HIGGS BOSON PRODUCTION WITH A TOP QUARK PAIR IN THE DIPHOTON CHANNEL, DOUBLE HIGGS PRODUCTION IN THE BB-DIPHOTON CHANNEL, AND INNER TRACKER UPGRADE WITH THE ATLAS DETECTOR AT THE LARGE HADRON COLLIDER

by

Alex Zeng Wang

A dissertation submitted in partial fulfillment of
the requirements for the degree of

Doctor of Philosophy

(Physics)

at the

UNIVERSITY OF WISCONSIN–MADISON

2023

Date of final oral examination: 05/08/2023

The dissertation is approved by the following members of the Final Oral Committee:

Kevin Black, Professor, Physics
Tulika Bose, Professor, Physics
Snezana Stanimirovic, Professor, Astronomy
Sau Lan Wu, Professor, Physics

To my family.

ACKNOWLEDGMENTS

First and foremost, I would like to give my thanks to my advisor Professor Sau Lan Wu, who supported me throughout these past seven years, including the difficult years of the pandemic. She is an exceptional physicist who helps her students in so many different ways, including but certainly not limited to: suggesting research directions, supporting them financially, treating them to dinner, giving career advice, or providing invaluable networking opportunities. The list of all the ways in which she has assisted me is too long to fit here, but it suffices to say that she treats her students as her own children and provides them with all the best. Without her, I would not have had the opportunity to participate in so many unique physics analysis and hardware activities. I'd also like to thank Professor Tulika Bose, Professor Kevin Black, and Professor Snezana Stanimirovic for taking the time to serve on my defense committee and and powering through two back-to-back defenses with me and my fellow student Jay Chan. I thank Wisconsin Professors Yang Bai, Stanislav Boldyrev, Daniel Chung, Lisa Everett, Aki Hashimoto, Jeff Schmidt for their interesting physics lectures which provided a solid foundation for my research. Finally, I'd like to express my thanks and best wishes to T. T. Wu, who is always a pleasure to talk to and provided very helpful feedback on my thesis.

When I first joined the Wisconsin group in 2017, I had no experience in how to do a physics analysis at ATLAS. Therefore I am sincerely indebted to Chen Zhou who patiently guided me through all the various steps and supervised me in my analysis work. I would also like to thank Hongtao Yang for teaching me about statistics and providing so many helpful code examples that I still use to this day. I thank Laser Kaplan for his foundational work in the $t\bar{t}H$ ($H \rightarrow \gamma\gamma$) analysis which introduced me to machine learning, a technique that is now so indispensable to all aspects of high energy physics. I thank Wen Guan and Shaojun Sun for their support in all matters technical, whether it is tuning hyperparameters or optimizing job submission scripts. I thank Rui Zhang for his leadership and guidance in the HH combination efforts. I thank Jay

Chan for the many interesting physics discussions and the pineapple cakes from Taiwan, as well as Alkaid Cheng for his work in all the HH-related analyses. And finally, I thank the other members of the Wisconsin group who I have had the pleasure of interacting with at various times, including Wasikul Islam, Xiangyang Ju, Lauren Osojnak, Tuan Pham, Yan Qian, Werner Wiedenmann, and Haimo Zobernig.

As a student in ATLAS, I have had the opportunity of interacting with a diverse set of people from many different backgrounds serving in many different roles. In the Higgs group, I thank Jennet Dickinson and Haichen Wang, who played a pivotal role in the $t\bar{t}H$ ($H \to \gamma\gamma$) analysis leading to the ATLAS $t\bar{t}H$ observation. I thank Marco Delmastro, who always provided leadership and a positive attitude despite the sometimes stressful nature of pushing out important ATLAS Higgs publications. For their contributions and guidance in various topics in the Higgs group, I thank Jahred Adelman, Nicolas Berger, Fabio Cerutti, Ana Rosario Cueto Gomez, Roberto Di Nardo, Saskia Falke, Stephen Gadatsch, Shuo Han, Yanping Huang, Rachel Hyneman, Marumi Kado, Karsten Koeneke, Bertrand Laforge, Chris Meyer, Davide Mungo, Ioannis Nomidis, Giacinto Piacquadio, Kunlin Ran, Xifeng Ruan, Kerstin Tackmann, Ruggero Turra, Renjie Wang, Zirui Wang and many others.

In the HH group, I thank Florian Beisiegel, Mohamed Belfkir, Tyler Burch, Feng Chen, Marc Escalier, Louis Fayard, Ivan Sayago Galvan, Linghua Guo, Jake Hofgard, Raphael Hulsken, Zihang Jia, Elena Mazzeo, Jannicke Pearkes, Laura Pereira Sanchez, Alan Taylor, and many others for all their work and contributions to the $HH \to b\bar{b}\gamma\gamma$ analysis and combinations. I thank Valentina Cairo for the career help and the many great physics discussions. I thank the contacts and conveners of the HH efforts for their excellent leadership, including Alessandra Betti, Liza Brost, David Delgove, Louis D'Eramo, Adele D'Onofrio, Luca Fiorini, Katharine Leney, Stefano Manzoni, Giovanni Marchiori, Elisabeth Petit, Eleonora Rossi, Jason Veatch, and Caterina Vernieri.

I thank Ben Nachman and Marco Bomben for their guidance in the silicon radiation damage group, and especially Ben for supervising me on my ATLAS qualification task and introducing me to interesting anomaly detection methods.

I thank the physicists at SLAC for hosting me so that I could benefit from their expertise on ITk hardware and physics analysis. I thank Charlie Young for always checking up on me and

helping me get set up at SLAC. I thank Caterina Vernieri for hosting the weekly physics analysis meetings where I learned about all the analysis activities. I thank Su Dong for his mentorship and his excitement towards everything related to data transmission. I thank Sanha Cheong, Zijun Xu, and Zhi Zheng who struggled together with me and in doing so made tremendous contributions to setting up the module testing procedures at SLAC. In addition, I thank the many people who worked on data transmission, loading, and general support and supervision, including Brendon Bullard, Philippe Grenier, Hannah Herde, Rachel Hyneman, Karin Kutlay, Nico Linton and his 3D printer, Akane Maeda, Matt McCulloch, Eric Miller, Norm Picker, Larry Ruckman, Matthias Wittgen, Andrew Young, and Fengrui Zuo. I thank also our ITk colleagues at other institutes, including Todd Claybaugh, Roman Mueller, Elisabetta Pianori, and Steven Welch who all provided much needed expertise in order to enable the success of the loading activities at SLAC. I thank Nicole Hartman, Rachel Smith, Murtaza Safdari, and all the other SLAC students for making me feel welcome and including me in all the fun events. I thank Jannicke Pearkes (again) for the great physics discussions and being a great office mate. As I have seen first-hand, even the most complicated hardware work is doable when working as part of a supportive environment.

For their help with various administrative concerns I thank the staff at Wisconsin, CERN, and SLAC, including Adrienne Higashi, Sharon Kahn, Aimee Lefkow, Renee Lefkow, Sylvie Padlewski, and many others. I especially thank Sylvie for her support while I was in Europe, and I also thank Shaojun and his wife for his help in France during the pandemic and for bringing me dumplings.

I would like to give my thanks to my brother Raymond and my other friends including Lena Low, Indraneel Mangat, Winston Wu, Jack Yang, Tommy Yang, Wallace Yu, Albert Zheng, who, despite not being personally involved in physics, still supported me throughout this long PhD. Finally, I thank my parents and grandparents who sacrificed so much to bring me to the United States and raised me to appreciate the value of education.

TABLE OF CONTENTS

Page

Page

LIST OF TABLES

Table Page

LIST OF FIGURES

Figure Page

Figure Page

Figure Page

Figure Page

ABSTRACT

Since the discovery of the Higgs boson in 2012, the diphoton ($\gamma\gamma$) decay channel of the Higgs boson has been one of the most potent channels due to the contrast between the smoothly falling background and sharply peaked signal in the diphoton invariant mass.

In 2018, with up to 80 fb^{-1} of data at $\sqrt{s} = 13$ TeV, ATLAS observed Higgs boson production in association with a pair of top quarks ($t\bar{t}H$) with a significance of 5.8 σ by combining measurements in the $\gamma\gamma$, $b\bar{b}$, ZZ, and multi-lepton Higgs decay channels. The $t\bar{t}H$ production cross-section was measured to be 670 $\pm$ 90 (stat) $^{+110}_{-100}$ (syst) fb. The diphoton channel was one of the main contributors to this result, alone providing a significance of 4.1 σ.

With 140 fb^{-1}, a search for non-resonant Higgs pair production in the $b\bar{b}\gamma\gamma$ final state was performed. No significant signal was observed and upper limits at 95% confidence level were set. The observed limit on the SM cross-section was 130 fb, or 4.2 times the predicted value. The observed Higgs trilinear coupling modifier was constrained to be between [-1.5, 6.7].

Both the $t\bar{t}H$ ($H \to \gamma\gamma$) and $HH \to b\bar{b}\gamma\gamma$ analyses will benefit tremendously from the increased statistics expected from the High-Luminosity LHC (HL-LHC). To ensure the continued efficiency of the detector in the harsh HL-LHC environment, ATLAS will install a new Inner Tracker (ITk) consisting of silicon pixel sensors in its innermost layer. At SLAC National Accelerator Laboratory, a variety of electrical tests are performed for the construction of a prototype integrated pixel system, in order to provide early feedback and validation of the ITk design.

Chapter 1

Introduction

The Standard Model (SM) of particle physics is the theory which describes elementary particles and their interactions. While it does not yet explain all aspects of nature such as gravity or the non-zero mass of the neutrinos, it has nevertheless been extraordinarily successful. The Standard Model includes 12 elementary fermions and their corresponding anti-particles, grouped into three generations of quarks (up/down, charm/strange, top/bottom) and three generations of leptons (electron/electron neutrino, muon/muon neutrino, tau/tau neutrino). In addition, 12 gauge bosons (the photon, W^+, W^-, and Z bosons, and 8 gluons) mediate the electroweak and strong interactions between the various particles of the Standard Model.

The latest addition to the Standard Model is the Higgs boson, a massive scalar elementary particle predicted in the 1960's as a consequence of the Brout-Englert-Higgs (BEH) mechanism [1–6], which provides a framework to generate the masses of all elementary particles except for the gluon and photon. It introduces a Higgs field, a complex scalar doublet with four degrees of freedom with a non-zero vacuum expectation value allowing for electroweak symmetry to be spontaneously broken. After symmetry breaking, three of these degrees of freedom become the longitudinal polarizations of the W and Z bosons, giving them mass. The remaining degree of freedom becomes the observed Higgs boson. In addition, the elementary fermions become massive due to Yukawa interactions with the Higgs field. Thus measuring the properties of the Higgs boson and its expected interactions with other particles would be a critical test of electroweak symmetry breaking.

In 2012, the Higgs boson was finally observed simultaneously by the ATLAS and CMS experiments [7, 8] using proton-proton (pp) collision data from the Large Hadron Collider (LHC), a 27 km long particle accelerator located near the city of Geneva, Switzerland. Its mass, a free

parameter in the Standard Model, was determined to be approximately $125\ \mathrm{GeV}$. Other expected properties such as the spin and parity were likewise verified [9, 10].

In Run 2 of the LHC, consisting of the data taking period from 2015 to 2018, the focus of LHC physics has shifted towards validating the interactions between the Higgs boson and other elementary particles. The expectation that the Higgs boson couples to fermions, vector bosons, and even itself leads to wide variety of signals that could potentially be detected at the LHC.

This thesis features three major topics, two of which involve analyzing Higgs boson production with Run 2 pp data collected by the ATLAS detector at the LHC. The first topic is the *$t\bar{t}H$ ($H \to \gamma\gamma$) analysis and $t\bar{t}H$ combination*. The $t\bar{t}H$ ($H \to \gamma\gamma$) analysis uses pp data collected from 2015 to 2017 to measure the production of Higgs bosons in association with two top quarks, in which the Higgs boson subsequently decays into two photons. In the *$t\bar{t}H$ combination*, the results from the $t\bar{t}H$ ($H \to \gamma\gamma$) analysis are then combined with other $t\bar{t}H$ analyses in the $H \to b\bar{b}$, $H \to \mathrm{multilepton}$, and $H \to ZZ^{(*)} \to 4l$ decay channels, in order to establish the ATLAS observation of $t\bar{t}H$ production announced in 2018. The second topic, the *$HH \to b\bar{b}\gamma\gamma$ analysis*, uses pp data collected from 2015 to 2018 to search for Higgs pair production, in which one Higgs decays into two photons and the other decays into two b-quarks. Aside from the main $HH \to b\bar{b}\gamma\gamma$ results, additional sub-results are also presented to give additional context. These include a statistical combination of the $HH \to b\bar{b}\gamma\gamma$ analysis with other double-Higgs and single-Higgs channels, as well as an extrapolation of the $b\bar{b}\gamma\gamma$ analysis to the conditions expected at the future High Luminosity LHC (HL-LHC). The third topic covers recent hardware efforts on a prototype Inner Tracker (ITk) system conducted at SLAC National Accelerator Laboratory. A major aspect of this work involves tests on the quality of the pixel modules and services providing data transmission, power, and status monitoring.

Chapter 2 provides a brief review of the phenomenology of Higgs boson physics at the LHC. Chapters 3 and 4 describe the components of the ATLAS detector and how various physics objects such as photons, electrons, muons, and jets are reconstructed and calibrated. Both the $t\bar{t}H$ ($H \to \gamma\gamma$) analysis and $b\bar{b}\gamma\gamma$ analysis feature a similar overall analysis strategy exploiting unique advantages of the $H \to \gamma\gamma$ decay at ATLAS. Therefore Chapters 5, 6, 7, and 8 feature a high-level overview of this common strategy for optimizing the event selection, modelling the signal and background, evaluating systematic uncertainties, and extracting statistical results. Chapter 9

covers the details of the $t\bar{t}H$ ($H \rightarrow \gamma\gamma$) analysis and $t\bar{t}H$ combination. Chapter 10 covers the $b\bar{b}\gamma\gamma$ analysis, the double-Higgs and single-Higgs combination, and the projection to the High Luminosity LHC (HL-LHC). Chapter 11 describes the hardware work on the ITk upgrade at SLAC. Finally, the main results of this thesis are summarized in Chapter 12.

Chapter 2

Phenomenology

The SM Lagrangian after symmetry breaking shows that the Higgs boson couples to elementary fermions, vector bosons, and even itself. The strength of the coupling to elementary fermions is proportional to the fermion mass, and the strength of the coupling to vector bosons is proportional to the square of the vector boson mass. Also present are the trilinear and quadrilinear self-couplings of the Higgs, which are related to the mass of the Higgs boson.

2.1 Single Higgs boson production and decays at the LHC

Figure 2.1 shows Feynman diagrams representing the main processes by which single Higgs bosons are produced and decay at the LHC. They feature a variety of interesting experimental signatures with cross-sections and branching ratios spanning multiple orders of magnitude [11]. Their values are summarized in Table 2.1, calculated for a center of mass energy of $\sqrt{s} = 13$ TeV and Higgs mass $m_H = 125.09$ GeV, the value obtained from the latest ATLAS and CMS combined measurement[1] [12].

Gluon fusion, ggF (Figure 2.1 (a)), is by far the largest and most common production mode at the LHC. As the Higgs does not directly couple to gluons, the interaction proceeds through a loop dominated by top quark contributions. Due to its large cross-section, it is often a persistent background in the $t\bar{t}H$ ($H \rightarrow \gamma\gamma$) and $b\bar{b}\gamma\gamma$ analyses despite efforts to reject it using kinematic selections.

[1] Since then, the precision of the Run 1 combination has been surpassed by individual ATLAS and CMS measurements, but 125.09 GeV remains the preferred value for many Run 2 ATLAS Higgs analyses.

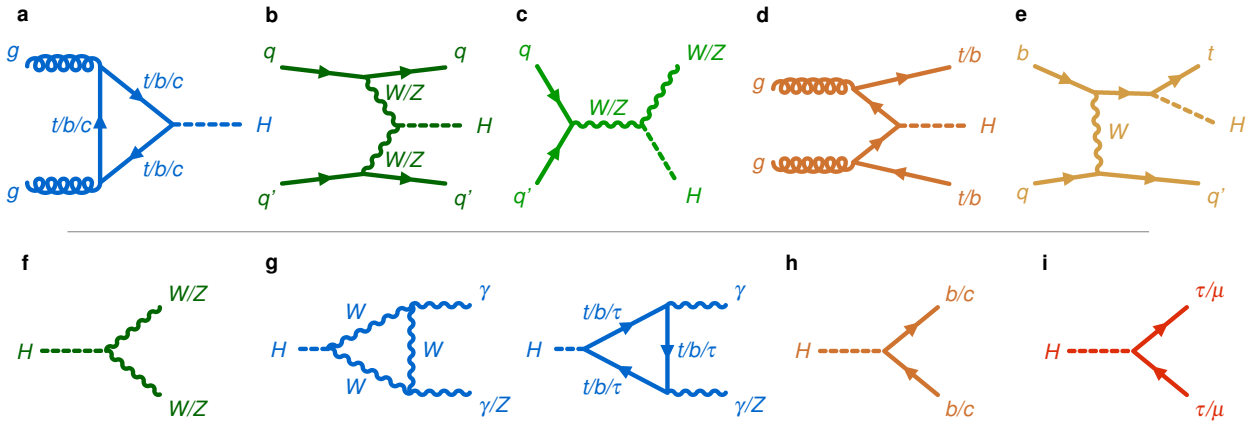

Figure 2.1: Representative leading order diagrams for single-Higgs production via (a) gluon fusion, (b) vector boson fusion, (c) associated production with a vector boson, (d) associated production with a pair of top or bottom quarks, and (e) associated production with a single top quark. The second row shows leading order diagrams for Higgs boson decays into (f) vector boson pairs, (g) photon pairs or $Z\gamma$, (h) fermion pairs, or (i) lepton pairs.

Single-Higgs production modes	σ_{SM} [pb] at 13 TeV	Order of calculation
ggF	48.5	N^{3}LO QCD + NLO EW
VBF	3.78	approximate-NNLO QCD + NLO EW
WH	1.37	NNLO QCD + NLO EW
$qq \to ZH$	0.76	NNLO QCD + NLO EW
$gg \to ZH$	0.12	NLO QCD
$t\bar{t}H$	0.51	NLO QCD + NLO EW
$b\bar{b}H$	0.49	NNLO QCD
$tHjb$	0.074	NLO QCD
tWH	0.015	NLO QCD

Table 2.1: Single Higgs boson production cross-sections and their corresponding orders of calculation from the CERN Yellow Report 4. Values are reported for $\sqrt{s} = 13$ TeV and $m_H = 125.09$ GeV. The s-channel production of $tHjb$ is neglected.

The second largest production mode is vector boson fusion, VBF (Figure 2.1 (b)), characterized by a distinctive signature of two back-to-back hard jets in the forward and backward regions of the detector.

The next largest production mode is associated production with a vector boson, VH, where $V = W^{\pm}, Z$ (Figure 2.1 (c)). It is commonly detected by the presence of jets, leptons, or neutrinos (missing energy) resulting from the decay of the W and Z bosons. ZH production includes both the dominant $qq \to ZH$ diagram and the less common $gg \to ZH$ production mode.

Associated production with a pair of top quarks, $t\bar{t}H$ (Figure 2.1 (d)), is quite rare, with a cross-section of only 0.5 pb. However its production provides a direct, tree-level probe of the top-Higgs Yukawa coupling. Similar to the case of WH and ZH, the decay of the top quark into a W and b quark presents a unique signature with multiple jets and possible leptons. $t\bar{t}H$ production is considered the signal in the $t\bar{t}H$ analysis, as well as a major background in the $b\bar{b}\gamma\gamma$ analysis. Also related is the associated production with a pair of bottom quarks, $b\bar{b}H$ (Figure 2.1 (d)).

Associated production with a single top quark, tH, proceeds mainly through the t-channel, $tHjb$ (Figure 2.1 (e)), or in association with a W boson, tWH. Measurements of tH production are often correlated to those of $t\bar{t}H$ due to the similar final states. Unlike $t\bar{t}H$ however, tH is also sensitive to the sign of the top-Higgs Yukawa coupling; negative coupling values would lead to massive detectable enhancements in the tH cross-section [13].

Just as with the Higgs production modes, the Higgs decay channels also span multiple orders of magnitude, as shown in Table 2.2. The dominant Higgs decay channel is $H \to b\bar{b}$, (Figure 2.1 (h)) with a branching ratio of 58%. In contrast, the $H \to \gamma\gamma$ decay (Figure 2.1 (i, j)) possesses one of the smallest branching ratios at 0.227%. Despite this, it was one of the leading channels in the Higgs observation [7, 8] in both the ATLAS and CMS detectors due to its experimentally clean signature with two high energy photons. Due to the excellent resolution in the electromagnetic calorimeters, photons resulting from the $H \to \gamma\gamma$ decay manifest experimentally as a sharply peaked resonance in the diphoton invariant mass $m_{\gamma\gamma}$, in contrast to background diphoton events which constitute a smoothly falling *continuum* or *non-resonant* background. Both the ATLAS Run 2 $t\bar{t}H$ ($H \to \gamma\gamma$) and $b\bar{b}\gamma\gamma$ analyses use a similar strategy exploiting these features of the $H \to \gamma\gamma$ decay; in the case of $b\bar{b}\gamma\gamma$, the role of the $H \to b\bar{b}$ decay in the analysis strategy is very much secondary to that of the $H \to \gamma\gamma$ decay.

Higgs decay channel	Branching ratio [%]
$H \to b\bar{b}$	58.1
$H \to WW$	21.5
$H \to gg$	8.18
$H \to \tau\tau$	6.26
$H \to c\bar{c}$	2.88
$H \to ZZ$	2.64
$H \to \gamma\gamma$	0.227
$H \to Z\gamma$	0.154
$H \to \mu\mu$	0.022

Table 2.2: Theoretical Higgs boson decay branching ratios for $m_H = 125.09$ GeV.

2.2 Higgs pair production at the LHC

SM Higgs pair production (di-Higgs, double-Higgs, HH) is even more rare than single-Higgs production, with an inclusive cross-section smaller by about three orders of magnitude. Despite its small size, it is by far the best method to probe the trilinear Higgs self-coupling λ_{HHH}. At 13 TeV, di-Higgs production proceeds mainly through gluon-fusion (ggF) from a triangle and box diagram (Figure 2.2). In the SM, these diagrams interfere destructively, resulting to a small production cross-section of 31 fb (NNLO FTapprox [14, 15]) which would be difficult to observe with Run 2 LHC data. However, any changes to λ_{HHH}, such as those resulting from Beyond the Standard Model (BSM) models modifying the Higgs potential [16], could lead to large enhancements in the amplitude of the triangle diagram, resulting in much higher detectable cross-sections. After ggF HH, the second largest production mode is vector-boson fusion HH (Figure 2.3) with a much smaller SM cross-section of 1.7 fb (N3LO QCD [15]).

Figure 2.4 shows the production cross-sections of various SM HH production modes as a function of centre-of-mass energy and as a function of the self-coupling modifier $\kappa_\lambda = \lambda_{HHH}/\lambda_{HHH}^{SM}$ [17]. For comparison, the dependence of the single-Higgs cross-section as a function of κ_λ [11, 18, 19] is also shown.

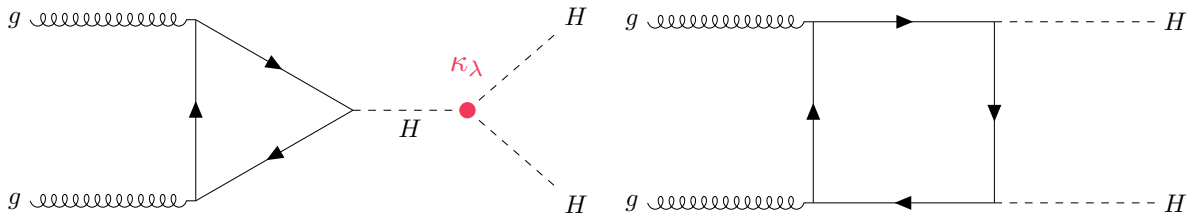

Figure 2.2: Leading order diagrams for Higgs pair production through gluon-fusion. In the SM, destructive interference between the (a) triangle and (b) box diagrams leads to a small cross-section of 31 fb at 13 TeV. The loops in the diagram are dominated by top quark contributions due to its large Yukawa coupling with the Higgs.

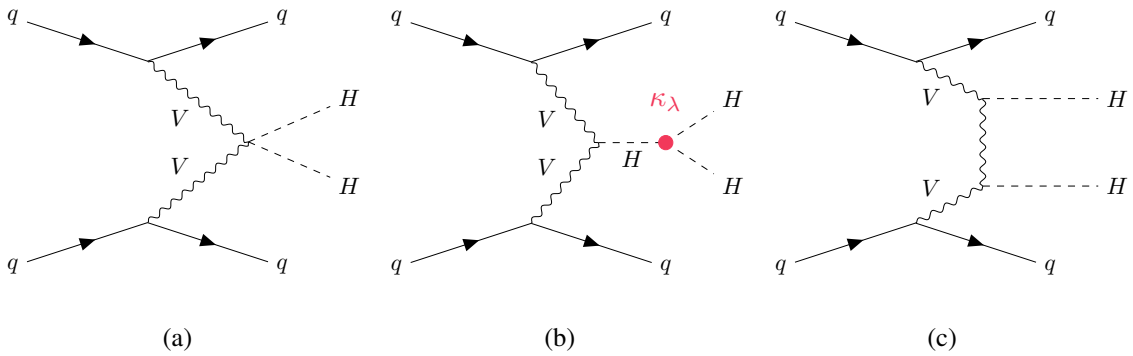

Figure 2.3: Leading order diagrams for Higgs pair production through vector boson fusion, showcasing (a) the $HHVV$ vertex, (b) the HHH vertex, and (c) the VVH vertex. In the SM, vector boson fusion has a cross-section of 1.7 fb at 13 TeV and therefore is subdominant to the main ggF process.

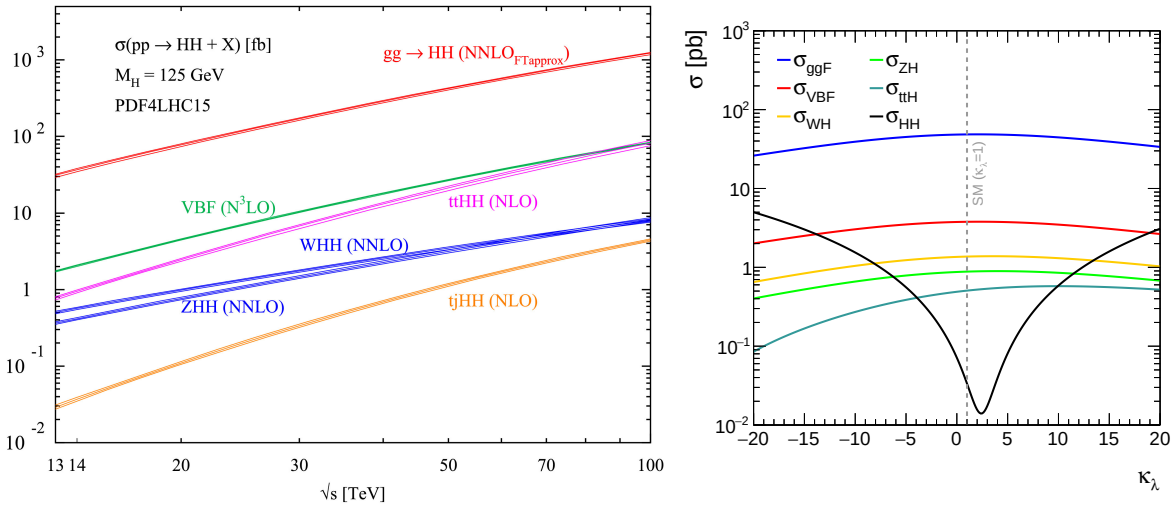

(a) (b)

Figure 2.4: (a) The production cross-sections of various SM HH production modes as a function of centre-of-mass energy. (b) The dependence of single-Higgs and double-Higgs cross-sections as a function of κ_λ at $\sqrt{s}$ = 13 TeV. The HH cross-section reaches a minimum at around κ_λ = 2.4, the point of maximum destructive interference between the box and triangle ggF diagrams.

2.3 Continuum background in $H \to \gamma\gamma$ analyses

In the $t\bar{t}H$ ($H \to \gamma\gamma$) and $b\bar{b}\gamma\gamma$ analyses, the continuum background is dominated by the non-resonant production of two prompt photons through diagrams such as Figure 2.5, accompanied by additional jets ($\gamma\gamma$ + jets) resulting from further selection criteria applied in these analyses. An additional prominent background component in these analyses originates from $t\bar{t}\gamma\gamma$ production, which despite to its smaller cross-section, is comparable to the $\gamma\gamma$ + jet component due to its similar final state as the signal. These processes involving two genuine photons typically make up 80% of the continuum background. A subdominant component of the background consists of photon-jet or jet-jet processes, in which jets are misidentified as photons.

A major advantage of the $H \to \gamma\gamma$ channel is that the continuum background can be assumed to be a smoothly falling, analytical, function of $m_{\gamma\gamma}$, whose shape and normalization parameters are constrained by the observed data. It is therefore not necessary to require detailed simulations of the strict composition of the background or calculations of its cross-section. The only consideration is whether the choice of the *type* of function used induces any significant bias on the fitted signal, which is determined following a procedure described in Section 5.

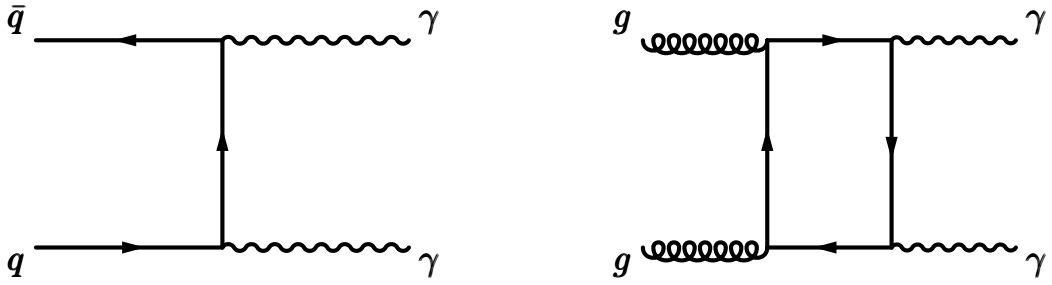

(a) (b)

Figure 2.5: Example diagrams of prompt diphoton production which constitute a majority of the diphoton continuum background in $H \to \gamma\gamma$ analyses. For the $t\bar{t}H$ ($H \to \gamma\gamma$) and $b\bar{b}\gamma\gamma$ analyses, these diagrams may involve additional jets to meet selection requirements.

Chapter 3

The ATLAS detector

The ATLAS detector [20] is a general-purpose detector with forward-backward symmetry and nearly full solid angle coverage around the interaction point. The interaction point defines the origin of a cylindrical coordinate system with z being the distance along the beam pipe, and r and ϕ the distance and azimuthal angle from the z-axis. The pseudorapidity is defined as $\eta = -\log\tan(\theta/2)$, where θ is the polar angle, while the angular distance between two points is defined as $\Delta R = \sqrt{(\Delta\eta)^2 + (\Delta\phi)^2}$.

The main components of the ATLAS detector can broadly be separated into the inner detector, the calorimeter, and the muon spectrometer (MS).

3.1 The inner detector

The inner detector is responsible for the reconstruction of particle tracks from the interaction point. It consists of a pixel detector, a silicon microstrip detector (SCT), and a transition radiation tracker (TRT), all immersed in a 2 T solenoidal magnetic field. The pixel and SCT detectors provide precision tracking over the region $|\eta| < 2.5$ and are arranged in concentric cylinders around the beam axis in the barrel region, and as perpendicular disks in the end-cap region. The pixel detector is closest to the interaction point, and as such, provides the most accurate readings with the most readout channels. TRT straws are arranged parallel to the beam axis in the barrel region or radially in wheels in the end-caps, and provide $R - \phi$ information for tracking up to $|\eta| = 2.0$. Despite its lower precision, the TRT complements the tracking capabilities of the pixel and SCT due to the large number of measurements and longer measured track length. The tracking properties of the inner detector make it critical for impact parameter measurements and vertexing

for heavy flavour and tau lepton tagging. It is also useful for tracking converted photons, defined as those which have produced e^+e^- pairs by interacting with the inner detector.

3.2 The calorimeter

The ATLAS calorimeter system measures the energy of particles and jets and consists of the electromagnetic (EM) and hadronic calorimeters covering the range $|\eta| < 4.9$. Both calorimeters use sampling technology consisting of alternating layers of an absorbing material to initiate particle showers and an active medium to measure the deposited energy.

As the name suggests, the EM calorimeter is designed to measure the energy of photons and electrons. High energy photons interact with the calorimeter material via e^+e^- pair production, which subsequently radiate photons by bremsstrahlung. The EM calorimeter is divided into cylindrical barrel ($|\eta| < 1.475$) and two end-cap ($1.375 < |\eta| < 2.5$, $2.5 < |\eta| < 3.2$) components. The detector medium consists of liquid argon due to its linear behaviour, stability of response over time, and radiation hardness, while an accordion geometry layout helps reduce dead zones from components such as cables. The EM calorimeter is segmented into three sections in the precision physics region ($|\eta| < 2.5$), while only two sections are present for $2.5 < |\eta| < 3.2$. A thin presampler layer in front of the EM calorimeter covers the region $|\eta| < 1.8$ in order to correct for energy lost upstream of the calorimeter. The ATLAS EM calorimeter design aims to achieve a relative energy resolution $\sigma_{\mathrm{E}}/E = 10\%/\sqrt{E} \oplus 0.7\%$ [20], where E is measured in GeV.

The hadronic calorimeters consist of the Tile, HEC, and FCAL calorimeters which measure the energy of hadronic interactions. The Tile calorimeter consists of steel absorber with scintillator tiles in the barrel region ($|\eta| < 1.0$) and two extended barrels ($0.8 < |\eta| < 1.7$) and is placed directly outside the envelope of EM calorimeter. The Hadronic End-cap Calorimeter (HEC) consists of two wheels per end-cap covering the area $1.5 < |\eta| < 3.2$ directly behind the end-cap EM calorimeters. Finally, the Forward Calorimeter (FCAL) covers the extreme forward region of $3.1 < |\eta| < 4.9$.

3.3 The muon spectrometer

The muon spectrometer consists of three large air-core superconducting toroids which deflect muon trajectories through three layers of chambers in each of the barrel and end-cap regions. Monitored Drift Tube chambers (MDTs) and Cathode-Strip Chambers (CSCs) provide precision muon tracking for $|\eta| < 2.7$. These are complemented by the muon triggering system consisting of Resistive Plate Chambers (RPCs) in the barrel region ($|\eta| < 1.05$) and Thin Gap Chambers (TGCs) in the end-caps ($1.05 < |\eta| < 2.4$), which provide bunch-crossing identification, well-defined p_{T} thresholds, and measurements of the muon coordinates in the direction orthogonal to that determined by the MDT and CSCs.

3.4 The trigger system

The initial event rate of 1.7 billion collisions per second is reduced to a much more manageable 100 kHz by a hardware-based L1 trigger and further to 1 kHz by the software-based high level trigger (HLT) [21]. Both the $t\bar{t}H$ ($H \rightarrow \gamma\gamma$) and $b\bar{b}\gamma\gamma$ analyses presented in this thesis use the same diphoton trigger targeting the presence of two high momentum photon-like objects. The hardware L1 diphoton trigger requires two distinct transverse energy deposits of at least 15 GeV in a 2x2 cluster in the electromagnetic calorimeter [22]. The L1 trigger gives region of interest (ROI) information such as the η and ϕ coordinates of events passing this criteria to the HLT. The HLT requires transverse momentum of at least 35 GeV and 25 GeV for the two highest p_T photons, as well as *Loose* criteria based on shower shape variables in the calorimeter. For data taken in 2017 and 2018, to account for the increase in pileup, the L1 energy criterium was raised to 20 GeV and the HLT required the *Medium* shower shape criteria.

Chapter 4

Object reconstruction

Both the $t\bar{t}H$ ($H \rightarrow \gamma\gamma$) and $b\bar{b}\gamma\gamma$ analyses use a similar set of physics object definitions summarized below. One major exception involves a change in the default jet reconstruction and b-tagging algorithms between the publication of the $t\bar{t}H$ ($H \rightarrow \gamma\gamma$) and $b\bar{b}\gamma\gamma$ analyses. Furthermore, the $b\bar{b}\gamma\gamma$ analysis uses an additional calibration procedure to further improve the energy of b-jets and better identify the $H \rightarrow b\bar{b}$ decay.

4.1 Photons

Photon candidates are reconstructed from topological clusters in the EM calorimeter and are required to have $|\eta| < 2.37$ and $1.37 < |\eta| < 1.52$ in order to be in the acceptance range of the inner tracker and to avoid the crack region between the barrel and endcaps. In order to reject non-prompt photons produced from hadronic jets containing neutral pions, photons must further pass the *Tight* identification criteria, based on the lateral and longitudinal energy profiles of the calorimeter showers, as well as the *Fixed Cut Loose* calorimeter and track-based isolation requirements [23]:

- topoetcone20 $< 0.065 E_{\mathrm{T}}^{\gamma}$
- ptcone20 $< 0.05 E_{\mathrm{T}}^{\gamma}$

where topoetcone20 is the sum of energies in topological clusters and ptcone20 is the scalar sum of track p_{T} within a cone of $\Delta R = 0.20$ around a photon.

Photons may be labeled as converted or unconverted, based on whether they have produced electron-positron pairs before reaching the electromagnetic calorimeter. The photon energy is calibrated based on a multivariate regression algorithm and corrected using scale factors derived from

$Z \to e^+e^-$ events. The direction of the photons is reconstructed by exploiting the longitudinal segmentation of the calorimeter and constraints from the beam spot position, as well as (for converted photons) position and track information associated with conversion vertex.

4.2 Diphoton vertex

Collision vertices are defined as those with at least two tracks with $p_{\mathrm{T}} > 0.5$ GeV. In many analyses the primary vertex is chosen to be the *hardest vertex*, the vertex with the highest $\sum p_{\mathrm{T}}^2$ of tracks associated with said vertex. However for $H \to \gamma\gamma$ analyses this is not necessarily the best choice as photons generally do not leave tracks in the inner tracker, although their trajectories can still be inferred from the segmentation of the calorimeter. For photons with conversion track hits in either the Pixel or SCT that are consistent with a collision vertex, that vertex can be selected directly as the diphoton vertex.

Otherwise, a neural network [24] is used to identify the diphoton vertex using the following variables as input:

- $(z_{\mathrm{common}} - z_{\mathrm{vertex}})/\sigma_z$, where z_{vertex} is the position of the primary vertex in the z-direction, z_{common} is the weighted mean of z-positions of extrapolated photon trajectories calculated from calorimeter pointing with a constraint from the beam spot position, and σ_z is the associated extrapolation error
- $\sum p_{\mathrm{T}}$, the scalar sum of transverse momenta of tracks associated with the vertex
- $\sum p_{\mathrm{T}}^2$, the squared scalar sum of transverse momenta of tracks associated with the vertex
- $\Delta\phi(\gamma\gamma, \mathrm{vertex})$ the azimuthal angle between the diphoton system and the system defined by the vector sum of tracks associated with the vertex

This NN is able to select a vertex within 0.3 mm of the true vertex for $> 80\%$ of inclusive signal events, increasing to up to $> 98\%$ for signals with many tracks such as $t\bar{t}H$. The performance is noticeably better than the hardest vertex approach for events with low numbers of tracks. Following the selection of the diphoton vertex, all quantities are then recalculated relative to that selected vertex.

4.3 Leptons

Electrons are reconstructed from energy clusters in the EM calorimeter matched to tracks in the inner detector. Muons are reconstructed from tracks in the muon spectrometer with possibly additional matched contributions from tracks in the inner detector. Electrons are required to have $p_{\mathrm{T}} > 10$ GeV and $|\eta| < 2.47$, excluding $1.37 < |\eta| < 1.52$, while muons are required to have $p_{\mathrm{T}} > 10$ GeV and $|\eta| < 2.7$ [23, 25]. Electrons (muons) must have an impact parameter significance of $|d_0/\sigma(d_0)| < 5$ ($|d_0/\sigma(d_0)| < 3$) and $|z_0 \sin\theta)| < 0.5$ mm relative to the diphoton vertex. Both electrons and muons are further required to satisfy identification criteria and both calorimeter and track based isolation.

For the $t\bar{t}H$ and $b\bar{b}\gamma\gamma$ analyses, tau leptons are not directly reconstructed, and any selections on leptons refer only to electrons and muons.

4.4 Jets

For the $t\bar{t}H$ ($H \to \gamma\gamma$) analysis, jets are reconstructed from 3-dimensional topological clusters in the electromagnetic and hadronic calorimeters (EMtopo) [26] using the anti-k_t algorithm [27,28] with radius parameter $R = 0.4$. For the $b\bar{b}\gamma\gamma$ analysis, the EMtopo algorithm was updated to the particle-flow (PFlow) algorithm [29], which combines information from both the tracker and calorimeter in order to achieve improved resolution, reconstruction efficiency, and pileup resistance. In both cases, jets are required to have $p_{\mathrm{T}}>$ 25 GeVand $|y| < 4.4$. Furthermore, a jet vertex tagger [30] is applied to jets with $p_{\mathrm{T}} < 60$ GeV and $|\eta| < 2.4$ in order to suppress contributions from pileup by ensuring the jet indeed originates from the correct primary vertex.

4.4.1 b-jets

For the $t\bar{t}H$ ($H \to \gamma\gamma$) analysis, jets with $|\eta| < 2.5$ (central jets) resulting from the hadronization of b-quarks (b-jets) are identified using the MV2c10 [31] algorithm, using both object-level variables such as jet p_{T} and event-level variables such as the impact parameter with respect to the primary vertex and the number of associated tracks. For the $b\bar{b}\gamma\gamma$ analysis, the MV2c10 algorithm is replaced with the DL1r tagger which uses a different MVA algorithm and additional input variables to achieve superior performance [32]. For both cases, four working points are provided, with

associated b-jet efficiencies of 60%, 70%, 77%, and 85%, and a corresponding light jet rejection rate ranging from 1300 to 30.

For the $b\bar{b}\gamma\gamma$ analysis, the kinematics of the b-jets are particularly important as they are used to reconstruct the $H \to b\bar{b}$ decay, and therefore an additional b-jet energy calibration is applied. A μ-in-jet correction associates muons originating from B or D hadrons with the jets they are emitted from, which would normally be lost from the calculation of the jet energy. A further p_{T}-reco correction accounts for the presence of neutrinos and out-of-cone radiation by applying a global p_{T}-dependent scale factor derived from $t\bar{t}$ samples to the jet 4-vector. In $HH \to b\bar{b}\gamma\gamma$ events, the combination of both corrections improves the width of the $m_{b\bar{b}}$ distribution by 20%, while shifting its peak closer to m_H.

4.5 Overlap removal

An overlap removal procedure is applied to avoid double-counting reconstructed lepton or photon candidates as jets:

- Remove electrons, muons, or jets within $\Delta R = 0.4$ of any photon
- Remove jets within $\Delta R = 0.2$ of any electron
- Remove electrons or muons within $\Delta R = 0.4$ of any jet

4.6 Missing transverse energy

The missing transverse energy $E_{\mathrm{T}}^{\mathrm{miss}}$ is calculated from the negative vector sum of all reconstructed objects in an event. An additional track based soft-term (TST) is added to account for non-reconstructed objects with low-p_{T} but well-reconstructed tracks associated with the diphoton vertex.

$$E_{x(y)}^{\mathrm{miss}} = -\sum_{i=\gamma,e,\mu,\mathrm{jet},\mathrm{soft\ track}} (p_i)_{x(y)} \tag{4.1}$$

The $E_{\mathrm{T}}^{\mathrm{miss}}$ and direction ϕ^{miss} are consequently defined as

$$\begin{aligned} E_{\mathrm{T}}^{\mathrm{miss}} &= \sqrt{(E_x^{\mathrm{miss}})^2 + (E_y^{\mathrm{miss}})^2} \\ \phi^{\mathrm{miss}} &= \arctan(E_y^{\mathrm{miss}}/E_x^{\mathrm{miss}}) \end{aligned} \tag{4.2}$$

The variables $E_{\mathrm{T}}^{\mathrm{miss}}$ and ϕ^{miss} are commonly used as a proxy for neutrinos or other BSM particles that do not interact directly with detector elements.

Chapter 5

Preselection and event categorization

The $t\bar{t}H$ ($H \to \gamma\gamma$) and $b\bar{b}\gamma\gamma$ analyses both use a similar strategy exploiting the diphoton mass as a discriminant variable; their similarities in analysis strategy are therefore summarized below.

All events are selected by the diphoton trigger (Section 3.4) requiring two tight, isolated (Section 4.1) photons with $p_{\mathrm{T}} > 35(25)$ GeV. In addition, the diphoton invariant mass $m_{\gamma\gamma}$ must satisfy $105 < m_{\gamma\gamma} < 160$ GeV, and in order to avoid the turn-on threshold of the diphoton trigger, the ratio $p_{\mathrm{T}}/m_{\gamma\gamma}$ of the leading (subleading) photon is required to be greater than 35% (25%). The window $120 < m_{\gamma\gamma} < 130$ GeV is termed the *signal region* as it roughly covers 95% of the expected Higgs signal, while the remainder $105 < m_{\gamma\gamma} < 130$ and $130 < m_{\gamma\gamma} < 160$ is defined as the *sideband region*.

A set of simple additional offline selections depending on the expected signal topology are then applied to further increase the signal to background ratio. For example, the $t\bar{t}H(H \to \gamma\gamma)$ observation analysis requires additional jets and leptons consistent with the decay of a top quark, while the $b\bar{b}\gamma\gamma$ analysis requires two additional b-jets. After this stage, a multi-variate analysis (MVA) technique is used to further separate signal and background. In this way, the complicated multi-variate phase space is reduced to a single variable ranking the likelihood of an event being signal or background. This MVA score is then used to define different categories. This is done by performing an exhaustive scan over all possible boundaries, with the objective to maximize the combined significance in the selected categories, while discarding events with an extremely low signal likelihood.

To avoid overtraining the model and artificially inflating the expected performance of the categorization strategy, the entire process is performed on a selection of events taken from either a data

control region or from a statistically independent set of simulated events. Only at the last moment when the analysis selection is frozen is the selection finally applied to real, unblinded, data.

Chapter 6

Signal and background modelling

The $m_{\gamma\gamma}$ spectrum of the signals and backgrounds are modelled separately by analytical functions in each of the analysis categories. Broadly, two types of processes are considered. Processes involving the decay of a Higgs boson to two photons form a sharply peaked resonance centered at 125 GeV. The remaining continuum, or non-resonant, background can be modelled as an analytical smoothly falling function of $m_{\gamma\gamma}$.

6.1 Modelling of Higgs boson processes

In each category, the $m_{\gamma\gamma}$ shape of the di-Higgs and single-Higgs processes is defined by a double-sided crystal ball (DSCB) [24, 33] distribution, which is a Gaussian core with power law tails:

$$f(t) = \begin{cases} e^{-\frac{1}{2}t^2}, & -\alpha_L \leq t \leq \alpha_H \\ e^{-\frac{1}{2}\alpha_L^2}\left[\frac{\alpha_L}{n_L}\left(\frac{n_L}{\alpha_L} - \alpha_L - t\right)\right]^{-n_L}, & t < -\alpha_L \\ e^{-\frac{1}{2}\alpha_H^2}\left[\frac{\alpha_H}{n_H}\left(\frac{n_H}{\alpha_H} - \alpha_H + t\right)\right]^{-n_H}, & t > \alpha_H \end{cases} \tag{6.1}$$

with $t = (m_{\gamma\gamma} - \mu_{CB})/\sigma_{CB}$ and parameters $\mu_{CB}, \sigma_{CB}, \alpha_L, n_L, \alpha_H, n_H$. In particular, μ_{CB} controls the position of the peak and σ_{CB} the width of the central Gaussian. The parameters are obtained from a fit to simulated Monte Carlo events (MC) and generally fixed in the fit, with the exception of μ_{CB} and σ_{CB} which may be modified by systematic uncertainties.

6.2 Modelling of the continuum background

The continuum $\gamma\gamma$ background is modelled by an analytical function whose shape and normalization are obtained from a fit to the data. This approach is therefore almost completely data-driven,

with the exception of the specific choice of function. A background function with too many degrees of freedom may absorb a portion of a real signal, while a background function with too few degrees of function may fit poorly and cause the appearance of a fake signal where there is none.

In every category of an analysis, the choice of background function and associated bias are estimated with the so-called *spurious signal* test. First, a high-statistics background-only template is created as a proxy for the real continuum background. The construction of the background-only template depends on the individual analyses and are detailed in the following sections. In all cases, the templates are validated against sideband data to ensure that they provide an adequate description of the continuum background.

A potential background function is tested by performing a signal plus background fit to the background-only template, with the signal extracted from such a fit denoted as N_{sp}. To account conservatively for possible variations in the signal position, multiple such fits are performed for signal peak positions in the range of $[121, 129]$ GeV, and the *spurious signal* is defined as the maximum magnitude of N_{sp} over that range. The function passes the test if the associated spurious signal is small, with respect to either the expected number of signal events or the expected statistical uncertainty on the signal:

- $\mathrm{Max}|(N_{sp}/N_{s,\mathrm{exp}})| < 10\%$, where $N_{s,\mathrm{exp}}$ is the expected number of signal events in the category.
- $\mathrm{Max}|(N_{sp}/\sigma_{\mathrm{bkg}})| < 20\%$, where σ_{bkg} is the statistical uncertainty on the fitted number of signal events when fitting the signal plus background model to the template, with the template errors estimated from the data sideband.

For categories with extremely low statistics, the spurious signal criteria are further relaxed to accommodate 2 σ local statistical fluctuations in the background template by defining a new variable ζ_{sp}:

$$\zeta_{sp} = \begin{cases} N_{sp} + 2\Delta_{MC}, & N_{sp} + 2\Delta_{MC} < 0 \\ N_{sp} - 2\Delta_{MC}, & N_{sp} - 2\Delta_{MC} > 0 \\ 0, & \text{otherwise} \end{cases} \tag{6.2}$$

where Δ_{MC} is a local statistical fluctuation of the background template. ζ_{sp} should then pass the criteria as N_{sp} before.

If multiple functions pass the spurious signal test, generally the one with the smallest number of degrees of freedom is chosen, though the exact criteria depends on the analysis. Each function is finally tested by checking the fit quality on the data sideband. The associated bias enters the statistical model as an additional signal whose normalization is constrained by a Gaussian centered at 0 with magnitude equal to the value of the spurious signal.

Chapter 7

Systematic uncertainties

In the $t\bar{t}H$ ($H \rightarrow \gamma\gamma$) and $b\bar{b}\gamma\gamma$ analyses, systematic uncertainties affect the normalizations and $m_{\gamma\gamma}$ distributions of the single-Higgs and di-Higgs samples. While the exact magnitudes of the uncertainty vary between the two analyses, a list of the common sources of experimental and theoretical systematics is summarized below. It is assumed that uncertainties on the $m_{\gamma\gamma}$ shape impact only the σ_{CB} and μ_{CB} parameters of the DSCB function. By design, the only systematic uncertainty associated with the modelling of the non-resonant background is the spurious signal, as described in section 6.2.

7.1 Experimental systematic uncertainties

Sources of experimental systematic uncertainties include

- The luminosity
- The value of the Higgs boson mass
- The diphoton trigger efficiency
- The photon identification and isolation efficiency.
- The photon energy scale and resolution
- The jet energy scale and resolution
- The jet vertex tagger efficiency
- The efficiency of the b-tagging algorithm

- The lepton reconstruction efficiency
- The calculation of the $E_{\mathrm{T}}^{\mathrm{miss}}$
- The modelling of pileup in the simulation

The photon energy scale and resolution uncertainties affect both the normalization and shape of the Higgs processes, while the uncertainty on the Higgs boson mass affects only the shape of the Higgs processes. All other uncertainties affect only the normalization.

The nominal integrated luminosity is obtained from measurements taken by the LUCID-2 detector [34]. For the 80 fb^{-1} and 140 fb^{-1} datasets used in the $t\bar{t}H$ ($H \to \gamma\gamma$) and $b\bar{b}\gamma\gamma$ analyses, the uncertainty on its value is on the order of 2%.

An uncertainty of 0.19% is applied to the value of the Higgs boson mass, corresponding to the error from the Run 1 combined mass measurement by ATLAS and CMS [12].

The uncertainty on the efficiency of the diphoton trigger is evaluated using radiative Z boson decays and with a bootstrap technique involving events collected from prescaled lower-threshold triggers [22]. It is on the order of 1%. Uncertainties in photon identification and isolation are obtained from control samples of prompt photons from γ + jet production and radiative Z decays, and $Z \to e^+e^-$ events [23]. The photon energy scale and resolution uncertainties are determined from control samples of electrons from Z boson and J/ψ decays and photons from radiative Z boson decays [23]. The impacts on the peak position and width of the DSCB signal is on the order of 0.5% (photon energy scale) or 10% (photon energy resolution).

Uncertainties in the jet energy scale and resolution are obtained from control samples where jets recoil against well calibrated particles such as photons, Z bosons, or other jets [35]. Other uncertainties relating to electrons, muons, flavour tagging, the $E_{\mathrm{T}}^{\mathrm{miss}}$ calculation, and pileup modelling are also evaluated and generally found to be negligible.

7.2 Theoretical systematic uncertainties

Sources of theoretical systematic uncertainties include the Higgs boson branching ratios, the presence of higher order QCD terms, the value of the QCD coupling constant α_s, the parton distribution function, the choice of parton showering algorithm, and the modeling of certain single Higgs processes in association with heavy flavour jets.

The uncertainties on the $H \to \gamma\gamma$ and $H \to b\bar{b}$ branching ratios are obtained from Ref. [11].

Uncertainties due to missing higher-order terms in the perturbative QCD cross-section calculation, the PDF set, and the value of α_s are estimated by considering alternative choices of factorization and renormalization scales, PDF sets, and α_s values. These uncertainties are factorized into their effects on the total inclusive cross-sections, and on the migration of events between categories caused by changes in the distribution of kinematic variables. In measurements of the signal strength $\mu = \sigma/\sigma_{SM}$ both effects are included. However, in direct measurements of the signal cross-section, the former uncertainties are then removed.

The uncertainties from the modelling of the parton shower, underlying event, and hadronization is evaluated by comparing the yields obtained from the nominal generated samples to alternative samples using the same generator but a different showering algorithm.

An additional systematic uncertainty is associated with the production of ggH, VBF, and VH in association with heavy flavour jets. A conservative 100% uncertainty on the yield on these processes is implemented based on measurements using $H \to ZZ^{(*)} \to 4l$ [36], $t\bar{t}\ b\bar{b}$ [37], and Vb [38] [39] events.

Chapter 8

Statistical framework

8.1 Likelihood function

The statistical results are obtained from an extended maximum likelihood fit of the $m_{\gamma\gamma}$ distribution in the range $105 < m_{\gamma\gamma} < 160$ GeV, performed simultaneously over all relevant categories. The likelihood is defined as:

$$\mathcal{L} = \prod_{c} \left(\text{Pois}(n_c | N_c(\theta)) \cdot \prod_{i=1}^{n_c} f_c(m^i_{\gamma\gamma}, \theta) \cdot G(\theta) \right) \tag{8.1}$$

where for each event i in a category c, n_c is the observed number of events, N_c is the expected number of events, f_c is the value of the probability density function, θ are nuisance parameters representing systematic uncertainties, and $G(\theta)$ are Gaussian constraints on the nuisance parameters. In the $t\bar{t}H$ ($H \to \gamma\gamma$) and $b\bar{b}\gamma\gamma$ analyses, the only unconstrained nuisance parameters are the shape and normalization parameters of the continuum background functions.

The expected number of events N_c, defined in equation 8.2, is the sum of the expected yields from all considered processes: di-Higgs (in the case of the $b\bar{b}\gamma\gamma$ analysis), single-Higgs, the spurious signal uncertainty, and the non-resonant background:

$$N_c(\theta) = \mu \cdot N_{\text{HH,c}}(\theta_{\text{yield}}) + N_{\text{H,c}}(\theta_{\text{yield}}) + N_{\text{sp,c}} \cdot \theta_{\text{sp,c}} + N_{\text{non-res,c}} \tag{8.2}$$

where $\mu = \sigma/\sigma_{SM}$ is the signal strength, θ_{yield} and $\theta_{\text{sp,c}}$ represent yield systematics, as detailed in Section 7.

The probability density function f_c representing the shape information shown in equation 8.3 is the sum of the DSCB functions modelling di-Higgs signals, single-Higgs, and the spurious signal (Section 6.1), and the analytical function modelling the non-resonant background chosen by the

spurious signal test (Section 6.2):

$$f_c(m_{\gamma\gamma},\theta) = [\mu \cdot N_{\mathrm{HH,c}}(\theta_{\mathrm{yield}}) \cdot f_{\mathrm{HH,c}}(m_{\gamma\gamma},\theta_{\mathrm{shape}}) + N_{\mathrm{H,c}}(\theta_{\mathrm{yield}}) \cdot f_{\mathrm{H,c}}(m_{\gamma\gamma},\theta_{\mathrm{shape}}) + N_{\mathrm{sp,c}} \cdot \theta_{\mathrm{sp,c}} \cdot f_{\mathrm{HH,c}}(m_{\gamma\gamma},\theta_{\mathrm{shape}}) + N_{\mathrm{non-res,c}} \cdot f_{\mathrm{non-res,c}}(m_{\gamma\gamma},\theta_{\mathrm{shape}})]/N_c(\theta_{\mathrm{yield}}) \quad (8.3)$$

where θ_{shape} represents shape systematics.

Variations in the nuisance parameters $\theta_{\mathrm{yield}}, \theta_{\mathrm{sp,c}}, \theta_{\mathrm{shape}}$ are propagated to the number of events N or the PDF shape f through response functions, implemented in three ways:

- Gaussian: $X(\theta) = X_0(1+\sigma\theta)$
- Log-normal: $X(\theta) = X_0 \exp(\log(1+\sigma)\theta)$
- Asymmetric

where σ is the magnitude of the systematic uncertainty, and X is the impacted quantity: either the yield (for yield systematics), or the σ_{CB} or μ_{CB} parameters of the DSCB (for shape systematics). Symmetric uncertainties, where the magnitudes of the upper and lower variations are equal, use either the Gaussian or log-normal response functions. Typically, Gaussian response functions are used for migration uncertainties, the spurious signal, and the uncertainty on the $H \to \gamma\gamma$ peak position, while the log-normal is used for everything else. An additional application of the log-normal distribution is for uncertainties which should never give a negative result, such as the impact of the luminosity uncertainty on the total event yield. In practice the difference between the two is often negligible. The asymmetric response function is used in cases where the upper and lower variations are unequal, and is defined as an interpolation between two log-normal functions.

In a combination of different channels, such the $t\bar{t}H$ combination, the combined likelihood function is simply obtained by multiplying the individual likelihood functions together. Systematic uncertainties in the different channels may be correlated (de-correlated) by equating (not equating) the nuisance parameters corresponding to said uncertainties in each channel.

The value of μ can be obtained in a fit as the value which maximizes the likelihood given in Equation 8.1 on the data. In the case where a positive μ is found, the *significance* of this can be calculated; intuitively it is the chance that such an excess could not be explained purely due statistical fluctuations alone. In the case where there is no significant excess, one can infer that

there is some *upper limit* to the possible value of μ - otherwise an excess in the data would have been observed. Fundamentally, the calculation of both quantities is based on the profile likelihood

$$\lambda(\mu) = -2\log\frac{L(\mu,\hat{\hat{\theta}})}{L(\hat{\mu},\hat{\theta})} \tag{8.4}$$

where $\hat{\hat{\theta}}(\mu)$ is the value of the nuisance parameters that maximize the likelihood for the value of μ, and $\hat{\mu}$ and $\hat{\theta}$ are the unconditional maximum-likelihood values.

In both analyses, it is assumed that the presence of a signal can only enhance the total number of events, i.e. $\mu \geq 0$.

8.2 Discovery significance

The level of disagreement between the data and a hypothesized value of μ is quantified by the test statistic:

$$\tilde{t}_\mu = \begin{cases} -2\log\frac{L(\mu,\hat{\hat{\theta}}(\mu))}{L(0,\hat{\hat{\theta}}(0))} & \hat{\mu} < 0 \\ -2\log\frac{L(\mu,\hat{\hat{\theta}}(\mu))}{L(\hat{\mu},\hat{\theta})} & \hat{\mu} \geq 0 \end{cases} \tag{8.5}$$

Compared to Equation 8.4, the first case asserts that observing data with downward fluctuations $\hat{\mu} < 0$ should not be counted as more evidence against the signal hypothesis than observing data with $\hat{\mu} = 0$ (as it is assumed $\mu \geq 0$).

For the purpose of discovering a new signal, the null hypothesis to reject is $\mu = 0$ and therefore Equation 8.5 reduces to

$$q_0 \equiv \tilde{t}_0 = \begin{cases} 0 & \hat{\mu} < 0 \\ -2\log\frac{L(0,\hat{\hat{\theta}}(0))}{L(\hat{\mu},\hat{\theta})} & \hat{\mu} \geq 0 \end{cases} \tag{8.6}$$

It can be shown using the Wald approximation [40] that $f(q_0|0)$, the distribution of the test statistic q_0 under the $\mu = 0$ hypothesis, is a half chi-square, and that the discovery significance can be simply calculated as:

$$Z_0 = \sqrt{q_0} \tag{8.7}$$

In other words, the significance can be calculated easily from the log-likelihood difference of two fits performed to the data; one with μ fixed to 0, and one with μ freely floating.

In addition, in a simple counting experiment with the Poisson likelihood function

$$L(\mu) = \frac{(\mu s + b)^n}{n!} e^{-(\mu s + b)} \tag{8.8}$$

where n is the number of events, s is the number of signal events, and b is the number of background events, the significance reduces to the simple formula

$$Z_0 = \sqrt{q_0} = \begin{cases} \sqrt{2(n \log \frac{n}{b} + b - n)} & \hat{\mu} \geq 0 \\ 0 & \hat{\mu} < 0 \end{cases} \tag{8.9}$$

where $\hat{\mu} = \frac{n-b}{s}$

Finally the SM expected significance is

$$Z_0 = \sqrt{2((s+b)\log(1+s/b) - s)} \tag{8.10}$$

using $\mu = 1$ and $n = s + b$

Equation 8.10 is used as a proxy for the expected significance when optimizing the $t\bar{t}H$ ($H \to \gamma\gamma$) and $b\bar{b}\gamma\gamma$ analyses as it is easy to calculate, although it does not capture the full difference in $m_{\gamma\gamma}$ shape between the signals and backgrounds.

8.3 Upper limits

For setting limits, the test statistic is:

$$\tilde{q}_\mu = \begin{cases} -2 \log \frac{L(\mu, \hat{\hat{\theta}}(\mu))}{L(0, \hat{\theta}(0))} & \hat{\mu} < 0 \\ -2 \log \frac{L(\mu, \hat{\hat{\theta}}(\mu))}{L(\hat{\mu}, \hat{\theta}(\mu))} & 0 \leq \hat{\mu} \leq \mu \\ 0 & \hat{\mu} > \mu \end{cases} \tag{8.11}$$

where the third case asserts that observing data with upward fluctuations $\hat{\mu} > \mu$ should not be counted as evidence against the background only hypothesis.

From the Wald approximation [40], it can similarly be calculated that the CDF for obtaining an upper limit of μ, given a hypothesized value of μ' is

$$F(\tilde{q}_\mu|\mu') = \begin{cases} \Phi(\sqrt{\tilde{q}_\mu} - \frac{\mu-\mu'}{\sigma}) & 0 < \tilde{q}_\mu \leq \mu^2/\sigma^2 \\ \Phi(\frac{\tilde{q}_\mu - (\mu^2 - 2\mu\mu')/\sigma^2}{2\mu/\sigma}) & \tilde{q}_\mu > \mu^2/\sigma^2 \end{cases} \tag{8.12}$$

The classical 95% CL limit is the value of μ for which $p_\mu = 1 - F(\tilde{q}_\mu|\mu) = 5\%$. However, many ATLAS searches, including $HH \to b\bar{b}\gamma\gamma$, use instead the CLs definition [41] to set limits, which requires $p_\mu/(1-p_b) = 5\%$, where $p_b = 1 - F(\tilde{q}_\mu|0)$ is the p-value under the background-only hypothesis. The CLs convention results in more conservative (weaker) limits but avoids cases in which even the background-only hypothesis is excluded due to a low analysis sensitivity. In practice, the 95% limit is obtained using an iterative procedure in which μ is increased until $p_\mu/(1-p_b)$ exceeds 5%. In the following presented results, all limits use the CLs convention.

Chapter 9

$t\bar{t}H$ ($H \to \gamma\gamma$) analysis and $t\bar{t}H$ combination

9.1 Introduction

The coupling between the Higgs and the top quark is of special interest as the heaviest particle in the SM. While the Higgs-top Yukawa can be explored through potential loop contributions in ggF production and $H \to \gamma\gamma$ decays, $t\bar{t}H$ production provides a more direct, tree-level test of this coupling. In 2018, ATLAS and CMS independently observed $t\bar{t}H$ production [42,43] through a combination of the $H \to \gamma\gamma$, $H \to ZZ^{(*)}$, $H \to WW^{(*)}$, $H \to \tau^+\tau^-$, and $H \to b\bar{b}$ decay channels, an important first step in constraining the value of the Higgs-top Yukawa coupling. This section presents the $t\bar{t}H$ ($H \to \gamma\gamma$) analysis used in the ATLAS observation analysis and its subsequent combination with other channels. The $H \to \gamma\gamma$ channel was and still remains one of the most competitive for probing $t\bar{t}H$ production due to its high signal purity and relative ease of background modelling discussed in Section 2.

9.2 Data and simulation samples

The dataset used for the ATLAS $t\bar{t}H$ ($H \to \gamma\gamma$) analysis corresponds to 79.8 fb^{-1} of pp collision data at $\sqrt{s} = 13$ TeV collected from 2015 to 2017. Simulated Higgs boson events from ggF, VBF, VH, and $t\bar{t}H$ were generated using the POWHEG generator interfaced with PYTHIA8 for parton showering, hadronization, and underlying event simulation. Events from $b\bar{b}H$, $tHqb$, and tWH were generated with MADGRAPH5_aMC@NLO interfaced to PYTHIA8. The generated events were passed through GEANT4 [44] in order to simulate the response of the ATLAS detector. The cross-sections were set to the values shown in Table 2.1

As described in Section 6.2, the modelling of the non-resonant background is data-driven and therefore not directly represented by any MC samples. However, a $t\bar{t}\gamma\gamma$ sample was generated

using the MADGRAPH5_aMC@NLO generator and showered with PYTHIA8 in order to estimate the non-resonant background uncertainty in certain regions. In order to save processing time, the $t\bar{t}\gamma\gamma$ sample was passed through ATLFASTII [45], a fast parametric simulation of the ATLAS detector response.

9.3 Event Selection

Events are selected using the diphoton trigger requiring two photons with p_{T} greater than 35 GeV and 25 GeV. Photons are required to pass the isolation and identification quality requirements (Section 4.1) and the diphoton invariant mass must be satisfy $105 < m_{\gamma\gamma} < 160$ GeV.

The event selection strategy aims to maximize the signal-background separation power by exploiting the decay products of the top quarks and the Higgs. Over 90% of the time, the top quark decays into a b-quark and a W-boson, with latter subsequently decaying into two quarks (referred to as a hadronic top decay) or a lepton and neutrino (referred to as a leptonic top decay). Therefore, events are first broadly separated into a **Had** region, requiring 0 leptons and at least 3 jets, of which at least 1 must be b-tagged, and a **Lep** region, requiring at least 1 lepton and at least 1 b-tagged jet. The **Had** region targets events in which both top quarks decay hadronically, but also includes includes contributions from hadronic ttH decays with non-reconstructed τ leptons and leptonic ttH decays with unidentified leptons. The **Lep** region targets events in which at least one top quark decays leptonically.

In each region, a boosted decision tree (BDT) is trained to provide additional separation power between signal and background. In both regions, the BDT uses $t\bar{t}H$ MC as the training signal, while the training background uses data-driven control regions as a proxy for the non-resonant $\gamma\gamma$ background. In the **Had** region, this background consists of *NTI* events, defined as those in which at least one or more photons fail at least one of the isolation or identification requirements. The training background in the **Lep** region also uses NTI events, but with a further modification: the ≥ 1 b-jet requirement is relaxed to instead require at least one central jet, and the $m_{\gamma\gamma}$ window is expanded from [105, 160] GeV to [80, 250] GeV. Furthermore, the photon p_{T} requirement of $p_{\mathrm{T}}/m_{\gamma\gamma} > 0.35$ (0.25) is replaced with direct cut of $p_{\mathrm{T}} > 35$ (25) GeV. Despite slightly changing the event kinematics, the loosening of these photon and jet requirements increases the statistics available for training, and results in a net benefit to the effectiveness of the BDT model.

In the **Had** region, the BDT uses the following training variables to distinguish between signal and background:

- The $p_{\mathrm{T}}/m_{\gamma\gamma}, \eta, \phi, E/m_{\gamma\gamma}$ of the two photons
- The $p_{\mathrm{T}}, \eta, \phi, E$, and b-tag status of the 6 highest-p_T jets, where the b-tag status is 1 if a jet is b-tagged and 0 otherwise
- $E_{\mathrm{T}}^{\mathrm{miss}}$ and ϕ^{miss}, the magnitude and ϕ angle of the missing transverse momentum

The **Lep** region uses a similar set of variables, but with the removal of the b-tag status (due to the usage of non-b-tagged events in the training background), and the addition of the lepton 4-vector.

- The $p_{\mathrm{T}}/m_{\gamma\gamma}, \eta, \phi, E/m_{\gamma\gamma}$ of the two photons
- The $p_{\mathrm{T}}, \eta, \phi, E$, of the 4 highest-$p_T$ jets
- The $p_{\mathrm{T}}, \eta, \phi, E$, or the 2 highest-$p_T$ leptons
- $E_{\mathrm{T}}^{\mathrm{miss}}$ and ϕ^{miss}, the magnitude and ϕ angle of the missing transverse momentum

The scaling of the photon p_{T} and energy training variables is critical in order to prevent the BDT from simply selecting events based on the value of $m_{\gamma\gamma}$, thereby creating features in the $m_{\gamma\gamma}$ distribution of the non-resonant background which may be difficult to model. Figures 9.1 and 9.2 show the distributions of the main training variables for signal and background in the **Had** and **Lep** regions. Photons, leptons, and jets originating from the decay of a Higgs or top quark generally have higher p_{T} distributions than those originating from the non-resonant background, allowing for separation. In both regions, $E_{\mathrm{T}}^{\mathrm{miss}}$ variables are valuable for their modelling of neutrinos or misidentified leptons.

Following training, the BDT output in each region is shown in Figure 9.3, and demonstrates a clear separation between signal-like and background-like processes. In each of the **Had** and

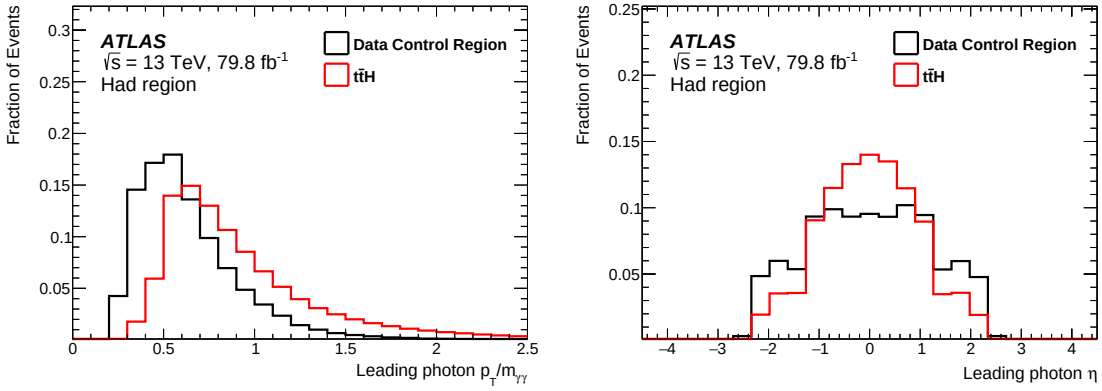

(a)

(b)

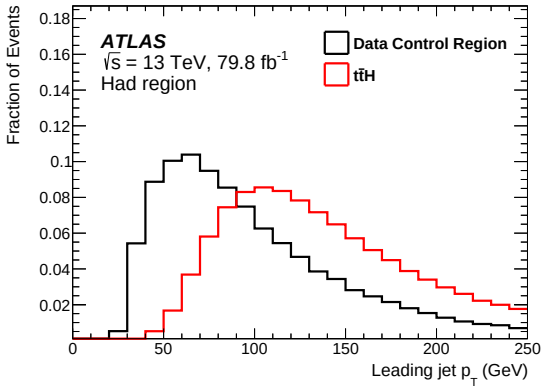

(c)

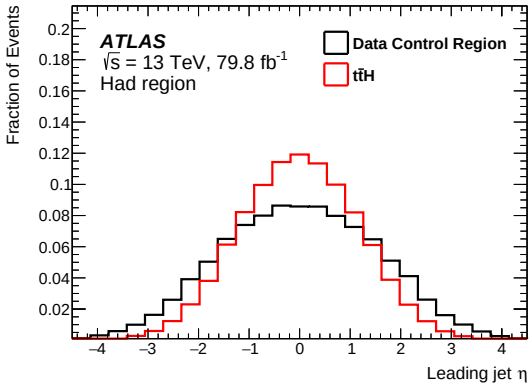

(d)

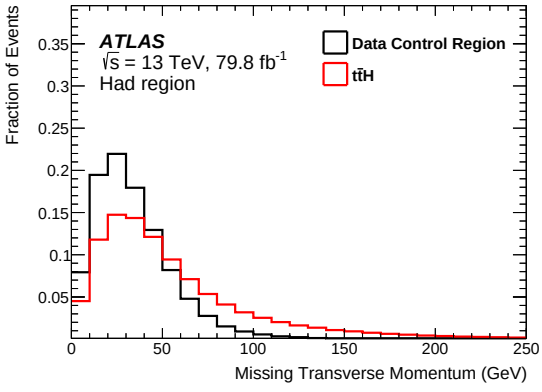

(e)

Figure 9.1: The distributions of the main BDT training variables in the **Had** region.

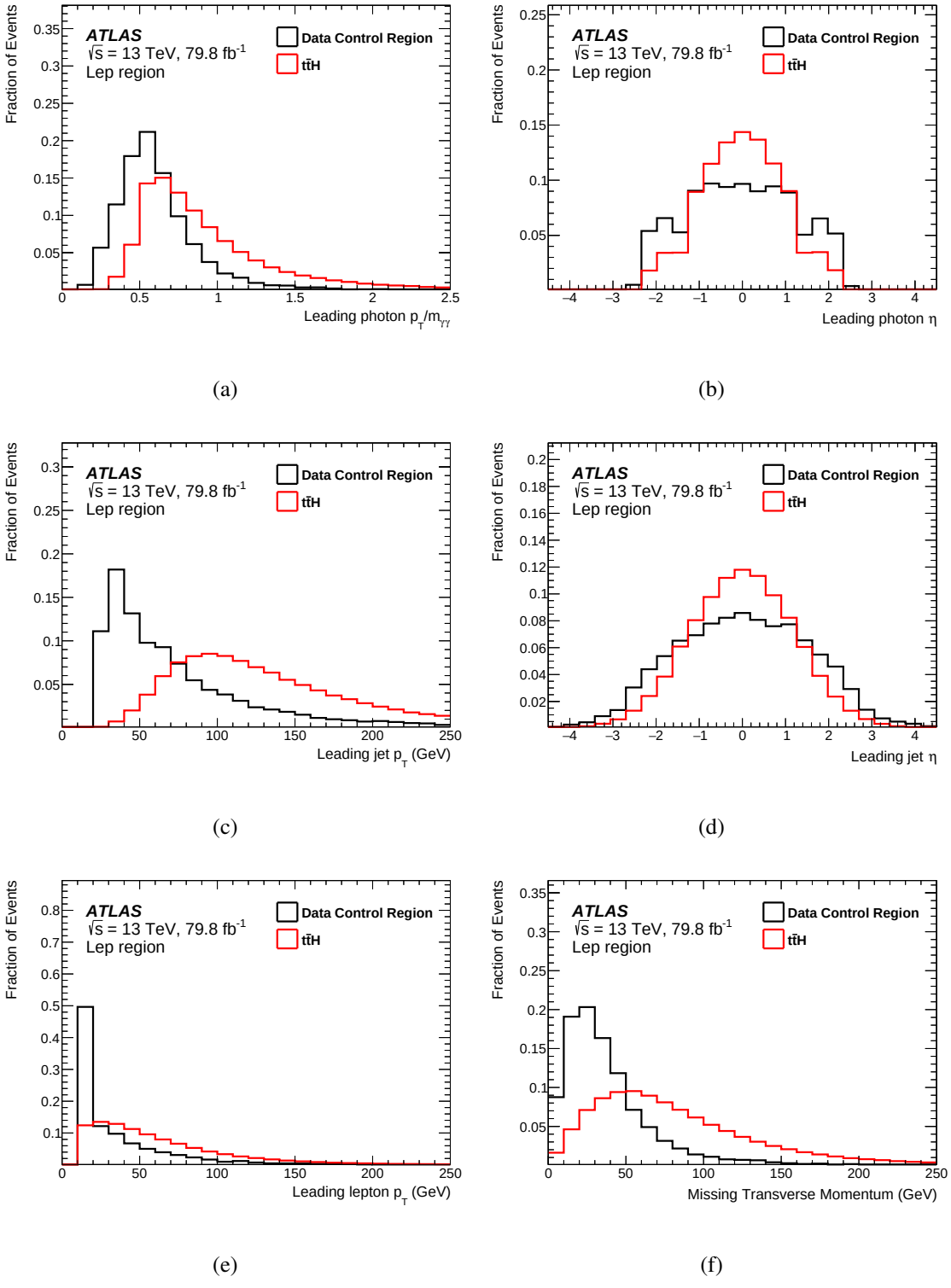

Figure 9.2: The distributions of the main BDT training variables in the **Lep** region.

Lep regions, categories are defined based on the BDT output in order to maximize the combined Asimov number counting significance.

$$Z = \sqrt{\sum_{c} 2[(s+b)\log(1+s/b) - s]} \tag{9.1}$$

For the purposes of optimization, s and b are defined as the expected number of signal and background events in a category in each category c in the $m_{\gamma\gamma} \in [123, 127]$ GeV window, a range which covers approximately 68% of the signal. s consists of the expected $t\bar{t}H$ MC yield, while $b = b_H + b_{\text{non-res}}$ consists of the expected MC yield b_H from other single Higgs processes, as well as the expected yield $b_{\text{non-res}}$ non-resonant background. In order to suppress fluctuations, $b_{\text{non-res}}$ is estimated from the expected yield in the NTI control region multiplied by a scale factor $f = \frac{4}{55}$, with the assumption that the non-resonant background is approximately flat. As $b_{\text{non-res}}$ is estimated from a control region, categories are required to have at least $b_{\text{non-res}} > 0.8$, or equivalently 9 NTI events in the sideband, as this will almost guarantee at least 2 sideband events when eventually evaluating on the data [1].

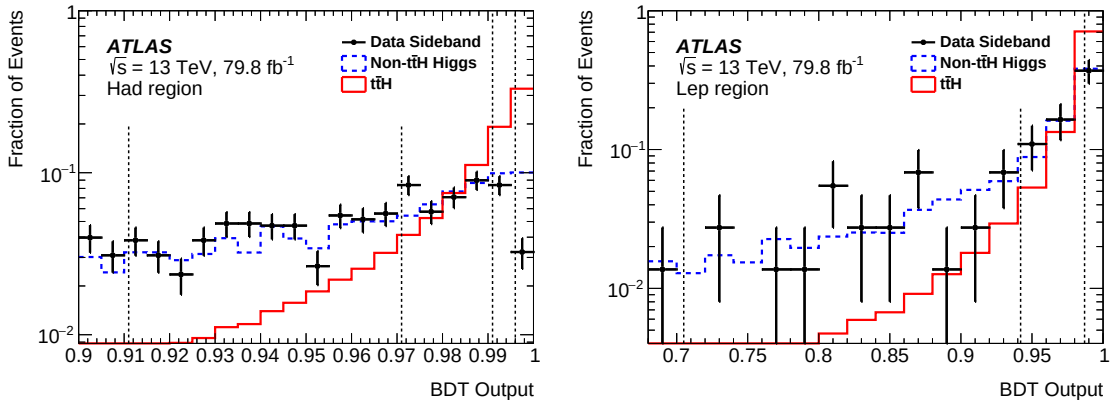

(a) (b)

Figure 9.3: The BDT output in the **Had** and **Lep** regions. The dashed lines denote the boundaries of the 7 $t\bar{t}H$ categories, with events closer to 1 being more signal-like. Events in the **Had** (**Lep**) region with score less than 0.911 (0.705) are rejected from the analysis.

[1] A poisson distribution with mean $\lambda = 9$ will have a $> 99\%$ chance of producing at least two events.

Four categories are created in the **Had** region and three in the **Lep** region. It was found that further increasing the number of categories would not bring a notable sensitivity improvement, while potentially increasing the impact of systematic uncertainties due to the addition of background-heavy categories. The categories are labelled in order of their sensitivity, with the most sensitive category defined by highest BDT scores denoted as **Had 1/Lep 1**

The final categories and their definitions are summarized in Table 9.1.

Category	Definition	
Had 1	0 leptons, ≥ 3 jets, ≥ 1 b-jet	BDT score $\in$ [0.996, 1.000]
Had 2		BDT score $\in$ [0.991, 0.996]
Had 3		BDT score $\in$ [0.971, 0.991]
Had 4		BDT score $\in$ [0.911, 0.971]
Lep 1	≥ 1 leptons, ≥ 1 b-jet	BDT score $\in$ [0.987, 1.000]
Lep 2		BDT score $\in$ [0.942, 0.987]
Lep 3		BDT score $\in$ [0.705, 0.942]

Table 9.1: The definitions of the 7 signal-sensitive categories for the $t\bar{t}H$ ($H \to \gamma\gamma$) analysis.

9.4 Signal and background modelling

In each category, the single-Higgs model is obtained from a combined DSCB fit to the sum of all Higgs production modes in each category.

The continuum background is modelled using an analytical function following the spurious signal test described in Section 6.2. Due to the low statistics available in this final state, the templates in the leptonic region are constructed from $tt\gamma\gamma$ MC samples with no photon identification or isolation cuts or MC weights applied. The templates in the hadronic region uses an enhanced version of the NTI data; in addition to the nominal NTI events, it also includes events with no b-tagged jets, and the b-tag status of all central jets in all events is set to "true". All templates are normalized to the data sideband.

Due to the low data statistics in these analyses, the test considers only exponential ($c_0 \cdot e^{c_1 m_{\gamma\gamma}}$, $c_0 \cdot e^{c_1 m_{\gamma\gamma}+c_2 m_{\gamma\gamma}^2}$, $c_0 \cdot e^{c_1 m_{\gamma\gamma}+c_2 m_{\gamma\gamma}^2+c_3 m_{\gamma\gamma}^3}$) and power-law $c_0 \cdot m_{\gamma\gamma}^{c_1}$ type functions, where c_i are constants determined from the fit. In each category, either exponential or power functions are chosen, determined by whichever has the lowest spurious signal. Using these functions, no significant spurious signal is observed after accounting for fluctuations due to low statistics in the background templates. The results are summarized in Table 9.2

Category	Function	N_{sp}
Had 1	Power	0.11
Had 2	Exponential	0.36
Had 3	Power	0.63
Had 4	Power	0.96
Lep 1	Power	0.12
Lep 2	Power	0.33
Lep 3	Exponential	0.24

Table 9.2: The results of the spurious signal test for the $t\bar{t}H$ ($H \to \gamma\gamma$) analysis, showing the chosen function and corresponding spurious signal in each category. No significant spurious signal is observed after accounting for fluctuations due to low statistics in the background templates.

9.5 $t\bar{t}H$ combination

The results from the $t\bar{t}H$ ($H \to \gamma\gamma$) analysis are combined with other Run 2 $t\bar{t}H$ measurements in the $H \to b\bar{b}$ [46], $H \to$ multilepton [47], and $H \to ZZ^{(*)} \to 4l$ channels. The $H \to$ multilepton analysis consists of the $H \to \tau^+\tau^-$, $H \to WW^{(*)}$, and $H \to ZZ^{(*)}$ final states, except in the case where $ZZ^{(*)} \to 4l$. Like $t\bar{t}H$ ($H \to \gamma\gamma$), the $H \to ZZ^{(*)} \to 4l$ analysis uses 79.8 fb^{-1} of data, while the $H \to b\bar{b}$ and $H \to$ multilepton results use only the 36.1 fb^{-1} of data taken in 2015 and 2016. The combination is achieved with the merging of the individual likelihood functions in each channel, as described in Section 8. In addition to the aforementioned Run 2 combination, a second combination is performed by adding the Run 1 $H \to$ multilepton,

$H \to b\bar{b}$, and $H \to \gamma\gamma$ channels, based on integrated luminosities of up to 4.7 fb^{-1} at $\sqrt{s} = 7$ TeV and 20.3 fb^{-1} at $\sqrt{s} = 8$ TeV.

Due to a difference in the object reconstruction and calibration procedures, most experimental uncertainties are not correlated between the between the 36.1 fb^{-1} and 79.8 fb^{-1} analyses. Almost all experimental systematic uncertainties, with the exception of the e/γ energy scale and resolution uncertainties, are decorrelated between Run 1 and Run 2 analyses. The robustness of this assumption is empirically tested by correlating or decorrelating various systematics and observing that the impact on the results is small.

9.6 $t\bar{t}H$ results

Figures 9.4 and 9.5 show the $m_{\gamma\gamma}$ distributions of the observed data in each of the seven categories for the $t\bar{t}H$ ($H \to \gamma\gamma$) analysis. Table 9.6 shows the measured $t\bar{t}H$ cross-sections and significances for the both the individual channels and combined results in the ATLAS $t\bar{t}H$ combination. No events are observed in the $H \to ZZ^{(*)} \to 4l$ channel and an upper limit at 68% CL is instead set on the $t\bar{t}H$ production cross-section.

The combined observed significance with 13 TeV data is 5.8 σ, constituting the first ever ATLAS observation of $t\bar{t}H$ production. A large part of this sensitivity is due to the $H \to \gamma\gamma$ channel, which contributes an observed significance of 4.1 σ and is tied only with the $H \to \mathrm{multilepton}$ channel. The combined 13 TeV $t\bar{t}H$ cross-section is 670 ± 90 (stat.) $^{+110}_{-100}$ (syst.) fb, in agreement with the SM value of 507^{+35}_{-50} fb. With 79.8 fb^{-1} the $H \to \gamma\gamma$ and $H \to ZZ^{(*)} \to 4l$ channels are still statistically limited and will continue improving simply by the collection of additional data even well into Run 3; in contrast, the $H \to \mathrm{multilepton}$ and $H \to b\bar{b}$ channels are already systematically limited with 36.1 fb^{-1}. Figure 9.7 shows the observed $t\bar{t}H$ cross-section split by decay channel and as a function of the centre-of-mass energy, again showing compatibility with the Standard Model.

For the $H \to \gamma\gamma$ channel, the main theoretical systematic uncertainties affecting the $t\bar{t}H$ cross-section measurement are due to parton shower modelling (8%) and the modelling uncertainty in the Higgs boson plus heavy flavour background (4%). The dominant experimental uncertainties include the reconstruction of the jet energy (5%), the photon isolation (4%), and the photon energy resolution (6%) and scale (4%).

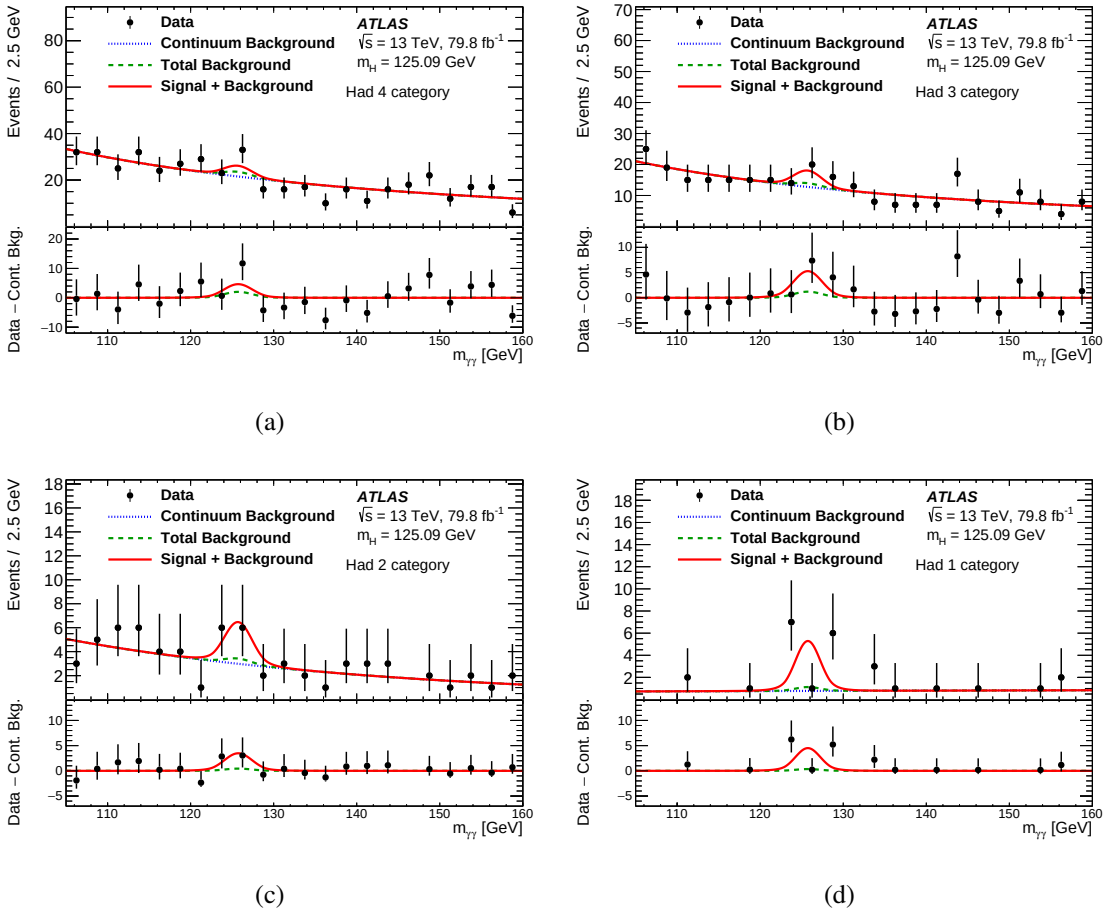

Figure 9.4: The $m_{\gamma\gamma}$ distribution in each of the four **Had** $t\bar{t}H$ ($H \to \gamma\gamma$) categories observed with 79.8 fb^{-1} of 13 TeV data. The red line shows the signal plus background fit. The blue dotted line shows the continuum background, while the green dashed line shows the total background consisting of the continuum background and non-$t\bar{t}H$ Higgs production modes. The bottom plot shows the results after subtracting the background component of the fitted model.

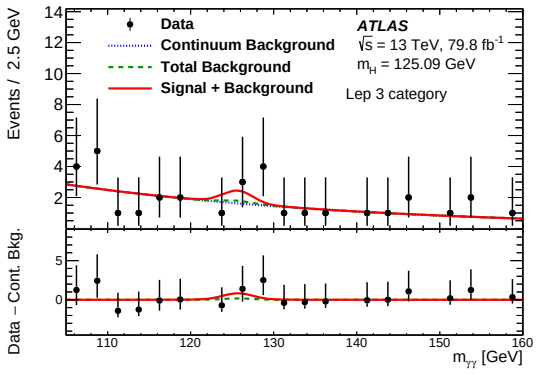

(a)

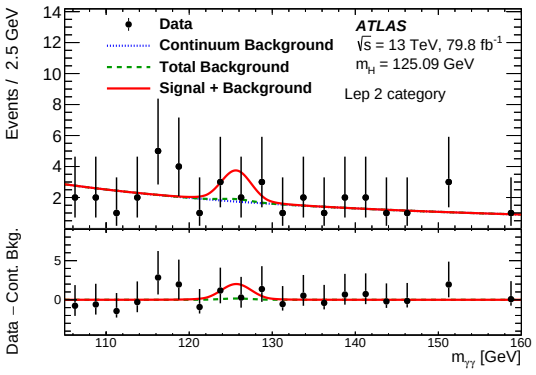

(b)

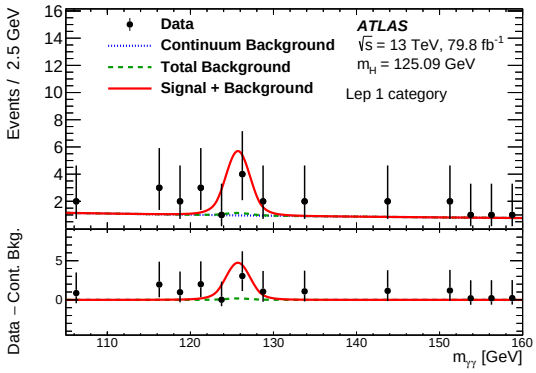

(c)

Figure 9.5: The $m_{\gamma\gamma}$ distribution in each of the three **Lep** $t\bar{t}H$ ($H \rightarrow \gamma\gamma$) categories observed with 79.8 fb^{-1} of 13 TeV data. The red line shows the signal plus background fit. The blue dotted line shows the continuum background, while the green dashed line shows the total background consisting of the continuum background and non-$t\bar{t}H$ Higgs production modes. The bottom plot shows the results after subtracting the background component of the fitted model.

Analysis	Integrated luminosity [fb^{-1}]	$t\bar{t}H$ cross section [fb]	Obs. sign.	Exp. sign.
$H \to \gamma\gamma$	79.8	710 $^{+210}_{-190}$ (stat.) $^{+120}_{-90}$ (syst.)	4.1 σ	3.7 σ
$H \to$ multilepton	36.1	790 $\pm$150 (stat.) $^{+150}_{-140}$ (syst.)	4.1 σ	2.8 σ
$H \to b\bar{b}$	36.1	400 $^{+150}_{-140}$ (stat.) $\pm$ 270 (syst.)	1.4 σ	1.6 σ
$H \to ZZ^* \to 4\ell$	79.8	<900 (68% CL)	0 σ	1.2 σ
Combined (13 TeV)	36.1$-$79.8	670 $\pm$ 90 (stat.) $^{+110}_{-100}$ (syst.)	5.8 σ	4.9 σ
Combined (7, 8, 13 TeV)	4.5, 20.3, 36.1$-$79.8	$-$	6.3 σ	5.1 σ

Figure 9.6: The measured $t\bar{t}H$ cross-sections and significances for both the individual and combined results in the ATLAS $t\bar{t}H$ combination. The $H \to$ multilepton analysis consists of the $H \to ZZ^{(*)}$(except $ZZ^{(*)} \to 4l$), $H \to WW^{(*)}$, and $H \to \tau^+\tau^-$ decay channels. No events are observed in the $H \to ZZ^{(*)} \to 4l$ channel and an upper limit at 68% CL is instead set on the $t\bar{t}H$ production cross-section. The combined observed significance with 13 TeV data is 5.8 σ, constituting the first ever ATLAS observation of $t\bar{t}H$ production. The measured 13 TeV $t\bar{t}H$ cross-section is 670 $\pm$ 90 (stat.) $^{+110}_{-100}$ (syst.) fb, in agreement with the SM value of 507^{+35}_{-50} fb.

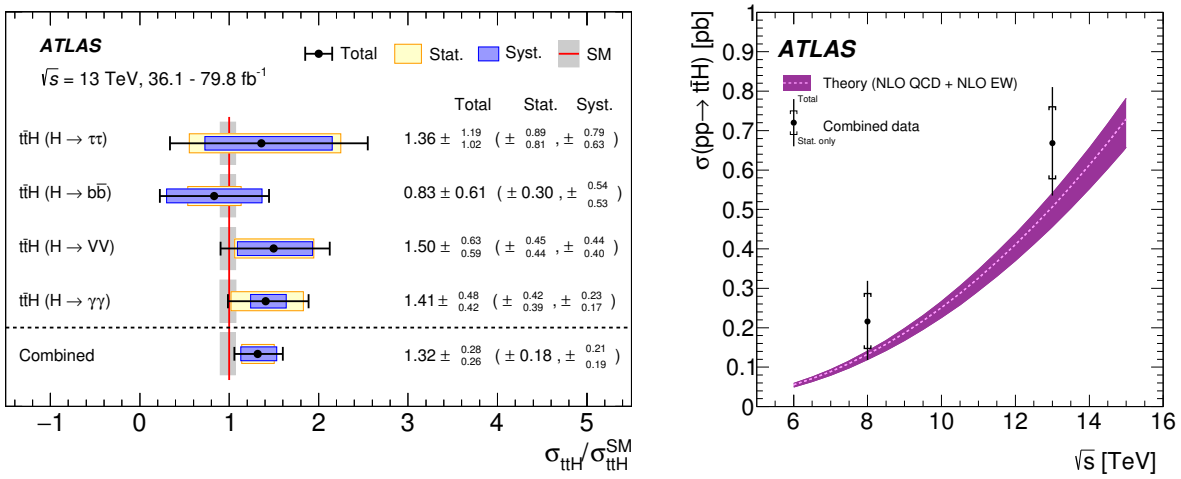

(a) (b)

Figure 9.7: (a) The observed $t\bar{t}H$ cross-section from the 13 TeV combination split by decay channel, under the assumption that the $H \to ZZ^{(*)}$and $H \to WW^{(*)}$couplings are scaled by the same factor with respect to the SM prediction. (b) The observed $t\bar{t}H$ cross-section from the 7 TeV and 13 TeV combinations, compared to the theoretical cross-section prediction and its uncertainty (purple band).

The impact of systematic uncertainties for the combined measurement are shown in Table 9.3. In the combination, the uncertainties originate primarily from the $H \to b\bar{b}$ and $H \to \mathrm{multilepton}$ channels. The largest theoretical systematic uncertainties due to modelling of the $t\bar{t}$ + heavy-flavour processes in the $H \to b\bar{b}$ analysis, and the modelling of the $t\bar{t}H$ process in all analyses. The dominant experimental uncertainties are due to the estimation of leptons from heavy-flavour decays, conversions, or misidentified hadronic jets, primarily in the $H \to \mathrm{multilepton}$ analysis, and the jet energy scale and resolution in all analyses.

Uncertainty source	$\Delta\sigma_{t\bar{t}H}/\sigma_{t\bar{t}H}$ [%]
Theory uncertainties (modelling)	11.9
$t\bar{t}$ + heavy flavour	9.9
$t\bar{t}H$	6.0
Non-$t\bar{t}H$ Higgs boson production modes	1.5
Other background processes	2.2
Experimental uncertainties	9.3
Fake leptons	5.2
Jets, $E_{\mathrm{T}}^{\mathrm{miss}}$	4.9
Electrons, photons	3.2
Luminosity	3.0
τ-lepton	2.5
Flavour tagging	1.8
MC statistical uncertainties	4.4

Table 9.3: The impact of systematic uncertainties for the combined measurement in the 13 TeV ATLAS $t\bar{t}H$ combination. Only systematic uncertainties with an impact of greater than 1% are listed. The dominant theoretical uncertainties are due to modelling of the $t\bar{t}$ + heavy-flavour processes in the $H \to b\bar{b}$ analysis, and the modelling of the $t\bar{t}H$ process in all analyses. The dominant experimental uncertainties are due to the estimation of leptons from heavy-flavour decays, conversions, or misidentified hadronic jets, primarily in the multilepton analysis, and the jet energy scale and resolution in all analyses. The MC statistical uncertainties are due to the limited number of simulated events in the $H \to b\bar{b}$ and $H \to \mathrm{multilepton}$ analyses.

Chapter 10

$HH \to b\bar{b}\gamma\gamma$

10.1 Introduction

In Run 2, the three most sensitive decay channels for HH searches are $HH \to b\bar{b}b\bar{b}$, $HH \to b\bar{b}\tau^+\tau^-$, and $HH \to b\bar{b}\gamma\gamma$, all of which rely on the high $H \to b\bar{b}$ branching ratio to maximize the cross-section of this rare process (Table 10.1). Similar to the case of $t\bar{t}H$ production, the $b\bar{b}\gamma\gamma$ channel exploits the clean diphoton trigger and excellent diphoton mass resolution to obtain extremely competitive results despite the low $H \to \gamma\gamma$ branching ratio.

Previously, ATLAS searched for HH production in the $b\bar{b}\gamma\gamma$ channel with 36.1 fb^{-1} of Run 2 data, considering only the ggF HH production mode [48]. In the 36.1 fb^{-1} analysis, no significant signal was observed; the observed (expected) 95% confidence level upper limit on the HH cross-section was 22 (28) times the SM prediction, while the Higgs trilinear coupling was constrained to the range $-8.2 < \kappa_\lambda < 13.2$ at 95% CL.

Compared to the previous 36.1 fb^{-1} analysis, the $b\bar{b}\gamma\gamma$ analysis presented in this thesis [49] offers a re-optimized search strategy with the full Run 2 dataset of 139 fb^{-1}. For the first time, both ggF and VBF HH production modes are considered; however, the optimization of the event selection still focuses primarily on ggF HH as the dominant production mode. Other rare HH processes such HHV and $ttHH$ are omitted. Furthermore it is assumed that the only BSM physics enters through the value of κ_λ and other couplings such as the Higgs-top Yukawa coupling are set to their SM values.

10.2 Data and simulation samples

The dataset used for the ATLAS $b\bar{b}\gamma\gamma$ analysis corresponds to 139 fb^{-1} of pp collision data at $\sqrt{s} = 13$ TeV collected from 2015 to 2018.

Branching Ratio	$b\bar{b}$	W^+W^-	$\tau^+\tau^-$	Z^+Z^-	$\gamma\gamma$
$b\bar{b}$	33%				
W^+W^-	25%	4.6%			
$\tau^+\tau^-$	7.4%	2.5%	0.39%		
Z^+Z^-	3.1%	1.2%	0.34%	0.076%	
$\gamma\gamma$	0.26%	0.10%	0.029%	0.013%	0.0005%

Table 10.1: The branching ratios of various HH decay channels. With Run 2 data, the three most sensitive HH channels are $HH \to b\bar{b}b\bar{b}$, $HH \to b\bar{b}\tau^+\tau^-$, and $HH \to b\bar{b}\gamma\gamma$.

Simulated ggF HH samples were generated at QCD next-to-leading-order with finite top-quark mass in real and virtual corrections (NLO FT) [50] with POWHEGBOX [v2] [51]. PYTHIA8 [8] was used for parton showering, hadronization, and underlying event simulation. ggF HH samples for other values of κ_λ were obtained by a reweighting method [52]. Starting from base SM samples of κ_λ = 0, 1, and 20, weights were derived in bins of the di-Higgs invariant mass m_{HH} and applied to the base SM sample to produce distributions of kinematic variables corresponding to any other value of κ_λ. The reweighting procedure was validated by comparing the event yields and relevant kinematic distributions of the sample generated with κ_λ = 10 to a sample generated with κ_λ = 1 and reweighted to $\kappa_\lambda = 10$. An additional uncertainty of a few percent on the yields is introduced to cover the small differences observed. VBF HH samples were generated at LO using MADGRAPH5_AMC@NLO 2.6.0 [53]. Samples were generated for κ_λ = 0, 1, 2, and 10. Finally, smooth parametrizations of the expected ggF and VBF yields as a function of κ_λ are obtained by performing quadratic fits in each analysis category.

The list of single-Higgs samples is overall similar to that used for the $t\bar{t}H$ ($H \to \gamma\gamma$) analysis. ggH, VBF, WH, ZH, $t\bar{t}H$, and $b\bar{b}H$ were generated using POWHEG and showered with PYTHIA, while tH samples were generated using MADGRAPH5_AMC@NLO and showered with PYTHIA. A background sample of $\gamma\gamma$ + jets generated and showered with SHERPA was used to represent the continuum background in the optimization of the event selection and evaluating the spurious signal uncertainty, but was otherwise not used for any statistical results.

Similar to the $t\bar{t}H$ ($H \to \gamma\gamma$) analysis, the cross-sections of the generated single-Higgs and di-Higgs samples were normalized to the latest theoretical predictions. The single-Higgs samples were passed through GEANT4 [44] to simulate the response of the ATLAS detector, while the HH signal and $\gamma\gamma$ + jets samples were instead processed by ATLFASTII [45].

10.3 Event Selection

The $b\bar{b}\gamma\gamma$ categorization strategy aims to achieve excellent sensitivity to the SM HH signal hypothesis without compromising the sensitivity to BSM HH κ_λ signals.

Similar to the $t\bar{t}H$ ($H \to \gamma\gamma$) analysis, the $b\bar{b}\gamma\gamma$ analysis requires two tight, isolated photons with $p_{\mathrm{T}}/m_{\gamma\gamma} > 35\%(25\%)$ and $105 < m_{\gamma\gamma} < 160$ GeV. In addition, events must contain two b-jets tagged passing the 77% working point. The b-jets are ranked by the tightest b-tagging working

point they pass, with ties broken by p_{T}, and it is assumed that the two highest-ranked b-jets are the result from the $H \to b\bar{b}$ decay. To reduce background contamination from hadronic or leptonic $t\bar{t}H$ decays, events must have less than 6 central jets and 0 leptons. Finally, events with three or more b-jets tagged at 77% WP are rejected to maintain orthogonality with the $HH \to b\bar{b}b\bar{b}$ analysis.

As the relative contributions from the different production diagrams differ as a function of the four body mass $m_{b\bar{b}\gamma\gamma}$, this variable can be used as a useful proxy to the value of κ_λ. In particular, ggF HH signals with large $|\kappa_\lambda|$ will generally have a softer $m_{b\bar{b}\gamma\gamma}$ spectrum than signals with small $|\kappa_\lambda|$ due to the larger contribution from the triangle diagram [15].

In practice, the modified four-body mass

$$m^*_{b\bar{b}\gamma\gamma} = m_{b\bar{b}\gamma\gamma} - (m_{\gamma\gamma} - 125\ \mathrm{GeV}) - (m_{b\bar{b}} - 125\ \mathrm{GeV}) \tag{10.1}$$

is used instead due to the cancellation of detector resolution effects. Events with $m^*_{b\bar{b}\gamma\gamma} > 350$ GeV are classified into the **High Mass** region, which primarily targets SM-like signals, while events with $m^*_{b\bar{b}\gamma\gamma} < 350$ GeV are classified into the **Low Mass** region, which offers additional sensitivity for non-SM-like signals. Figure 10.1 illustrates the $m^*_{b\bar{b}\gamma\gamma}$ distributions for the ggF and VBF HH signals with a variety of κ_λ assumptions.

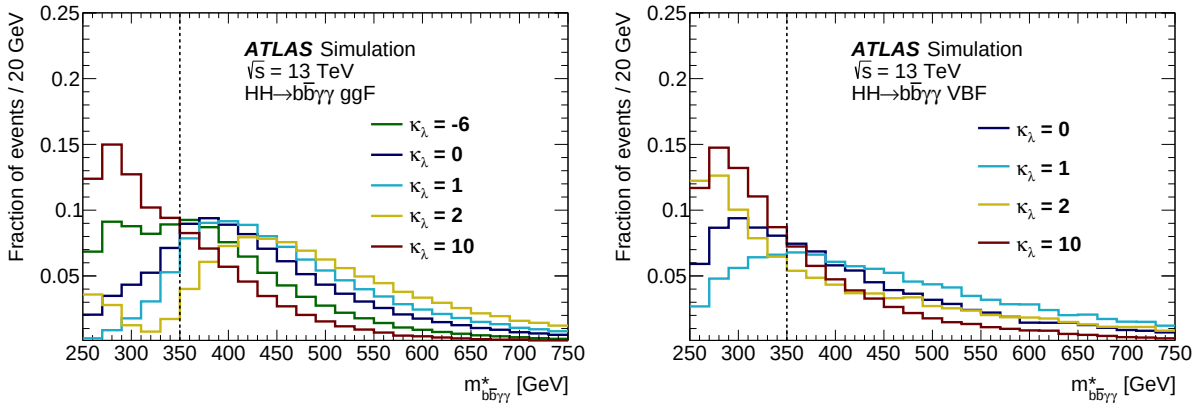

(a) (b)

Figure 10.1: The modified four-body invariant mass, as defined in Equation 10.1 for (a) ggF and (b) VBF HH signals for a variety of κ_λ assumptions. The dashed line at $m^*_{b\bar{b}\gamma\gamma}$ = 350 GeV denotes the boundary between the **High Mass** or **Low Mass** regions.

In each region, a separate boosted decision tree (BDT) is trained on MC to separate the HH signal from the various backgrounds. The **High Mass** (**Low Mass**) region uses the ggF HH $\kappa_\lambda = 1$ (HH $\kappa_\lambda = 10$) sample as the training signal, while the background consists of a mix of $\gamma\gamma$ (representing the continuum background) and the major single-Higgs backgrounds, ggH, ZH, and $t\bar{t}H$. For training purposes only, the signals and backgrounds are normalized not according to their cross-sections but to a set of empirically-optimized weights. The same set of kinematic variables are used in both regions:

- The $p_{\mathrm{T}}/m_{\gamma\gamma}, \eta, \phi^*$ of the two photons
- The $p_{\mathrm{T}}, \eta, \phi^*$, and pseudo-continuous b-tagging score of the two jets
- The $p_{\mathrm{T}}, \eta, \phi^*$, and mass of the $H \to b\bar{b}$ candidate
- $E_{\mathrm{T}}^{\mathrm{miss}}$ and $(\phi^{\mathrm{miss}})^*$, the magnitude and ϕ angle of the missing transverse momentum
- H_{T}, the scalar sum of the p_{T} of all jets
- The "single topness", $\chi_{Wt} = \min\sqrt{(\frac{m_{j_1 j_2} - m_W}{m_W})^2 + (\frac{m_{j_1 j_2 j_3} - m_t}{m_t})^2}$, where $m_W = 80\,\mathrm{GeV}$, $m_t = 173\,\mathrm{GeV}$, and the minimum is taken over all possible combinations of 3 jets in the event.

To remove one extra degree of freedom, all vectors in an event are rotated in the $R - \phi$ plane so that the azimuthal angle of the leading photon is equal to 0, and the resulting azimuthal angle is denoted as ϕ^*.

Figures 10.2, 10.3, 10.4, 10.5, 10.6, and 10.4 demonstrate the effectiveness of these training variables at separating different kinds of background in the **High Mass** and **Low Mass** regions. In particular, the $E_{\mathrm{T}}^{\mathrm{miss}}$, H_{T}, and χ_{Wt} variables are specifically designed to control the $t\bar{t}H$ contamination, which is in general a difficult background to reject to its similar final state as the signal.

The BDT score distributions in the **High Mass** and **Low Mass** regions after the training is shown in Figure 10.8. After training, in each mass region, two categories are defined by selections on the BDT output, in order to maximize the expected significance

$$Z = \sqrt{\sum_c 2[(s+b)\log(1+s/b) - s]} \tag{10.2}$$

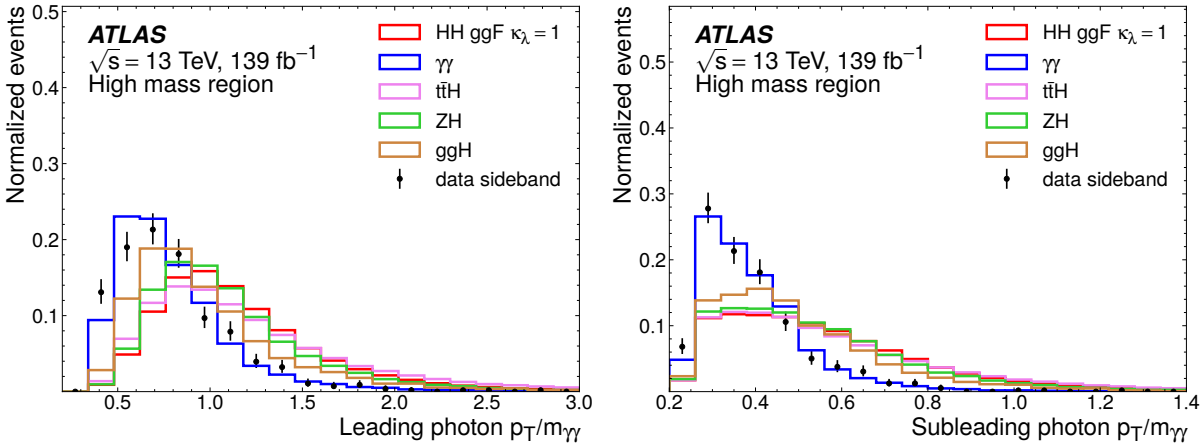

(a) (b)

Figure 10.2: The distributions of the main photon training variables in the **High Mass** region.

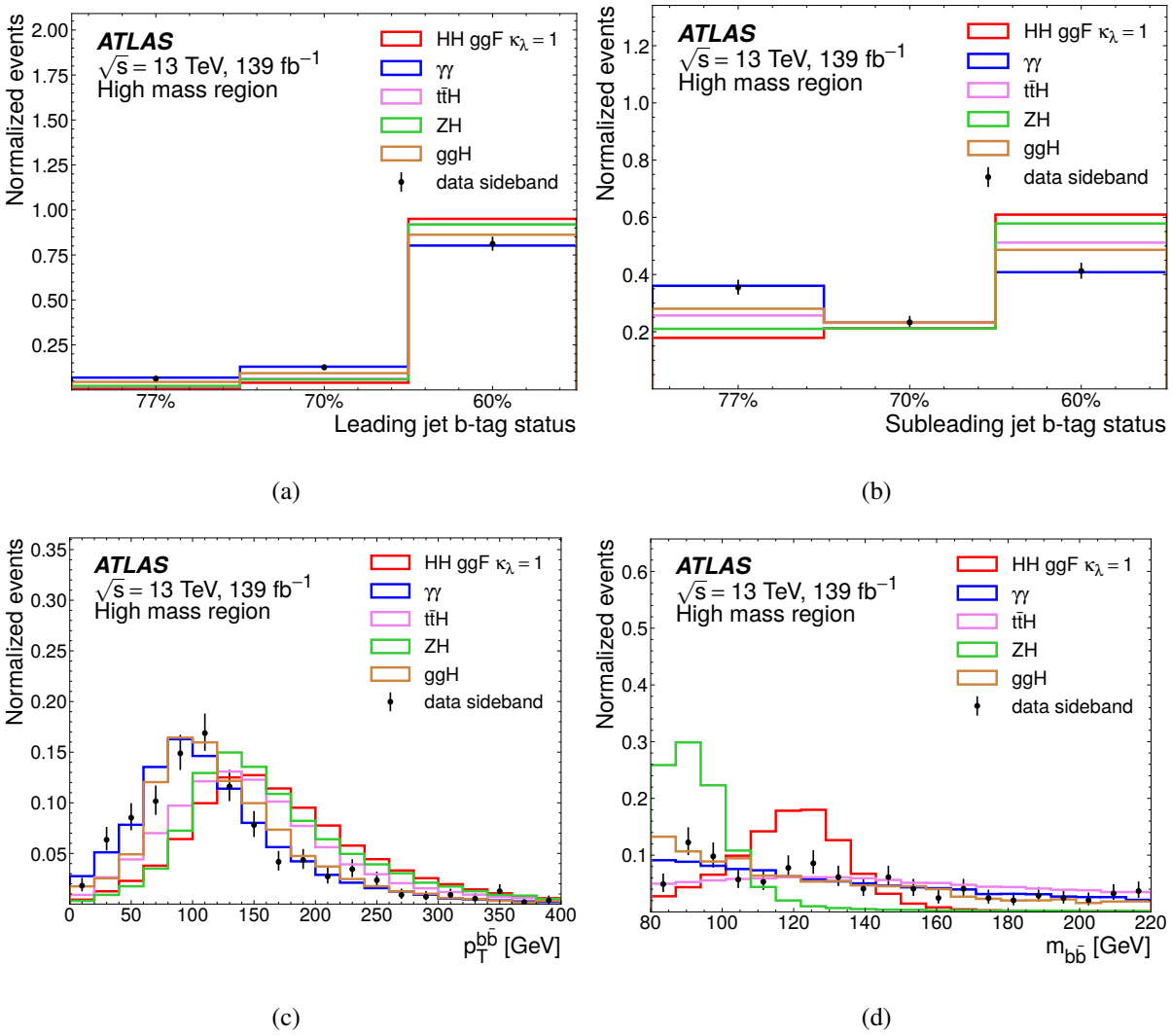

Figure 10.3: The distributions of the main jet training variables in the **High Mass** region.

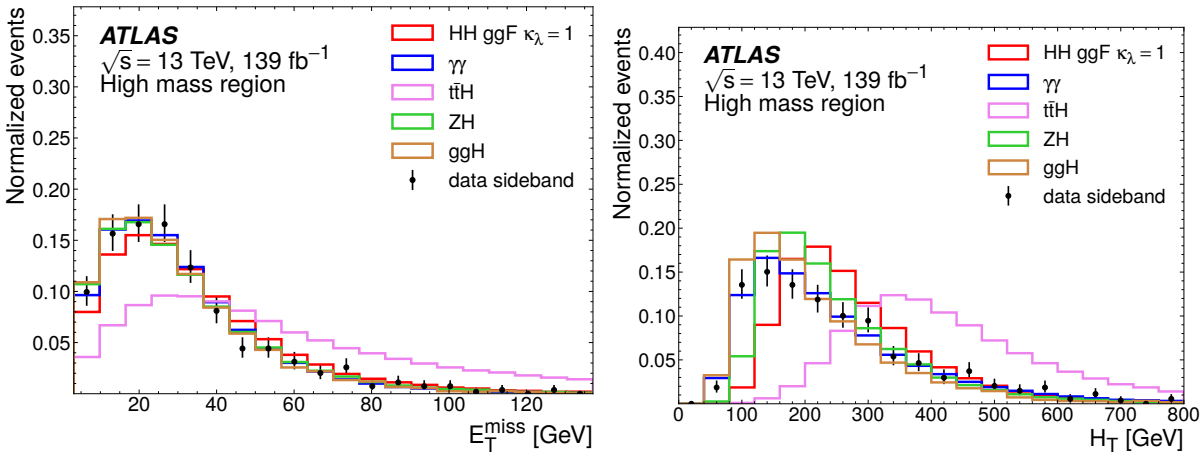

(a)

(b)

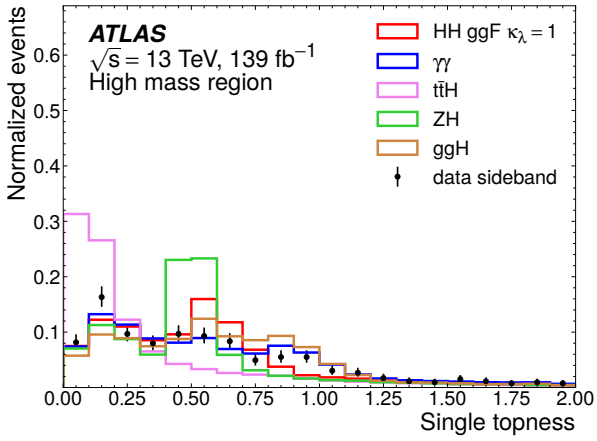

(c)

Figure 10.4: The distributions of the main training variables for rejecting $t\bar{t}H$ in the **High Mass** region.

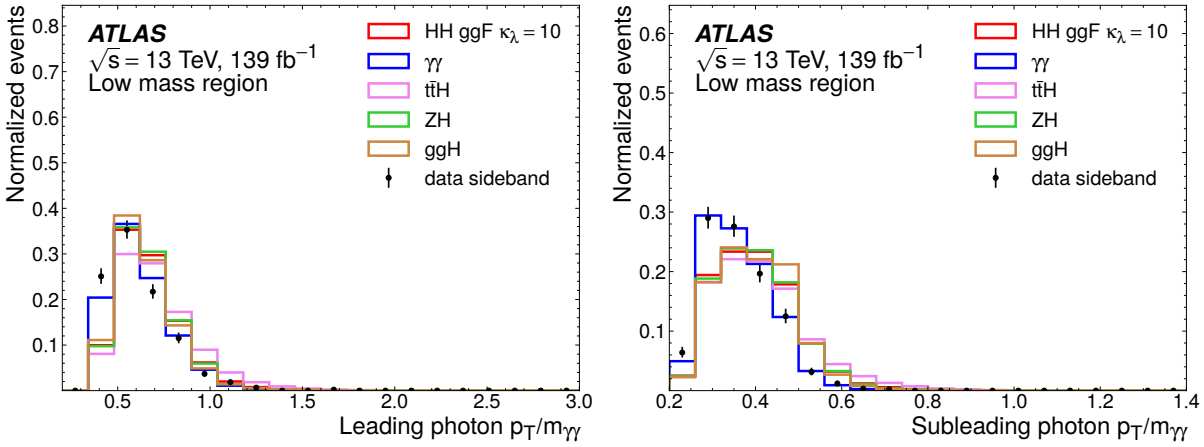

(a) (b)

Figure 10.5: The distributions of the main photon training variables in the **Low Mass** region.

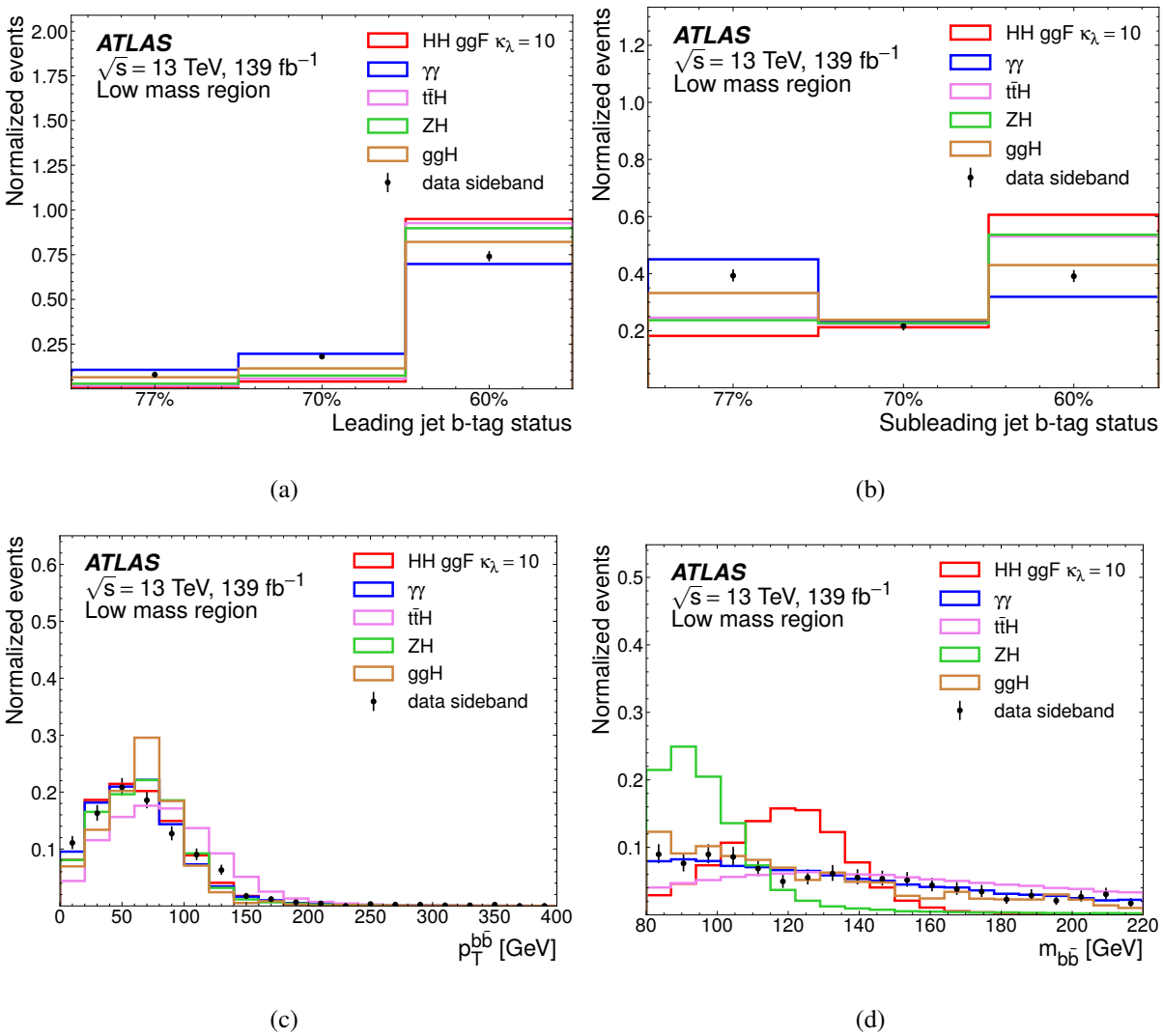

Figure 10.6: The distributions of the main jet training variables in the **Low Mass** region.

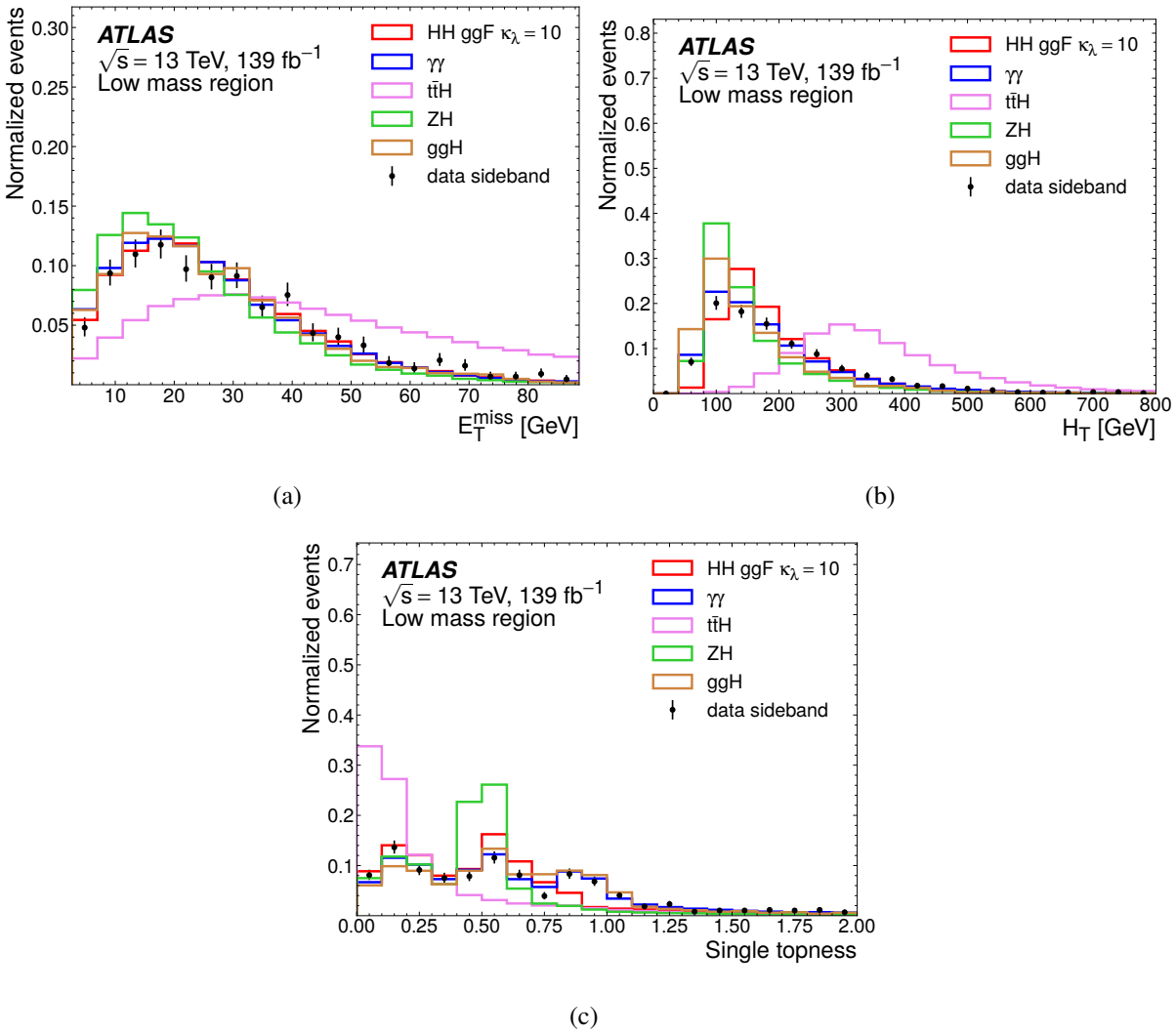

(a) (b)

(c)

Figure 10.7: The distributions of the main training variables for rejecting $t\bar{t}H$ in the **Low Mass** region.

where s and b are the expected number of signal and background events in the $m_{\gamma\gamma} \in [120, 130]$ GeV range in a category c. The expected background b is obtained from the sum of single-Higgs events and the continuum background estimated from the $\gamma\gamma$ + jet sample; to improve statistics, the continuum background yield is evaluated in the window $[105, 160]$ GeV and scaled by $10/55$ under the assumption that its shape is sufficiently flat. Similar to the case with the $t\bar{t}H$ ($H \to \gamma\gamma$) analysis, a minimum number of 9 expected sideband events is required in each category in order to ensure sufficient events when applying the categorization model to the data.

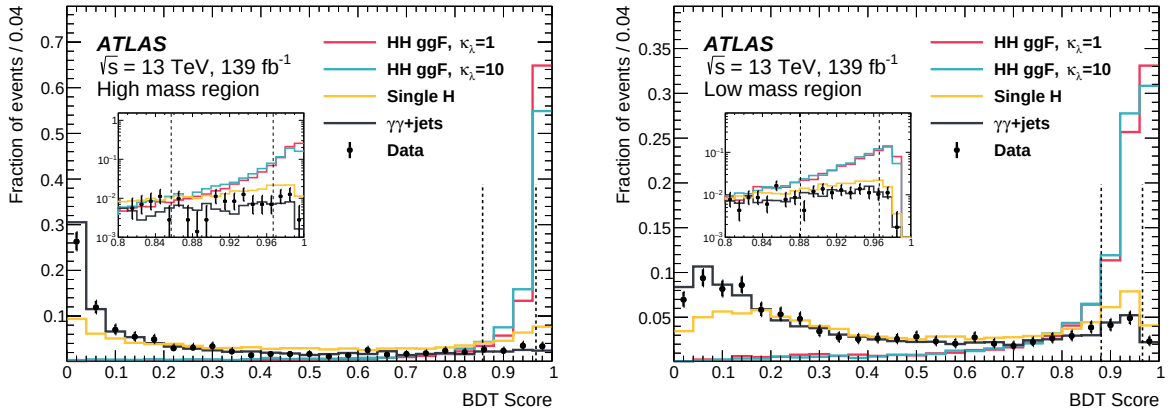

(a) (b)

Figure 10.8: The BDT distribution after training in (a) the **High Mass** and (b) the **Low Mass** regions for the two benchmark HH signals and backgrounds. The continuum background is represented in training by the $\gamma\gamma$ + jets MC; the data points are provided only as validation. The dashed lines indicate the boundaries between the categories as defined in Table 10.2. Events in the **High Mass** (**Low Mass**) region with score less than 0.881 (0.857) are rejected. The inset plot provides an enlarged view of the high-score area. Distributions are normalized to unit area.

The definitions of the four categories are summarized in Table 10.2. Figure 10.9 shows the expected significance in each of the four categories for the two benchmark scenarios - κ_λ = 1 and κ_λ = 10. As expected, while the sensitivity to κ_λ = 1 is almost completely driven by the **High Mass** BDT tight category, the sensitivity to κ_λ = 10 is comparatively more distributed among the **High Mass** and **Low Mass** regions.

Category	Selection criteria
High Mass BDT tight	$m^*_{b\bar{b}\gamma\gamma} \geq 350$ GeV, BDT score $\in [0.967, 1]$
High Mass BDT loose	$m^*_{b\bar{b}\gamma\gamma} \geq 350$ GeV, BDT score $\in [0.857, 0.967]$
Low Mass BDT tight	$m^*_{b\bar{b}\gamma\gamma} < 350$ GeV, BDT score $\in [0.966, 1]$
Low Mass BDT loose	$m^*_{b\bar{b}\gamma\gamma} < 350$ GeV, BDT score $\in [0.881, 0.966]$

Table 10.2: Definition of the categories used in the $b\bar{b}\gamma\gamma$ analysis. Before entering the BDT-based categories, events must satisfy the preselection requirements.

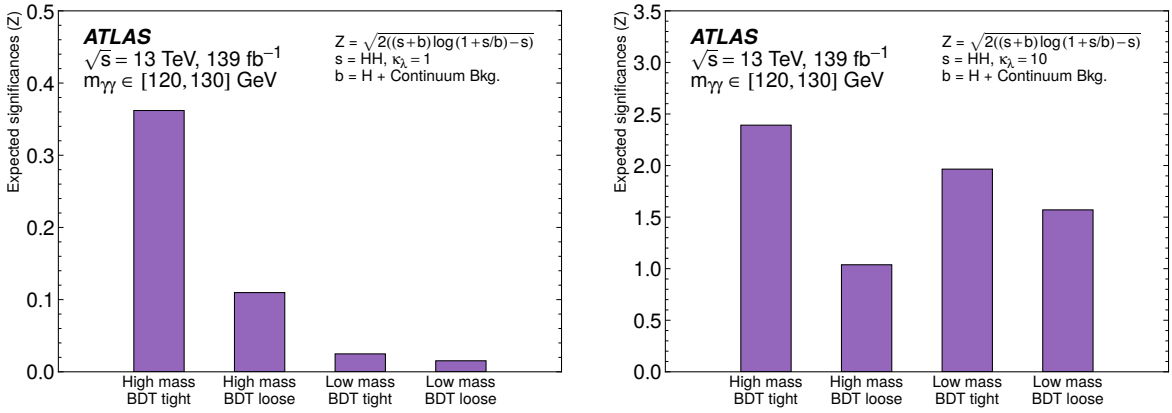

(a) (b)

Figure 10.9: The expected discovery significance in each of the four categories for (a) the SM κ_λ = 1 and (b) the κ_λ = 10 benchmark scenario.

10.4 Signal and background modelling

The signal model in each category is obtained by fitting the sum of the SM ggF and VBF HH signals to a DSCB function following the procedure in Section 6.1. In order to simplify the statistical model, the same fitted model parameters are also used for single-Higgs backgrounds and BSM di-Higgs signals. No significant bias was observed compared to an alternative approach in which single-Higgs and BSM di-Higgs were separately modelled. Table 10.3 shows the DSCB σ value as an approximate indication of the signal width in each category.

Category	σ_{DSCB} [GeV]
High Mass BDT tight	1.33 ± 0.01
High Mass BDT loose	1.47 ± 0.02
Low Mass BDT tight	1.50 ± 0.06
Low Mass BDT loose	1.64 ± 0.03

Table 10.3: The resolution parameter of the double-sided Crystal Ball functional form and corresponding statistical uncertainty for simulated Higgs boson pair events for the four $b\bar{b}\gamma\gamma$ categories.

In order to evaluate the uncertainty in the continuum background due to the spurious signal, background templates are constructed using the simulated $\gamma\gamma$ + jets samples. Due to the statistical uncertainties, the relaxed spurious signal condition is used - no significant spurious signal is observed after accounting for the fluctuations in the MC template. In each category, an exponential function is chosen due to the low associated bias and its low number of degrees of freedom.

10.5 $HH \to b\bar{b}\gamma\gamma$ results

A small but non-significant deficit of events in the signal region is observed, especially in the **High Mass** BDT tight category. The observed (expected) 95% CL upper limit on the signal strength is 4.2 (5.7). Limits are also set directly on the HH cross-section, yielding an observed (expected) 95% CL upper limit of 130 fb^{-1} (180 fb^{-1}). Figure 10.10 shows the observed $m_{\gamma\gamma}$

distribution in each of the categories. Table 10.4 summarizes the number of events from simulation and observed data in each category in the $120 < m_{\gamma\gamma} < 130$ GeV signal region.

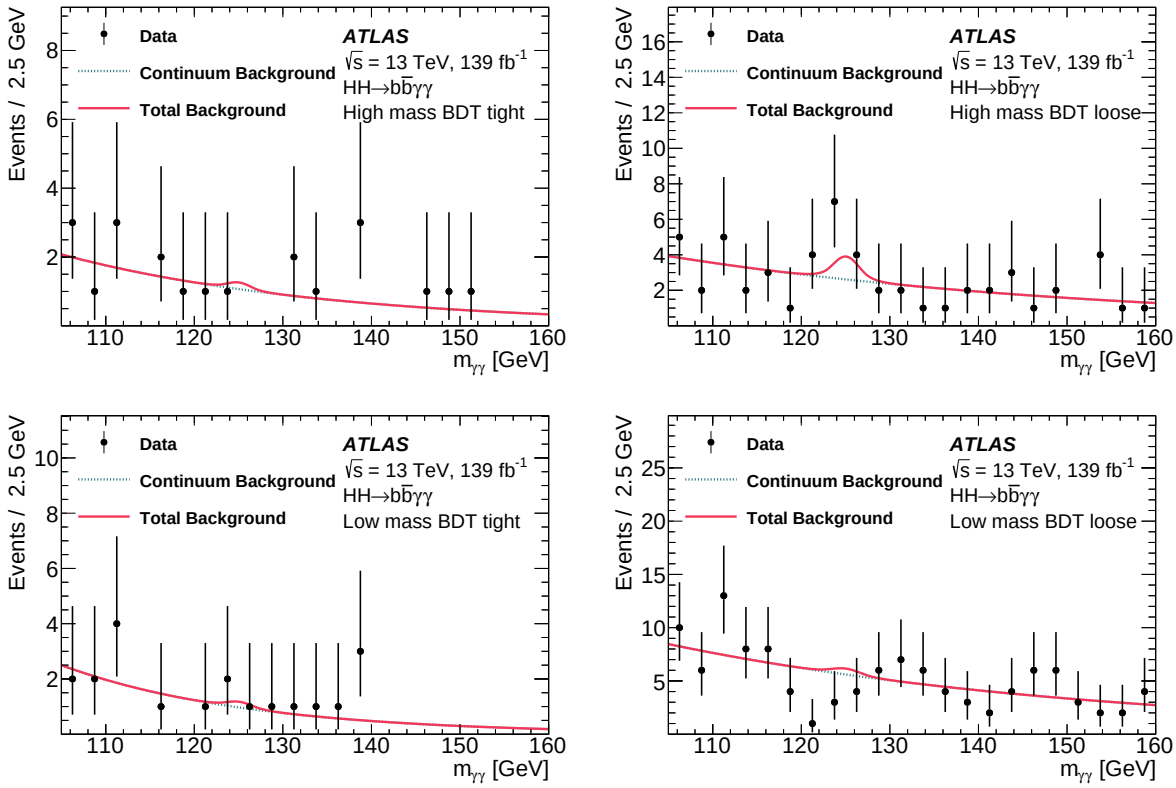

Figure 10.10: The $m_{\gamma\gamma}$ distribution of the observed data in each of the $b\bar{b}\gamma\gamma$ analysis categories. No significant excess is observed. The observed (expected) 95% CL upper limit on the signal strength is 4.2 (5.7). The red line shows the result of a background-only fit while the green dotted line shows the contribution from the continuum background. The peak near 125 GeV is due to single-Higgs background and not the HH signal.

Figure 10.11 shows the 95% CL upper limit on the HH cross-section as a function of κ_λ; the intersection between the theoretical cross-section and the limit curve results in an observed (expected) constraint of [-1.5, 6.7] ([-2.4, 7.7]) on the value of κ_λ. The expected constraints are obtained using a background hypothesis with no HH production. The inclusion of the VBF HH production affects the κ_λ constraint by approximately 5% compared to an alternative fit with only ggF HH. Figure 10.12 shows an alternative set of constraints on κ_λ based on the negative log-likelihood. The expected constraint on κ_λ is obtained using a hypothesis assuming SM HH

	High Mass BDT tight	High Mass BDT loose	Low Mass BDT tight	Low Mass BDT loose
Continuum background	$4.9^{+1.1}_{-1.3}$	$9.5^{+1.5}_{-1.7}$	$3.7^{+0.9}_{-1.1}$	$24.9^{+2.3}_{-2.5}$
Single Higgs boson background	$0.67^{+0.29}_{-0.13}$	$1.6^{+0.6}_{-0.2}$	$0.23^{+0.09}_{-0.03}$	$1.40^{+0.33}_{-0.16}$
ggF+bbH	$0.26^{+0.28}_{-0.16}$	$0.4^{+0.5}_{-0.2}$	$0.07^{+0.08}_{-0.04}$	$0.27^{+0.27}_{-0.16}$
$t\bar{t}H$	$0.19^{+0.03}_{-0.03}$	$0.49^{+0.09}_{-0.07}$	$0.107^{+0.022}_{-0.017}$	$0.75^{+0.13}_{-0.11}$
ZH	$0.142^{+0.035}_{-0.025}$	$0.48^{+0.09}_{-0.07}$	$0.040^{+0.020}_{-0.014}$	$0.27^{+0.06}_{-0.04}$
Rest	$0.074^{+0.032}_{-0.014}$	$0.16^{+0.07}_{-0.03}$	$0.012^{+0.008}_{-0.004}$	$0.111^{+0.030}_{-0.012}$
SM $HH(\kappa_\lambda = 1)$ signal	$0.87^{+0.10}_{-0.18}$	$0.37^{+0.04}_{-0.07}$	$0.049^{+0.006}_{-0.010}$	$0.078^{+0.008}_{-0.015}$
ggF	$0.86^{+0.10}_{-0.18}$	$0.35^{+0.04}_{-0.07}$	$0.046^{+0.006}_{-0.010}$	$0.072^{+0.008}_{-0.015}$
VBF	$(12.6^{+1.3}_{-1.2}) \cdot 10^{-3}$	$(16.1^{+1.4}_{-1.2}) \cdot 10^{-3}$	$(3.2^{+0.4}_{-0.4}) \cdot 10^{-3}$	$(6.9^{+0.5}_{-0.6}) \cdot 10^{-3}$
Alternative $HH(\kappa_\lambda = 10)$ signal	$6.5^{+1.0}_{-0.8}$	$3.6^{+0.6}_{-0.4}$	$4.5^{+0.7}_{-0.6}$	$8.5^{+1.3}_{-1.0}$
Data	2	17	5	14

Table 10.4: The number of events from observed data and events expected from simulation in each of the $b\bar{b}\gamma\gamma$ categories in the $120 < m_{\gamma\gamma} < 130$ GeV signal region.

production; because of this and other slightly different statistical assumptions, the results are not directly comparable to that of Figure 10.11. Of particular note in the likelihood scan is that due to the deficit observed in the data, the most probable value of κ_λ occurs at approximately 3, corresponding to the minimum possible cross-section times selection efficiency.

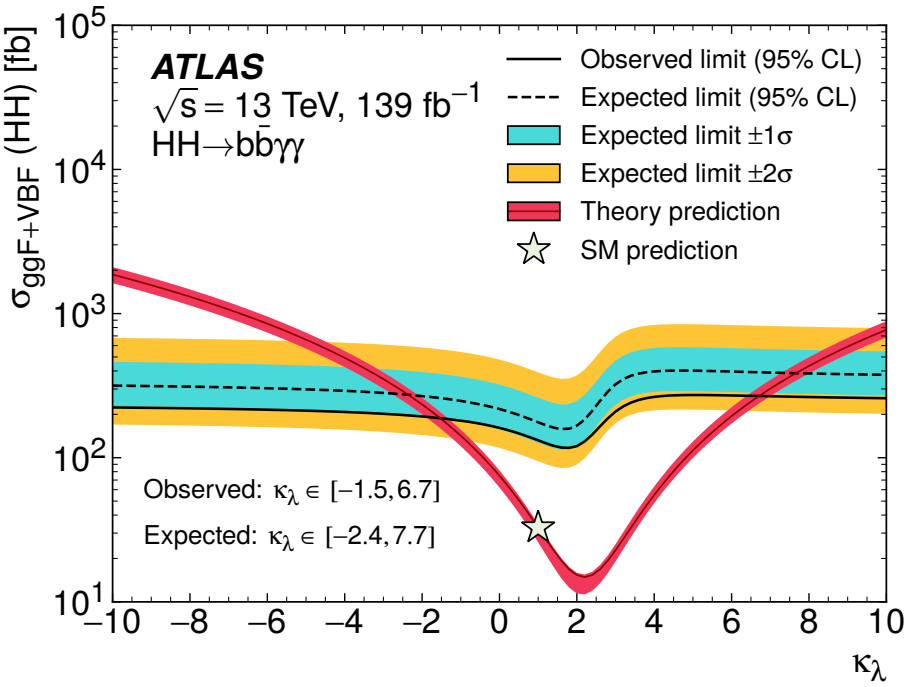

Figure 10.11: The observed and expected 95% CL limits on the HH cross-section as a function of κ_λ. The expected results are obtained under the background hypothesis that the HH cross-section is zero. The blue (yellow) bands about the expected limit denote the $\pm1\sigma$ ($\pm2\sigma$) variations due to statistical and systematic uncertainties. The red band shows the value and uncertainty of the HH cross-section predicted by theory. It is assumed that all couplings except κ_λ are equal to their SM values.

Compared to the previous ATLAS $b\bar{b}\gamma\gamma$ search with 36.1 fb^{-1}, the limit on the production cross-section improved by a factor of five, and the κ_λ constraint range improved by a factor of 2. The improvement is due partially due to the increase in luminosity but also due to the use of a new categorization strategy based on multi-variate techniques and better object reconstruction and calibration.

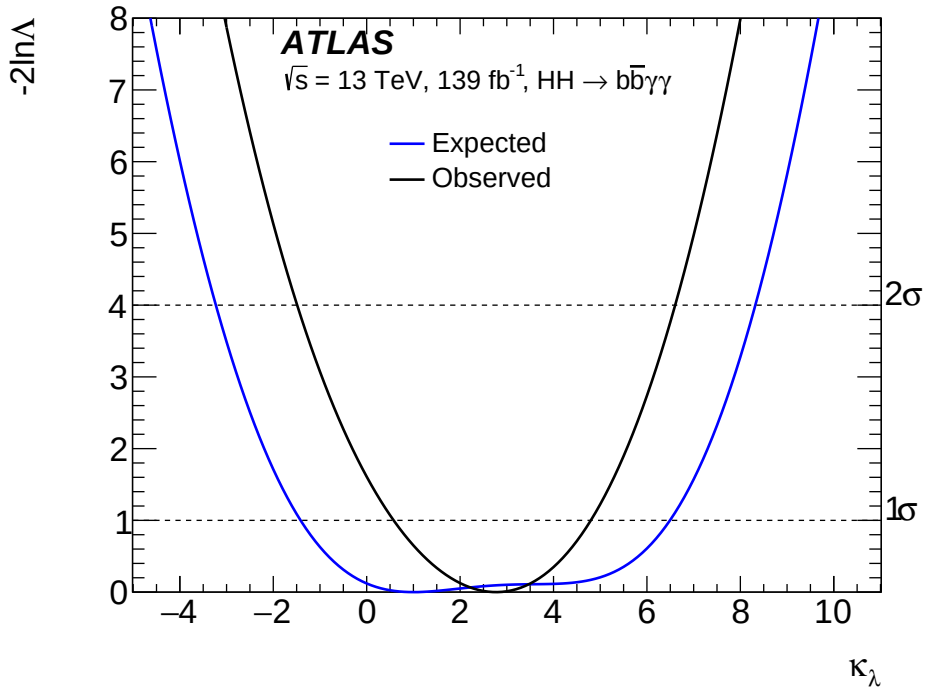

Figure 10.12: The observed and expected negative log-likelihood ratios as a function of κ_λ. The expected results are obtained from an Asimov data set generated under the SM hypothesis. The dashed horizontal lines indicate the values of the negative log-likelihood ratio corresponding to the 1σ and 2σ confidence levels. It is assumed that all couplings except κ_λ are equal to their SM values. Due to the deficit observed in the data, the most probable value of κ_λ occurs at approximately 3, corresponding to the minimum possible cross-section times selection efficiency.

Table 10.5 shows the the impact of various systematic uncertainties on the expected 95% upper limit on the HH cross-section. While the spurious signal uncertainty is one of the largest systematic uncertainties, its impact on the overall results is still small as the the analysis is almost entirely statistically limited. Other important systematic uncertainties include the photon energy resolution and the parton showering model.

Source	Type	Relative impact of the systematic uncertainties [%]
Experimental		
Photon energy resolution	Norm. + Shape	0.4
Theoretical		
Factorization and renormalization scale	Normalization	0.3
Parton showering model	Normalization	0.6
Heavy-flavor content	Normalization	0.3
$\mathcal{B}(H \to \gamma\gamma, b\bar{b})$	Normalization	0.2
Spurious signal	Normalization	3.0

Table 10.5: The impact of various systematic uncertainties on the expected 95% upper limit on the HH cross-section, calculated by re-evaluating the limits after fixing the relevant nuisance parameters to their best fit values while floating the remaining nuisance parameters. Systematic uncertainties with an impact of $< 0.2\%$ are omitted. The majority of the systematic uncertainties have a negligible effect on the $m_{\gamma\gamma}$ shape and consequently only affect the normalization of the signal and background processes.

10.6 HH and H combination

The results in the $b\bar{b}\gamma\gamma$ channel are extremely competitive with the $b\bar{b}\tau^+\tau^-$ and $b\bar{b}b\bar{b}$ channels, which used a similar dataset to observe signal strength limits of 4.7 and 5.4 [54]. A statistical combination of all three channels resulted in an observed signal strength limit of 2.4, as shown in Figure 10.13. In addition, Figure 10.14 shows the likelihood scan for κ_λ from the combination of

the three HH channels; the observed (expected) 95% CL constraint on κ_λ is found to be $-0.6 < \kappa_\lambda < 6.6$ $(-2.1 < \kappa_\lambda < 7.8)$, with an observed best-fit value of $\kappa_\lambda = 3.1$.

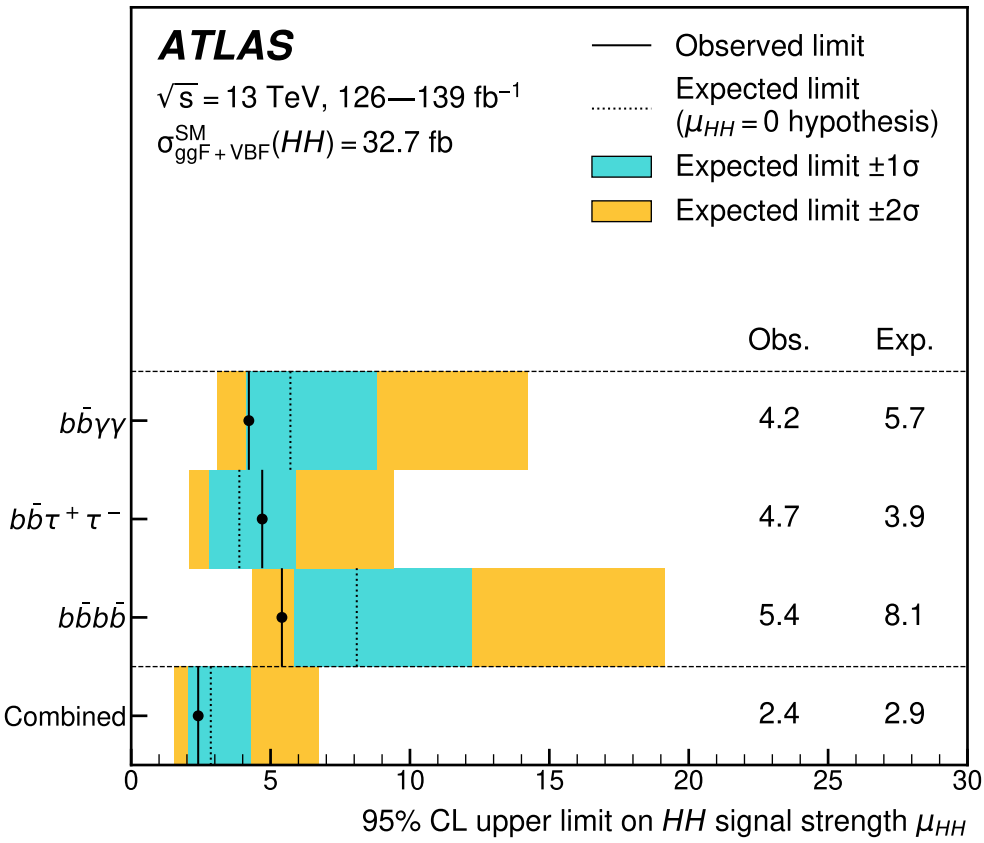

Figure 10.13: The observed and expected 95% CL upper limits on the HH signal strength from the individual $b\bar{b}b\bar{b}$, $b\bar{b}\tau^+\tau^-$, and $b\bar{b}\gamma\gamma$ channels and their combination. The expected limits are obtained under the assumption of no HH production.

Finally, the constraints on κ_λ can be further enhanced by yet another combination with analyses targeting single-Higgs boson production in the $\gamma\gamma$, Z^+Z^-, W^+W^-, $\tau^+\tau^-$, and $b\bar{b}$ decay channels, as summarized in Table 10.6. Figure 10.15 shows that under the assumption that the other coupling modifiers $\kappa_t, \kappa_V, \kappa_b, \kappa_\tau$ are fixed to the SM, the combined observed constraint is $-0.4 < \kappa_\lambda < 6.3$ $(-1.9 < \kappa_\lambda < 7.6)$, with a best-fit value of $\kappa_\lambda = 3.0$. An alternative model in which these coupling modifiers are instead allowed to float results in a similar constraint.

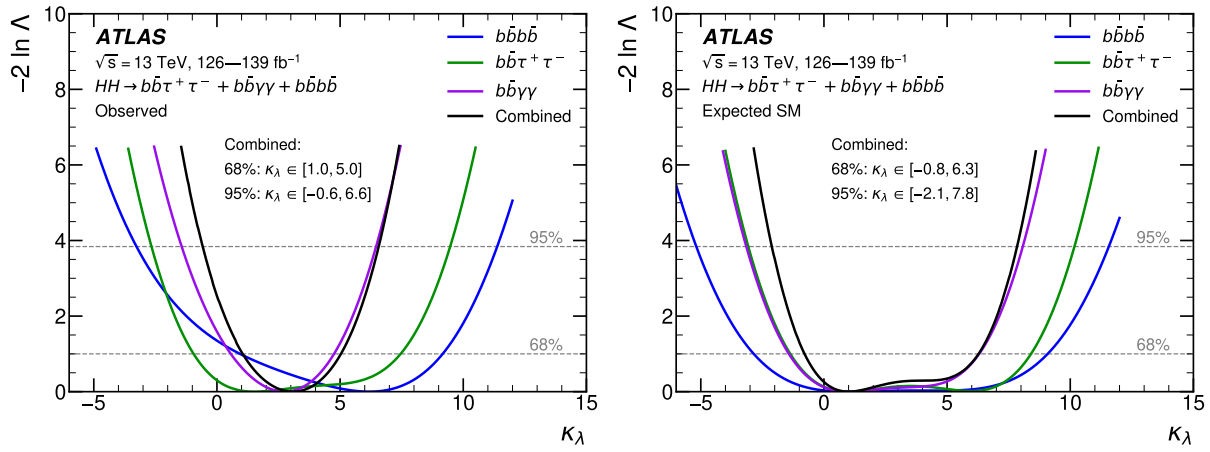

(a) (b)

Figure 10.14: The (a) observed and (b) expected likelihood curves as a function of κ_λ from the individual $b\bar{b}b\bar{b}$, $b\bar{b}\tau^+\tau^-$, and $b\bar{b}\gamma\gamma$ channels and their combination. The expected results assume SM HH production.

Channel	Integrated luminosity [fb^{-1}]
$HH \to b\bar{b}\gamma\gamma$	139
$HH \to b\bar{b}\tau^+\tau^-$	139
$HH \to b\bar{b}b\bar{b}$	126
$H \to \gamma\gamma$	139
$H \to Z^+Z^- \to 4l$	139
$H \to \tau^+\tau^-$	139
$H \to W^+W^- \to e\nu\mu\nu$ (ggF, VBF)	139
$H \to b\bar{b}$ (VH)	139
$H \to b\bar{b}$ (VBF)	126
$H \to b\bar{b}$ ($t\bar{t}H$)	139

Table 10.6: The list of input channels and their integrated luminosity used in the Run 2 ATLAS single-Higgs plus double-Higgs combination.

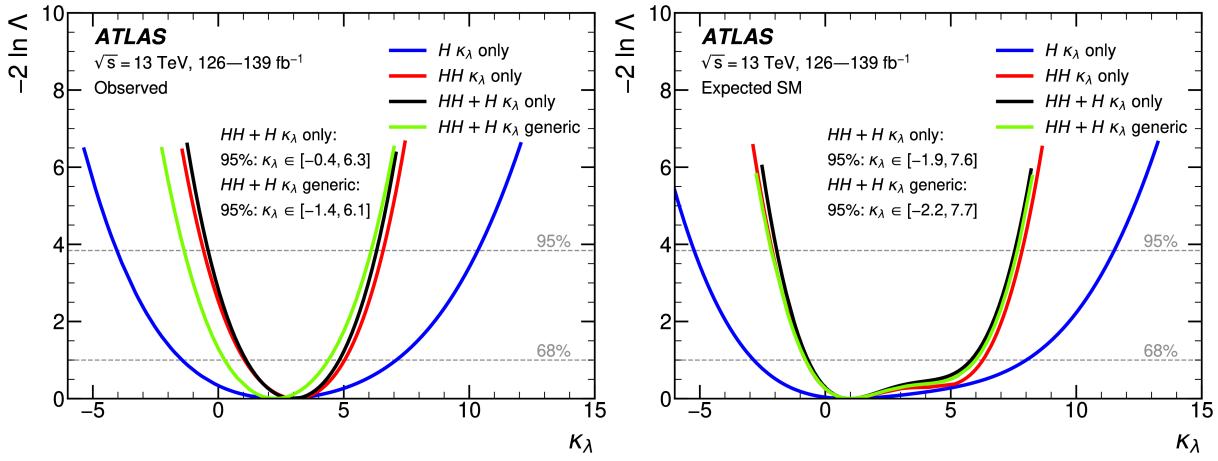

(a) (b)

Figure 10.15: The (a) observed and (b) expected likelihood curves as a function of κ_λ for the combination of double-Higgs and single-Higgs analyses. In the $HH + H$ κ_λ only model, the coupling modifiers $\kappa_t, \kappa_b, \kappa_V, \kappa_\tau$ are fixed to their SM values; in the $HH + H$ κ_λ generic model, they are instead allowed to float freely.

10.7 HL-LHC projections

While no significant HH signal was observed, it is yet unclear whether this is due to new physics or simply because of the miniscule SM HH cross-section. Under the latter assumption, projection studies have been performed extrapolating the sensitivity of the present $b\bar{b}\gamma\gamma$ analysis to a luminosity of 3000 fb^{-1} and $\sqrt{s}$ = 14 TeV, mimicking the the conditions expected at the High Luminosity LHC [55]. In the $b\bar{b}\gamma\gamma$ channel alone, it is projected that ATLAS will be able to achieve a signal significance of over $2\ \sigma$ for the SM HH signal and measure κ_λ to $[0.3, 1.9]$ at $1\ \sigma$. One key assumption in the projection is that at the HL-LHC, improvements in object reconstruction will cancel out with the degradation in environmental conditions, resulting in an object reconstruction efficiency effectively identical to that of Run 2. Furthermore, in the Baseline HL-LHC scenario, it is expected that many experimental and theoretical systematic uncertainties will be reduced by up to a factor of 50% [56]. Figure 10.16 shows the projected negative log-likelihood ratio as a function of κ_λ for a variety of HL-LHC scenarios.

The $b\bar{b}\gamma\gamma$ channel will remain one of the most competitive HH decay channels for the foreseeable future. A projected combination with the $HH \to b\bar{b}\tau^+\tau^-$ and $HH \to b\bar{b}b\bar{b}$ with 3000 fb^{-1} predicts a significance of $3.4\ \sigma$ [57] for SM HH production. With the inclusion of additional HH decay channels, further improvements in analysis strategy and object reconstruction, and a potential ATLAS-CMS combination, it may be possible to obtain a $5\ \sigma$ observation of HH production at the HL-LHC.

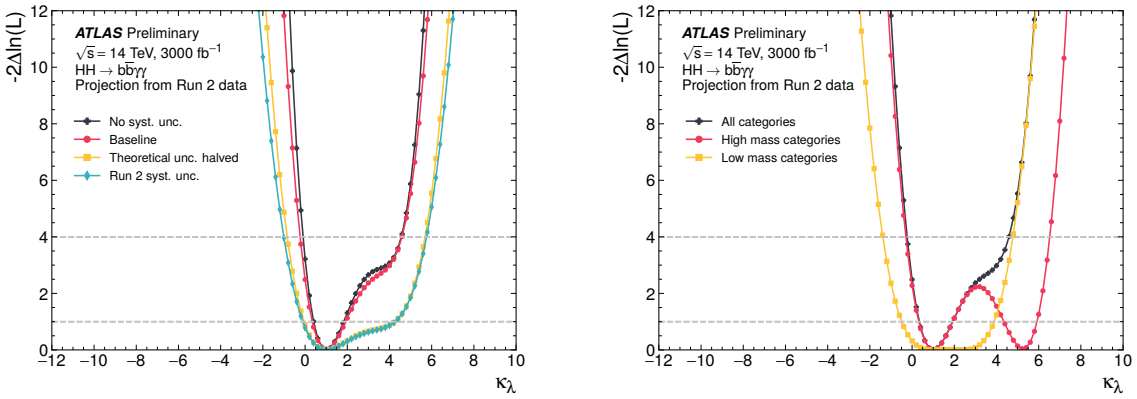

Figure 10.16: The negative log-likelihood ratios as a function of κ_λ, obtained by projecting the Run 2 $b\bar{b}\gamma\gamma$ analysis to the conditions of the HL-LHC. In (a), results for four different systematic uncertainty scenarios are shown. The Baseline scenario assumes that systematic uncertainties are reduced following the prescription described in Section 10.7; the $1\ \sigma$ constraint on κ_λ is $[0.3, 1.9]$. The Theoretical unc. halved scenario assumes that only theoretical systematic uncertainties are halved while experimental systematic uncertainties are unchanged from their Run 2 values. The Run 2 syst. unc. scenario assumes that all systematic uncertainties remain unchanged from their Run 2 values. The degradation in sensitivity in this scenario is due to the projected scaling of the spurious signal systematic which may be overly pessimistic. In (b), the Baseline scenario curve is split into contributions defined by the two **High Mass** and two **Low Mass** regions as defined in Table 10.2. The product of cross-section and selection efficiency results in degeneracies at different values of κ_λ for the **Low Mass** and **High Mass** categories, so that the degeneracy is resolved in the combined curve. The expected results are obtained from an Asimov data set generated under the SM hypothesis. The dashed horizontal lines indicate the values of the negative log-likelihood ratio corresponding to the $1\ \sigma$ and $2\ \sigma$ confidence levels. It is assumed that all couplings except κ_λ are equal to their SM values.

Chapter 11

The ITk upgrade

The high luminosity LHC (HL-LHC) is planned to begin operating around 2028. Featuring a planned instantaneous luminosity five times that of Run 2 and and a total integrated luminosity of up to 3000 fb^{-1}, it will bring sensitivity to rare processes such as Higgs pair production which are currently inaccessible. At the same time, the ATLAS detector will need to also be upgraded due to the harsh conditions resulting from such a drastic increase in luminosity, such as increased pileup and radiation damage.

A critical component under consideration is the inner detector, which will be completely replaced with a new inner tracker (ITk) [58]. The ITk project is arguably the most important upgrade to the whole ATLAS detector. As the closest component to the beamline, it is responsible for tracking, and by extension, b-tagging. At the same time, this proximity means that it is affected the most by hazards such as radiation damage.

SLAC national accelerator laboratory is the designated site for integrating the inner system, which consists of the two innermost layers of the ITk. At SLAC, pixel modules consisting of a readout chip and a silicon sensor will be glued onto local mechanical supports, and then connected with data and power services for eventual delivery to CERN. As a test run prior to production of the actual detector components, SLAC aims to complete a portion of the inner system with prototype materials in order to demonstrate the feasibility of the loading plan and the inner system design. This prototype project aims to provide crucial feedback concerning the many new challenging design aspects of the ITk detector, such as the large serial power chains, simultaneous readout of large numbers of channels, and thermal-mechanical compliance.

11.1 ITk layout

Figure 11.1 shows a schematic of one quadrant of the planned ITk layout [59], consisting of a series of nested barrel and ring layers, indexed from inside to out by increasing r. The inner system is defined as the innermost two layers of the ITk. In the inner system, the rings for layers 0 and 1 are coupled together at low z, and there are also rings in between the two layers (layer 0.5) at high z.

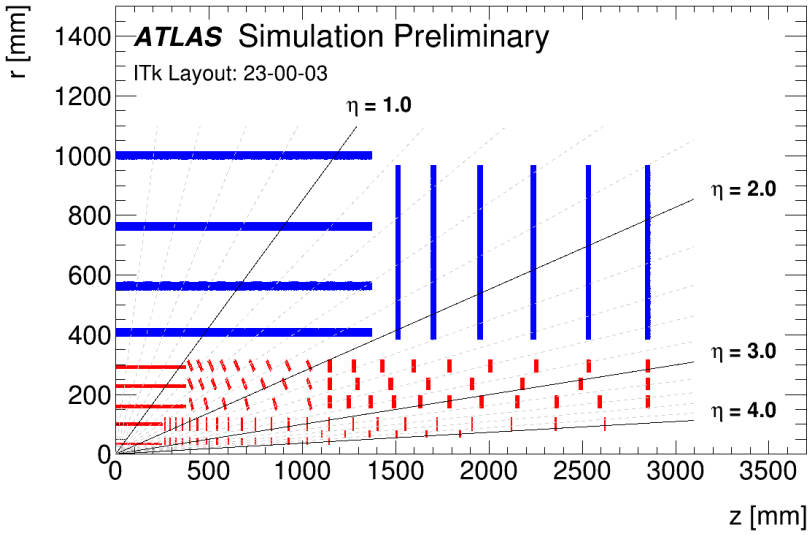

Figure 11.1: Schematic of one quadrant of the planned ITk layout. The blue (red) areas indicate silicon strip (pixel) sensor technologies. The inner system consists of the innermost two layers. Coupled rings are present in the inner system at low z.

11.2 Pixel modules

A pixel module consists of a silicon sensor bump bonded to a readout chip. Charged particles traversing the sensor ionize the silicon bulk, depositing charges which are then collected, digitized, and output by the readout chip for further processing. As of late 2022, there are two main designs of readout chip for the ATLAS ITk. The RD53A design [60] is a prototype pre-production chip, with relatively widespread availability but known peculiarities, while the ITkPixV1 chip [61] is considered to be more stable and closer to the final design specification, but is quite new with limited accessibility. The sensitive area of an ATLAS RD53A chip consists of a matrix of 192 $\times$

400 pixels of 50 μm $\times$ 50 μm, divided into three regions: synchronous, linear, and differential, named after their front end circuit designs. In contrast, the ATLAS ITkPixV1 chip will have twice the number of pixels at 384 $\times$ 400 pixels, all running the differential front end circuit.

For both the RD53A and ITkPixV1 designs, there are multiple types of module architectures depending on their intended use and position in the detector. The single chip card (SCC) consists of a single front end chip and is used for debugging purposes only due to its self contained nature and ease of use. Triplet modules containing three chips, will be present in the L0 stave and L0 and L0.5 rings, while quad modules containing four chips are designed for the remainder of the ITk pixel system [59]. In addition, triplet modules are attached to 3D sensors while quad modules are attached to planar sensors. The RD53A design will be assumed in the remainder of this section.

11.3 Electrical prototype

One major goal of the electrical prototype at SLAC is to assemble and test the coupled R0/1 ring and L1 staves. As many components such as modules and the local supports are not manufactured at SLAC, it is first important to check the quality of these components upon arrival. The electrical performance of the modules are characterized by standardized reception tests which are performed both by the sending institution and at SLAC. Once modules have passed the reception test, they are then loaded onto local supports. Modules are tested again after loading with the same tests in order to check for potential defects due to the loading process. After that, additional tests aim to characterize the performance of the additional service components used for data transmission, power, and monitoring on the loaded local supports.

11.4 Module reception test

Upon arrival at SLAC, all modules first undergo a series of reception tests. It is then possible to determine whether any future observed problems are due to the shipping process or from the loading and handling process at SLAC. The reception tests consist of three parts: visual inspection, sensor IV scans, and basic electrical tests. For each of these, any potential anomalies are noted and compared to results from the sending institution.

Figure 11.2 shows the reception stand used for the sensor IV scans and the electrical tests. Data is passed through the flexes, an adapter, and through a commercial DisplayPort cable to the readout computer. Two power supplies are present; one low voltage to power the front end, and one high voltage to reverse-bias the sensor. For RD53A, a front end module typically draws a current of 1.15A per chip, and a voltage of around 2V. The sensors are typically operated at a bias voltage of around 50V. In this reception setup, the module is supported underneath by a thermal pad and fan in order to prevent overheating, and the temperature and voltage consumed by the module are monitored using sense wires connected to a Raspberry Pi.

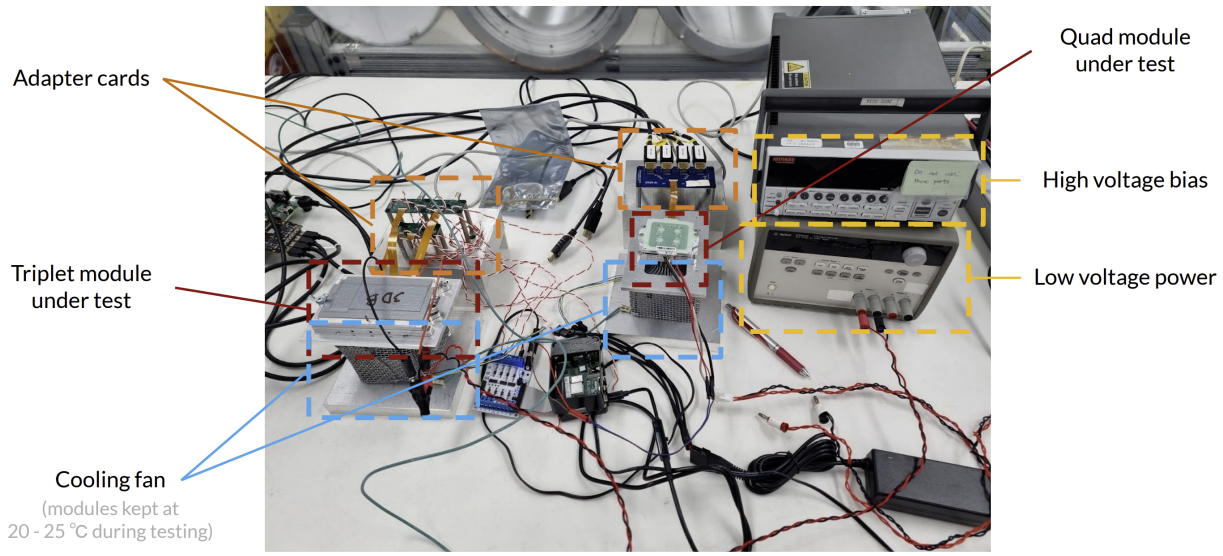

Figure 11.2: The reception stand used to perform electrical tests on the modules after the visual inspection. The image shows a triplet (‘3DB’) on the left and a quad module on the right, both of which are covered by a carrier to prevent accidental damage. The modules are situated on top of fans to prevent overheating. Data is output to the test machine via the brown flexes connected to the green and blue adapter cards in the background. The low voltage (bottom) and high voltage (top) power supplies can be seen stacked on the right. A Raspberry Pi monitors the temperature and voltage consumed.

11.4.1 Visual inspection

In this first step, the module is inspected for obvious visible physical defects, done by eye with an optical microscope. Particular focus is given to the wirebond connections, which are

especially delicate. The condition of the packaging, as well as the data recorded by shock and humidity sensors, is also noted. The visual inspection process aims to give only a quick survey of the module quality before proceeding with the more detailed and informative electrical tests. Figure 11.3 shows microscope images of a quad and triplet module. For the visual inspection, the top of the protective module carrier is removed.

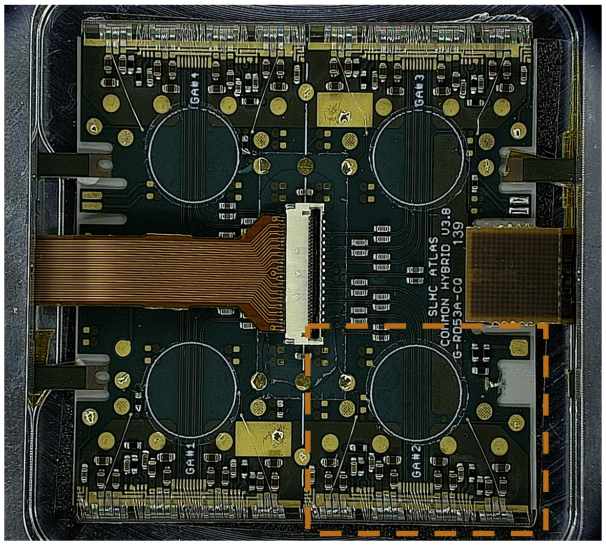

(a)

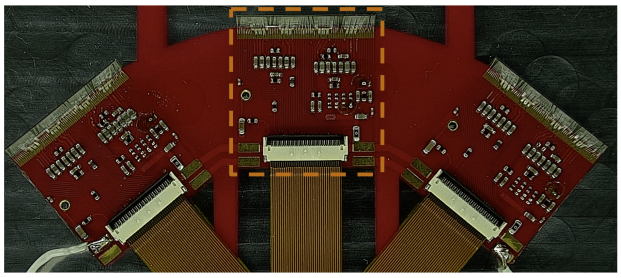

(b)

Figure 11.3: An overview image of (a) a quad module and (b) a triplet module taken by the SLAC visual inspection microscope. The area roughly corresponding to an individual chip is highlighted in orange. Wirebonds are visible on the top and bottom sides of the image. Data is transmitted through the brown flex passing to the left of the quad module and the three brown flexes at the bottom of the triplet.

11.4.2 Sensor IV scan

The performance of the silicon sensor is characterized by applying a range of bias voltages (V) and measuring the resulting leakage current (I). Increasing the bias voltage past a certain threshold will cause sensor breakdown, in which the leakage current increases rapidly with the current, and can lead to permanent damage to the sensor. The resulting IV curve is compared with that obtained from the sending institution, in order to ensure that the sensor characteristics have not changed, and that the nominal bias voltage working point does not exceed the breakdown threshold. Figure 11.4 shows an example of an IV curve for 3 chips from a given triplet module. The measured leakage current is sensitive to both temperature and the presence of light.

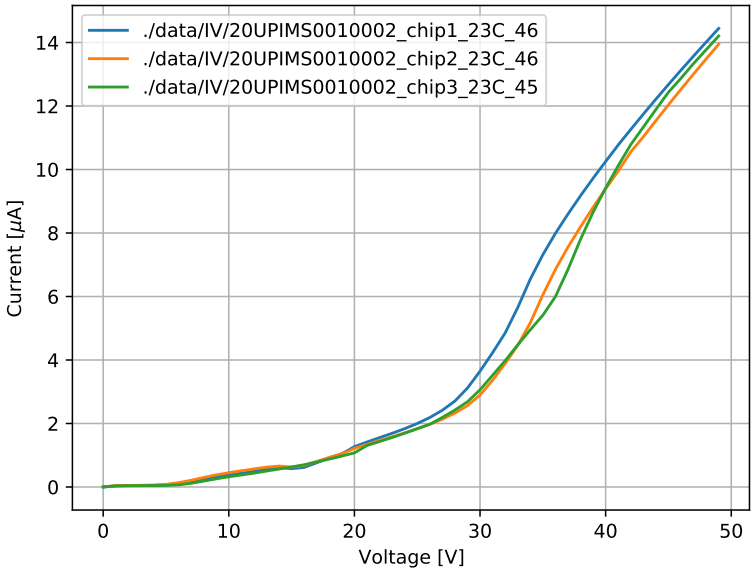

Figure 11.4: The sensor IV curve for each of the three chips from a triplet module measured at SLAC.

11.4.3 Basic electrical tests

Finally, the performance of the front end is tested. A series of basic electrical tests on the module is carried out with the YARR readout system [62].

The following scans are performed:

- Digital
- Analog
- Threshold
- Time over threshold
- Disconnected bump bond (cross-talk based)

The digital and analog scans test the basic responsiveness of the module, with the digital scan bypassing the analog front end circuit, by injecting a known pulse multiple times into each of the pixels, and checking the resulting number of hits in each pixel (the occupancy). The threshold scan tests the level of charge at which the pixels are triggered; in an ideal front end, all pixels should have a consistent threshold level with very little dispersion among different pixels. The time over threshold scan measures the amount of time for which a known, fixed injected charge exceeds the threshold value. Finally, of particular interest is the disconnected bump bond scan, which checks for the presence of any disconnected bump bonds between the sensor and the front end, and is therefore particularly sensitive to potential changes due to the mechanical action involved in the loading process. The disconnected bump bond test carried out at SLAC involves injecting charges into specific pixels and looking for the presence of cross-talk in neighbouring pixels. A lack of cross-talk indicates that one or more bump bonds have failed. While this scan avoids any need for a radioactive source and associated safety requirements, one downside is that it can only detect general areas of failure and not the specific pixels which have failed.

Electrical scan results for each module are backed up to a localdb database [63], for future integration with the global ITk production database [64]. In this way, it will be possible to track the history of the individual module components and their performance results.

11.4.4 Reception results

Common observed issues with the modules received at SLAC include broken front-end chips, early sensor breakdown, data transmission problems, noisy front-ends, or areas of disconnected bumps. However, due to their prototype status, the most important check is not their absolute quality but whether the results are consistent with those obtained from the sender. That said, the

quality of the modules is still valuable for purposes of evaluating the loading procedure at SLAC - for example, a module with only two out of four working chips would not nearly give as much useful data as a fully working module. As of November 2022, a total of 23 quad modules and 6 triplets have been reception tested at SLAC. Of these, 10 quad modules and 3 triplets have been loaded onto the L0/1 coupled ring. The L1 stave has been half-loaded with 6 quad modules.

11.5 Post-loading electrical tests

Figure 11.5 shows a fully-loaded L0/1 coupled ring (10 quads and 3 triplets) as well as a half-loaded L1 stave (6 quads). Following loading, the electrical tests in Section 11.4.3 are repeated for each individual module and the results are compared with the pre-loading results in order to check for anomalies. As the loading procedure involves removing the modules from their protective carriers, leaving their wirebonds permanently exposed, special additional mounts are designed in order to adapt the reception test setup for these post-loading tests. Of particular note is the difference in cooling system - while the module in reception was cooled from below through thermal contact with the carrier and a fan, the module in post-loading is now cooled by a fan held some distance above the module, leading to a slightly warmer temperature.

In general, it was found that for the 19 loaded modules, there were no large differences on the electrical scan results between reception and post-loading, and it was concluded that the loading procedure was safe. Certain modules showed small discrepancies in the threshold values, which is currently hypothesized to be due to the aforementioned temperature differences. Furthermore, due to the inherent risk in working with such exposed modules, it is unlikely that these post-loading tests will be needed for final production.

11.6 Data, power, and monitoring services

The treatment of data, powering, and monitoring services on the reception test stand is different from that in the final detector, and must therefore be accounted for at this stage.

On the reception test stand, modules are connected to data and monitoring services via a special adapter card, a setup which is obviously not feasible for the final detector layout. For the modules loaded onto the coupled ring, the data and monitoring information from all the modules will be

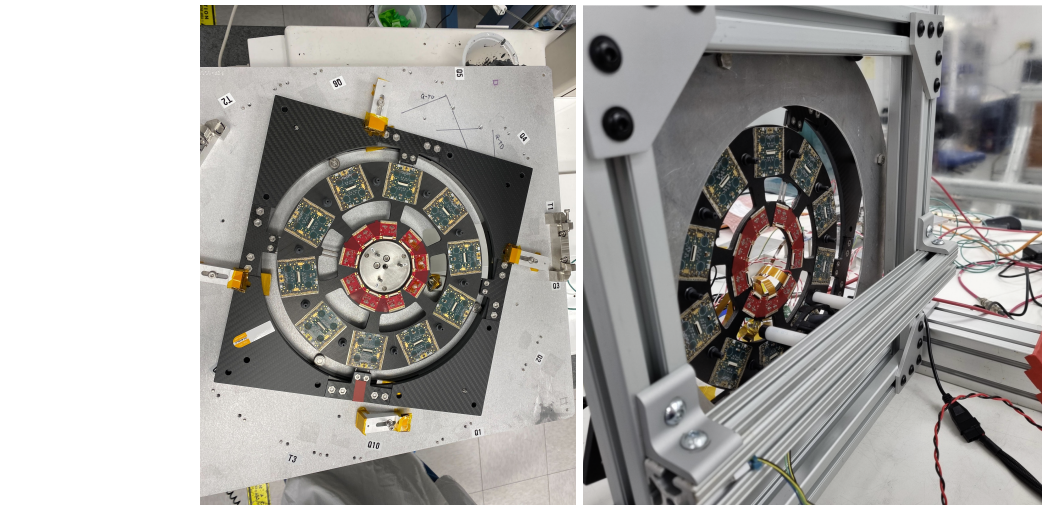

(a) (b)

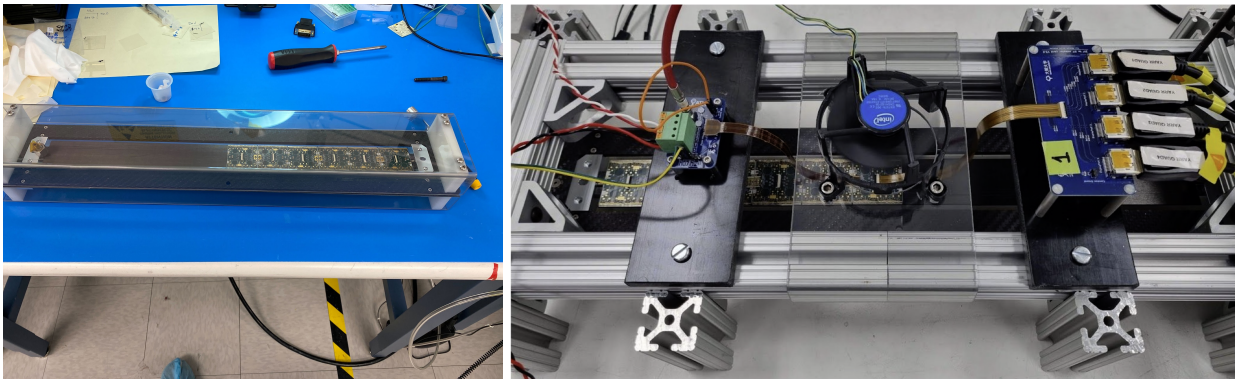

(c) (d)

Figure 11.5: (a) A fully loaded L0/1 coupled ring and (b) the custom test stand for post-loading tests. (c) The half-loaded L1 stave and (d) its corresponding test stand.

collected en-masse by an additional type-0 ring, which in turn interfaces with a patch panel (pp0), after which the signal will interface with DisplayPort (DP) cables for the pre-production testing setup.

Similar concerns exist for module powering. While the modules on the reception stand are individually powered, the modules on the detector will require the use of serial powering chains, in which groups of modules are powered in series, in order to save material on cabling. The coupled ring has two serial powering chains: one for the 10 quad modules, and one for the 3 triplet modules.

It is important to validate that in this serial powering chain setup, each module will self-regulate and draw only the allotted amount of voltage.

Figure 11.6 shows a schematic of the type-0 ring, with 9 connectors for the 3 triplet modules and 10 connectors for the 10 quad modules, labelled as T1 - T9 and Q1 - Q10, respectively.

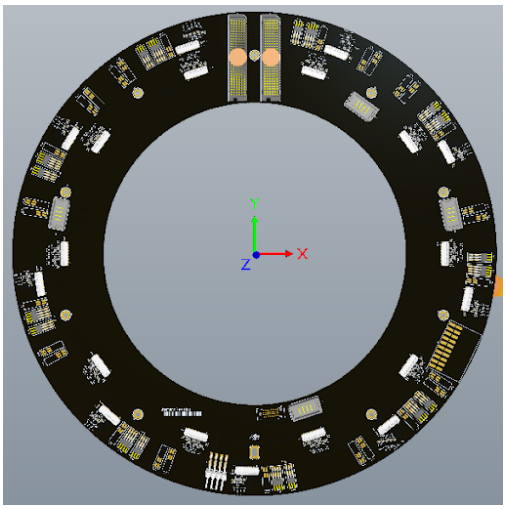

Figure 11.6: A schematic of the type-0 ring. 9 white ZIF connectors on the edge of the ring and 10 white ZIF connectors in the middle of the ring transfer data for the 3 triplet modules and 10 quad modules, respectively. In this thesis, they are referred clockwise from the top as T1 - T9 and Q1- Q10, respectively. The data is passed to the two rectangular LPAM connectors at the top, and through two special flexes to arrive at the pp0 (not shown). The right LPAM services Q1 - Q5 and T1 - T3, while the left LPAM covers Q6 - Q10 and T4 - T9.

11.6.1 Data transmission tests

The trigger rate of the new ITk Pixel detector is expected to be ten times higher than that of the current ATLAS detector. Each front end chip will contain one command lane operating at a bit rate of 160 Mbps and four output data lanes at a rate of 1.28 Gbps [58]. The total signal loss, from the front end chip to the receiving optical converter step of the detector, is required to be at worst -20 decibels (dB)[1] according to official design specifications [58]. A network analyzer is used to measure the signal loss as function of signal frequency; a frequency of 640 MHz is chosen to correspond with the nominal bit rate of 1.28 Gbps.

[1] A -10 dB corresponds to a 10 times reduction in the power.

Table 11.1 shows preliminary loss numbers in dB measured including the module flex, type-0 ring, ring to pp0 flex, and pp0 components. Unfortunately, a slight defect in the design of the ring to pp0 flex resulted in open connections for certain positions, leading to uncharacteristically high loss values. This is expected to be solved in the next design iteration of the connector. However, in general, the losses increase with the physical distance the signal is required to travel, with the largest distances corresponding to positions Q5 and Q6. For the unbroken connections, the average loss values of 4 - 6 dB, plus an anticipated 11 dB from additional cabling, results in a total loss that is within the required 20 dB budget. A similar test was conducted for the triplet positions, with similar conclusions.

Signal loss measurements for quad positions on the type-0 ring [-dB]										
Lane	Q1	Q2	Q3	Q4	Q5	Q6	Q7	Q8	Q9	Q10
DATA 0	3.4	4.2	5.4	4.5	28.5	13.4	3.8	5.2	3.2	-
DATA 1	5.3	12.2	5.5	23.8	13.2	6	4.9	3.7	3.7	-
DATA 2	4.1	4.8	5.3	5.1	> 40	8.2	4	3.7	3.6	-
DATA 3	3.8	4.8	5.2	29	5.6	5.4	6.2	3.9	3.7	-
CMD	4.5	5.2	15.4	12.1	16.1	13.9	4.5	4.3	4.7	-

Table 11.1: A measurement of data losses for a signal frequency of 640 MHz for various positions on the type-0 ring. Highlighted outlier values are speculated to be due to open connections in the flex connecting the type-0 ring with the pp0, which will be solved by using a new connector design. For the remaining connections, the average loss values of 4 - 6 dB, plus an anticipated 11 dB from additional cabling, results in a total loss that is within the required 20 dB budget. Due to the prototype nature of the ring, the Q10 position was inaccessible for testing.

In addition to the signal loss measurements, the data transmission quality is alternatively quantized through a bit error rate (BER) test. For a data transfer rate of 1.28 Gbps, the unit interval (UI), the time for one bit to be transferred, is approximately 780 ps. Due to the periodic nature of the output data stream, it is possible to add a time delay of up to one UI before sampling the signal. Thus by running multiple digital scans at various points in a UI, it is possible to test the fraction of

the UI robust to data transmission errors. In particular, points near the transition point between bit changes are generally unstable due to random bit flips caused by signal jitter.

In practice, as a balance between precision and resource consumption, a point in the UI is defined to pass only after 20 successful digital scans without errors, roughly corresponding to a bit error rate of 10^{-10}. In order to perform the digital scans at a rate of 1.28 Gbps, a readout system based on the SLAC RCE platform [65] was used instead of YARR, which at the time of testing only supporting speeds of up to 640 Mbps. In general, the signal loss decreases quickly with readout frequency; thus it is imperative to use the full expected transmission rate in order to detect the presence of possible data transmission issues. In addition, the BER tests provides important information complementary to the signal loss measurements as it directly evaluates the performance of the modules.

Table 11.2 shows the obtained widths for a fixed triplet module on various positions on the type-0 ring, showing relatively consistent performance.

Triplet position	Width at BER 10^{-10} [ps]
T4	207
T5	179
T6	207
T7	172
T8	217

Table 11.2: The bathtub widths corresponding to a bit error rate of 10^{-10} obtained from repeated digital scans for a fixed triplet module connected to various positions on the type-0 ring. The maximum possible width is approximately 780 ps. The measurement includes the type-0 ring, ring to pp0 flex, pp0, and an additional 0.5 m DP cable.

Finally, the flexes and cables were also scrutinized for potential data transmission problems. Due to the commercial nature of the DisplayPort cables, a selection of different cable brands were compared in order to determine the one with the best data transmission performance. Different cables from the same brand were also tested to ensure consistent performance. A similar procedure

was carried out for the data flexes which were custom made for the inner system, but did undergo several revisions.

11.6.2 Power and monitoring services

The type-0 ring provides not only data but also power and monitoring services to the quad and triplet modules. Real-time services for monitoring the voltage draw and temperatures of the modules are required both for debugging purposes as well as for monitoring once the detector is fully assembled. These systems will eventually be connected to an interlock to immediately shut down the module upon detecting any problems.

Figure 11.7 shows the front and back sides of the coupled ring once power and monitoring services have been attached. Note that the specific layout is subject to change with further iterations of the design; in particular, the additional 3D-printed ring on the backside is simply a temporary mechanical support and not expected to be used for the final detector.

11.6.3 Performance inside the QC box

Once the services have been attached, the modules can no longer be individually powered and therefore cannot be individually tested with the reception setup due to heating issues. Consequently, the ring is inserted into a special climate-controlled QC (Quality Control) box to control the temperature and humidity of the environment, shown in Figure 11.8.

Inside the QC box, the functionality of the monitoring services was validated as the temperatures and voltages of each module were successfully read out. The serial powering chain was also validated with each module drawing its expected voltage without any complications. Finally, electrical scans on the modules were conducted. While some module positions were not testable due to known damage in the LPAM connector, the results for the remaining modules were consistent with those obtained upon reception at SLAC. Figure 11.9 shows the result of a disconnected bump bond scan on a module before it is loaded and inside the QC box. While a large area of disconnected bump bonds is observed near the right edge of the module, its size is consistent between the two results and therefore does not indicate any damage due to the loading process.

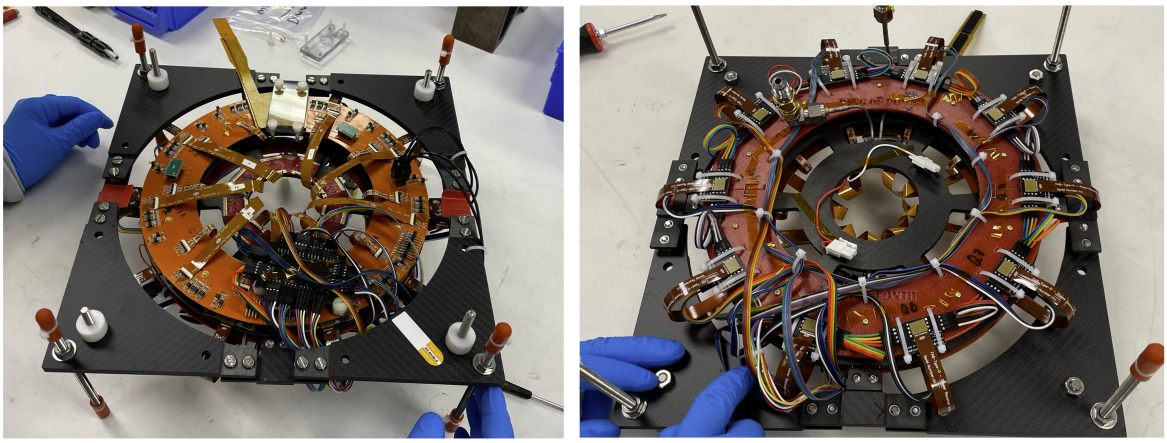

(a) (b)

Figure 11.7: (a) The type-0 ring mounted on top of the loaded ring. On this top face, the brown flex connectors route data from the triplet and quad modules to the type-0 ring and monitoring for the triplets. The large rectangular card collects information from monitoring services for the triplets and quads, and also distributes power for the quads. Serial powering for the triplets is achieved by simply soldering adjacent power connectors together. For the purposes of the electrical prototype only, an additional 3D-printed ring (b) is also attached to the back of the loaded ring in order to hold additional connectors required for powering and monitoring. On this bottom face, the brown flex connectors provide power to the quads. The small rectangular black cards constitute the quad serial powering and send monitoring information. Triplet power is provided through the red and white 4-pin power connectors.

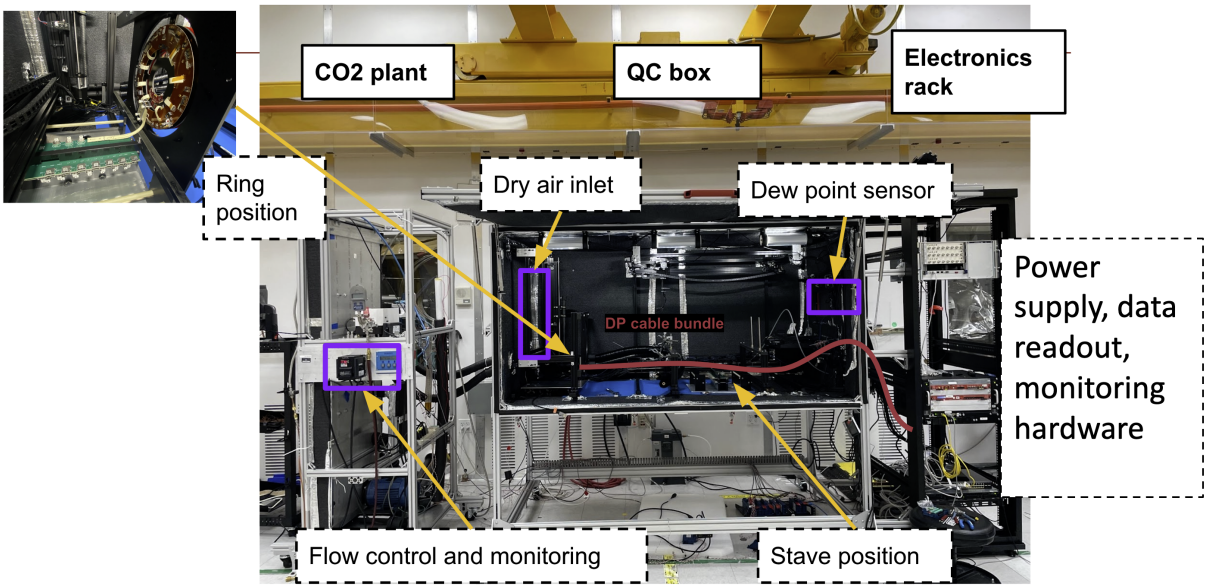

Figure 11.8: The environmentally-controlled box for holding the loaded ring and eventually the stave. Data, power, and monitoring services are output through a long bundle of cables to the electronics rack on the right.

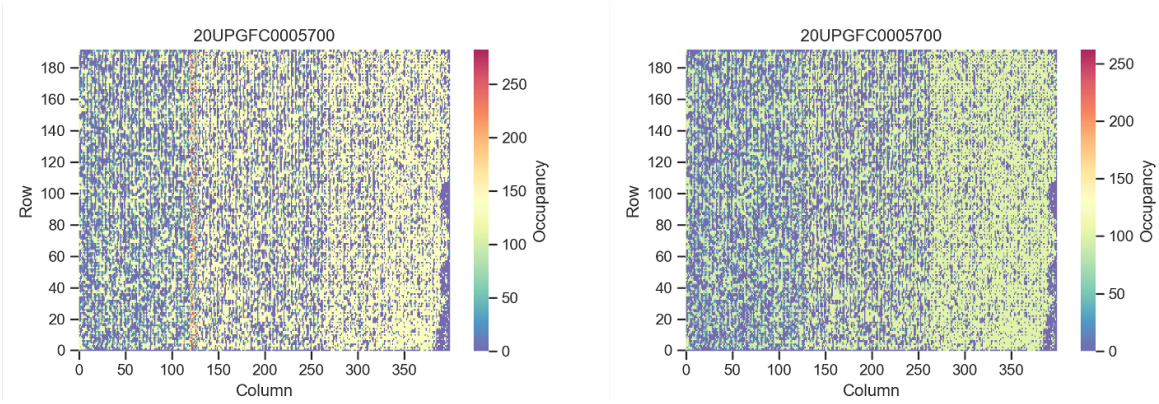

(a) (b)

Figure 11.9: Disconnected bump bond scan for the same quad module (a) upon reception at SLAC and (b) inside the QC box at a temperature of -5° C. While a small area of disconnected bump bonds (indicated by low occupancy pixels) is observed near the right edge of the module, its size is consistent between the two results and therefore does not indicate any damage due to the loading process.

Chapter 12

Conclusion

Despite its low branching ratio, the $H \to \gamma\gamma$ decay channel remains one of the best channels to probe Higgs couplings due to the excellent ATLAS photon resolution and clean signature of two high p_{T} photons. With 79.8 fb^{-1} of 13 TeV data, the $t\bar{t}H$ ($H \to \gamma\gamma$) channel was vital to the observation of $t\bar{t}H$ production in the ATLAS combination, alone contributing an observed (expected) significance of 4.1 σ (3.7 σ). Since then, the $t\bar{t}H$ ($H \to \gamma\gamma$) analysis has been updated several times in Run 2. In 2019, the $t\bar{t}H$ ($H \to \gamma\gamma$) analysis was updated to use 139 fb^{-1} of data collected from 2015 to 2018 [66]. The analysis categorization was unchanged from the 79.8 fb^{-1} analysis, and the resulting single channel significance of 4.9 σ (4.2 σ expected) reinforced the importance of this channel in probing $t\bar{t}H$ properties. A 2020 measurement of the CP properties of the Higgs-top coupling also used the same analysis selection in conjunction with additional selections in order to measure the CP properties of the Higgs-top Yukawa coupling [13]. Finally, in 2022, a simultaneous measurement of all Higgs production modes in the $H \to \gamma\gamma$ channel [67] included a reoptimization of the strategy for measuring $t\bar{t}H$. In this coupling analysis, the sensitivity of the $H \to \gamma\gamma$ channel allowed for one of the first measurements of $t\bar{t}H$ production in bins of the Higgs p_{T}, which provides additional sensitivity to κ_λ compared to inclusive production [68]. The coupling results were also included in a combination of all Higgs properties celebrating the tenth anniversary of the Higgs discovery [69].

The Run 2 $HH \to b\bar{b}\gamma\gamma$ analysis likewise exploited features of the $H \to \gamma\gamma$ decay in order to search for Higgs pair production in 139 fb^{-1} of 13 TeV data. No significant excess was observed, and the observed (expected) 95% CL limit on the HH signal strength was found to be 4.2 (5.7). A scan of the limit as a function of κ_λ resulted in an observed (expected) constraint on κ_λ of [-1.5, 6.7] ([-2.4, 7.7]). The results in the $b\bar{b}\gamma\gamma$ channel are extremely competitive with the $HH \to b\bar{b}\tau^+\tau^-$

and $HH \rightarrow b\bar{b}b\bar{b}$ channels, which used a similar dataset to observe signal strength limits of 4.7 and 5.4, respectively, for a total combined limit of 2.4 with all 3 channels [54]. While no signal was discovered in Run 2, projection studies indicate that the prospects of a discovery in the far future of the HL-LHC are optimistic. In the near future, developments in this channel may aim to additionally constrain the κ_{2V} modifier through the VBF HH production mode, which is currently included in the analysis as a signal but otherwise not targeted for optimization.

Finally, the importance of the ITk upgrade to the future performance of the ATLAS detector in the HL-LHC should not be understated. As the innermost part of the detector, it is critical for tracking and b-tagging, the latter of which is vital for the main HH channels which all rely on the $H \rightarrow b\bar{b}$ decay. At SLAC, the process of building the module reception stands, carrying out data transmission tests, and evaluating the functionality of the services yielded many interesting lessons regarding all the various aspects of the inner system. These include not only electrical but also subtle mechanical problems which can be difficult to spot without the act of physically assembling the prototypes. So far, all tests show that the loading procedure at SLAC does not degrade the electrical performance of the module. Future planned ITk activities at SLAC may include repeating the established tests for the L1 stave in the QC box, developing the simultaneous readout of multiple modules, and eventually completing an integrated quarter shell consisting of a coupled ring and stave.

LIST OF REFERENCES

[1] F. Englert and R. Brout, "Broken Symmetry and the Mass of Gauge Vector Mesons", *Phys. Rev. Lett.* **13** (1964) 321, doi:10.1103/PhysRevLett.13.321.

[2] P. W. Higgs, "Broken symmetries, massless particles and gauge fields", *Phys. Lett.* **12** (1964) 132, doi:10.1016/0031-9163(64)91136-9.

[3] P. W. Higgs, "Broken Symmetries and the Masses of Gauge Bosons", *Phys. Rev. Lett.* **13** (1964) 508, doi:10.1103/PhysRevLett.13.508.

[4] G. S. Guralnik, C. R. Hagen, and T. W. B. Kibble, "Global Conservation Laws and Massless Particles", *Phys. Rev. Lett.* **13** (1964) 585, doi:10.1103/PhysRevLett.13.585.

[5] P. W. Higgs, "Spontaneous Symmetry Breakdown without Massless Bosons", *Phys. Rev.* **145** (1966) 1156, doi:10.1103/PhysRev.145.1156.

[6] T. W. B. Kibble, "Symmetry Breaking in Non-Abelian Gauge Theories", *Phys. Rev.* **155** (1967) 1554, doi:10.1103/PhysRev.155.1554.

[7] ATLAS Collaboration, "Observation of a new particle in the search for the Standard Model Higgs boson with the ATLAS detector at the LHC", *Phys. Lett. B* **716** (2012) 1–29, doi:10.1016/j.physletb.2012.08.020.

[8] CMS Collaboration, "Observation of a new boson at a mass of 125 GeV with the CMS experiment at the LHC", *Phys. Lett. B* **716** (2012) 30–61, doi:10.1016/j.physletb.2012.08.021, arXiv:1207.7235.

[9] ATLAS Collaboration, "Study of the spin and parity of the Higgs boson in diboson decays with the ATLAS detector", *Eur. Phys. J. C* **75** (2015) 476, doi:10.1140/epjc/s10052-015-3685-1.

[10] CMS Collaboration, "Constraints on the spin-parity and anomalous HVV couplings of the Higgs boson in proton collisions at 7 and 8 TeV", *Phys. Rev. D* **92** (2015) 012004, doi:10.1103/PhysRevD.92.012004.

[11] LHC Higgs Cross Section Working Group, "Handbook of LHC Higgs Cross Sections: 4. Deciphering the Nature of the Higgs Sector", *CERN Yellow Reports: Monographs* **2** (2017) doi:10.23731/CYRM-2017-002.

[12] ATLAS and CMS Collaborations, "Combined Measurement of the Higgs Boson Mass in pp Collisions at $\sqrt{s} = 7$ and 8 TeV with the ATLAS and CMS Experiments", *Phys. Rev. Lett.* **114** (2015) 191803, doi:10.1103/PhysRevLett.114.191803.

[13] ATLAS Collaboration Collaboration, "CP Properties of Higgs Boson Interactions with Top Quarks in the $t\bar{t}H$ and tH Processes Using $H \to \gamma\gamma$ with the ATLAS Detector", *Phys. Rev. Lett.* **125** (2020) 061802, doi:10.1103/PhysRevLett.125.061802.

[14] M. Grazzini et al., "Higgs boson pair production at NNLO with top quark mass effects", *JHEP* **5** (2018) 059, doi:10.1007/jhep05(2018)059.

[15] B. D. Micco, M. Gouzevitch, J. Mazzitelli, and C. Vernieri, "Higgs boson potential at colliders: Status and perspectives", *Reviews in Physics* **5** (2020) 100045, doi:10.1016/j.revip.2020.100045.

[16] P. Agrawal et al., "Determining the shape of the Higgs potential at future colliders", *Phys. Rev. D* **101** (2020) 75023, doi:10.1103/physrevd.101.075023.

[17] ATLAS Collaboration, "Constraints on the Higgs boson self-coupling from the combination of single-Higgs and double-Higgs production analyses performed with the ATLAS experiment", *ATLAS-CONF-2019-049* (2019). https://cds.cern.ch/record/2693958.

[18] G. Degrassi, P. Giardino, F. Maltoni, and D. Pagani, "Probing the Higgs self coupling via single Higgs production at the LHC", *JHEP* **12** (2016) 080, doi:10.1007/jhep12(2016)080.

[19] F. Maltoni, D. Pagani, A. Shivaji, and X. Zhao, "Trilinear Higgs coupling determination via single-Higgs differential measurements at the LHC", *Eur. Phys. J. C* **77** (2017) 887, doi:10.1140/epjc/s10052-017-5410-8.

[20] ATLAS Collaboration, "The ATLAS Experiment at the CERN Large Hadron Collider", *JINST* **3** (2008) S08003, doi:10.1088/1748-0221/3/08/S08003.

[21] ATLAS Collaboration, "Performance of the ATLAS trigger system in 2015", *Eur. Phys. J. C* **77** (2017) 317, doi:10.1140/epjc/s10052-017-4852-3.

[22] ATLAS Collaboration, "Performance of electron and photon triggers in ATLAS during LHC Run 2", *Eur. Phys. J. C* **80** (2020) 47, doi:10.1140/epjc/s10052-019-7500-2.

[23] ATLAS Collaboration, "Electron and photon performance measurements with the ATLAS detector using the 2015–2017 LHC proton–proton collision data", *JINST* **14** (2019) P12006, doi:10.1088/1748-0221/14/12/P12006.

[24] ATLAS Collaboration, "Measurement of Higgs boson production in the diphoton decay channel in pp collisions at center-of-mass energies of 7 and 8 TeV with the ATLAS detector", *Phys. Rev. D* **90** (2014) 112015, doi:10.1103/PhysRevD.90.112015.

[25] ATLAS Collaboration, "Muon reconstruction and identification efficiency in ATLAS using the full Run 2 pp collision data set at $\sqrt{s} = 13$ TeV", *Eur. Phys. J., C* **81** (2021) 578, doi:10.1140/epjc/s10052-021-09233-2.

[26] ATLAS Collaboration, "Topological cell clustering in the ATLAS calorimeters and its performance in LHC Run 1", *Eur. Phys. J. C* **77** (2017), no. 7, 490, doi:10.1140/epjc/s10052-017-5004-5.

[27] M. Cacciari, G. P. Salam, and G. Soyez, "FastJet User Manual", *Eur. Phys. J. C* **72** (2012) 1896, doi:10.1140/epjc/s10052-012-1896-2.

[28] M. Cacciari, G. P. Salam, and G. Soyez, "The anti-k_t jet clustering algorithm", *JHEP* **04** (2008) 063, doi:10.1088/1126-6708/2008/04/063.

[29] ATLAS Collaboration, "Jet reconstruction and performance using particle flow with the ATLAS Detector", *Eur. Phys. J. C* **77** (2017) 466, doi:10.1140/epjc/s10052-017-5031-2.

[30] ATLAS Collaboration, "Performance of pile-up mitigation techniques for jets in pp collisions at $\sqrt{s}$ = 8 TeV using the ATLAS detector", *Eur. Phys. J. C* **76** (2016) 581, doi:10.1140/epjc/s10052-016-4395-z.

[31] ATLAS Collaboration, "Expected performance of the ATLAS b-tagging algorithms in Run-2", *ATL-PHYS-PUB-2015-022* (2015). https://cds.cern.ch/record/2037697.

[32] ATLAS Collaboration, "ATLAS b-jet identification performance and efficiency measurement with $t\bar{t}$ events in pp collisions at $\sqrt{s} = 13$ TeV", *Eur. Phys. J. C* **79** (2019) 970, doi:10.1140/epjc/s10052-019-7450-8.

[33] M. Oreglia, "A Study of the Reactions $\psi' \to \gamma\gamma\psi$",. https://www.slac.stanford.edu/cgi-wrap/getdoc/slac-r-236.pdf.

[34] ATLAS Collaboration, "Luminosity determination in pp collisions at $\sqrt{s} = 13$ TeV using the ATLAS detector at the LHC", *ATLAS-CONF-2019-021* (2019). https://cds.cern.ch/record/2677054.

[35] ATLAS Collaboration, "Jet energy scale and resolution measured in proton–proton collisions at $\sqrt{s} = 13$ TeV with the ATLAS detector", *Eur. Phys. J. C* **81** (2020) 689, doi:10.1140/epjc/s10052-021-09402-3.

[36] ATLAS Collaboration, "Measurement of inclusive and differential cross sections in the $H \to ZZ^* \to 4l$ decay channel in pp collisions at $\sqrt{s} = 13$ TeV with the ATLAS detector", *JHEP* **10** (2017) 132, doi:10.1007/jhep10(2017)132.

[37] ATLAS Collaboration, "Measurements of fiducial cross-sections for $t\bar{t}$ production with one or two additional b-jets in pp collisions at $\sqrt{s} = 8$ TeV using the ATLAS detector", *Eur. Phys. J. C* **76** (2016) doi:10.1140/epjc/s10052-015-3852-4.

[38] ATLAS Collaboration, "Measurement of differential production cross-sections for a Z boson in association with b-jets in 7 TeV proton-proton collisions with the ATLAS detector", *JHEP* **10** (2014) 141, doi:10.1007/jhep10(2014)141.

[39] ATLAS Collaboration, "Measurement of the cross-section for W boson production in association with b-jets in pp collisions at $\sqrt{s} = 7$ TeV with the ATLAS detector", *JHEP* **6** (2013) 084, doi:10.1007/jhep06(2013)084.

[40] G. Cowan, K. Cranmer, E. Gross, and O. Vitells, "Asymptotic formulae for likelihood-based tests of new physics", *Eur. Phys. J. C* **71** (2011), no. 2, 1554, doi:10.1140/epjc/s10052-011-1554-0.

[41] A. L. Read, "Presentation of search results: the CLs technique", *J. Phys. G: Nucl. Part. Phys.* **28** (2002) 2693, doi:10.1088/0954-3899/28/10/313.

[42] ATLAS Collaboration, "Observation of Higgs boson production in association with a top quark pair at the LHC with the ATLAS detector", *Phys. Lett. B* **784** (2018) 173, doi:https://doi.org/10.1016/j.physletb.2018.07.035.

[43] CMS Collaboration, "Observation of $t\bar{t}H$ Production", *Phys. Rev. Lett.* **120** (2018) 231801, doi:10.1103/physrevlett.120.231801.

[44] GEANT4 Collaboration, S. Agostinelli et al., "GEANT4 – a simulation toolkit", *Nucl. Instrum. Meth. A* **506** (2003) 250, doi:10.1016/S0168-9002(03)01368-8.

[45] ATLAS Collaboration, "The simulation principle and performance of the ATLAS fast calorimeter simulation FastCaloSim", *ATL-PHYS-PUB-2010-013* (2010). http://cdsweb.cern.ch/record/1300517.

[46] ATLAS Collaboration, "Search for the standard model Higgs boson produced in association with top quarks and decaying into a $b\bar{b}$ pair in pp collisions at $\sqrt{s} = 13$ TeV with the ATLAS detector", *Phys. Rev. D* **97** (2018) 072016, doi:10.1103/physrevd.97.072016.

[47] ATLAS Collaboration, "Evidence for the associated production of the Higgs boson and a top quark pair with the ATLAS detector", *Phys. Rev. D* **97** (2018) 072003, doi:10.1103/physrevd.97.072003.

[48] ATLAS Collaboration, "Search for Higgs boson pair production in the $\gamma\gamma b\bar{b}$ final state with 13 TeV pp collision data collected by the ATLAS experiment", *JHEP* **11** (2018) 040, doi:10.1007/jhep11(2018)040.

[49] ATLAS Collaboration, "Search for Higgs boson pair production in the two bottom quarks plus two photons final state in pp collisions at $\sqrt{s} = 13$ TeV with the ATLAS detector", *Phys. Rev. D* **106** (2022) 052001, doi:10.1103/physrevd.106.052001.

[50] S. Borowka et al., "Higgs Boson Pair Production in Gluon Fusion at Next-to-Leading Order with Full Top-Quark Mass Dependence", *Phys. Rev. Lett.* **117** (2016) 012001, doi:10.1103/PhysRevLett.117.012001.

[51] P. Nason and C. Oleari, "NLO Higgs boson production via vector-boson fusion matched with shower in POWHEG", *JHEP* **02** (2010) 037, doi:10.1007/JHEP02(2010)037.

[52] ATLAS Collaboration, "Validation of signal Monte Carlo event generation in searches for Higgs boson pairs with the ATLAS detector", *ATL-PHYS-PUB-2019-007* (2019). https://cds.cern.ch/record/2665057.

[53] J. Alwall et al., "The automated computation of tree-level and next-to-leading order differential cross sections, and their matching to parton shower simulations", *JHEP* **07** (2014) 079, doi:10.1007/JHEP07(2014)079.

[54] ATLAS Collaboration, "Constraining the Higgs boson self-coupling from single- and double-Higgs production with the ATLAS detector using pp collisions at $\sqrt{s} = 13$ TeV", *ATLAS-CONF-2022-050* (2022). https://cds.cern.ch/record/2816332.

[55] ATLAS Collaboration, "Measurement prospects of Higgs boson pair production in the $b\bar{b}\gamma\gamma$ final state with the ATLAS experiment at the HL-LHC", *ATL-PHYS-PUB-2022-001* (2022). https://cds.cern.ch/record/2799146.

[56] ATLAS Collaboration, "Report on the Physics at the HL-LHC and Perspectives for the HE-LHC", *ATL-PHYS-PUB-2019-006* (2019). https://cds.cern.ch/record/2664870.

[57] ATLAS Collaboration, "HL-LHC prospects for the measurement of Higgs boson pair production in the $b\bar{b}b\bar{b}$ final state and combination with the $b\bar{b}\gamma\gamma$ and $b\bar{b}\tau^+\tau^-$ final states at the ATLAS experiment", *ATL-PHYS-PUB-2022-053* (2022). https://cds.cern.ch/record/2841244.

[58] ATLAS Collaboration, "Technical Design Report for the ATLAS Inner Tracker Pixel Detector", *CERN-LHCC-2017-021* (2017) doi:10.17181/CERN.FOZZ.ZP3Q.

[59] ATLAS Collaboration, "Expected tracking and related performance with the updated ATLAS Inner Tracker layout at the High-Luminosity LHC", *ATL-PHYS-PUB-2021-024* (2021). https://cds.cern.ch/record/2776651.

[60] RD53 Collaboration, "The RD53A Integrated Circuit", *CERN-RD53-PUB-17-001* (2017). https://cds.cern.ch/record/2287593.

[61] RD53 Collaboration, "RD53B Manual", *CERN-RD53-PUB-19-002* (2019). https://cds.cern.ch/record/2665301.

[62] "YARR: Yet another Rapid Readout". https://yarr.web.cern.ch/yarr.

[63] "Local DB Docs". https://localdb-docs.readthedocs.io/en/master.

[64] "ITk Production Database". https://itkpd-test.unicorncollege.cz.

[65] R. Herbst et al., "Design of the SLAC RCE Platform: A general purpose ATCA based data acquisition system", in *2014 IEEE Nuclear Science Symposium and Medical Imaging Conference (NSS/MIC)*, pp. 1–4, 2014. doi:10.1109/NSSMIC.2014.7431254.

[66] ATLAS Collaboration, "Measurement of Higgs boson production in association with a $t\bar{t}$ pair in the diphoton decay channel using 139 fb^{-1} of LHC data collected at $\sqrt{s} = 13$ TeV by the ATLAS experiment", *ATLAS-CONF-2019-004* (2019). https://cds.cern.ch/record/2668103.

[67] ATLAS Collaboration, "Measurement of the properties of Higgs boson production at $\sqrt{s} = 13$ TeV in the $H \to \gamma\gamma$ channel using 139 fb^{-1} of pp collision data with the ATLAS experiment", doi:10.48550/arXiv.2207.00348. Submitted to *JHEP*.

[68] S. Amoroso et al., "Les Houches 2019: Physics at TeV Colliders: Standard Model Working Group Report", 2020. doi:10.48550/arXiv.2003.01700.

[69] ATLAS Collaboration, "A detailed map of Higgs boson interactions by the ATLAS experiment ten years after the discovery", *Nature* **607** (2022) 52–59, doi:10.1038/s41586-022-04893-w.